UNIVERSITY OF CALIFORNIA
Santa Barbara

Understanding and engineering two-dimensional electron gases in complex oxides

A Dissertation submitted in partial satisfaction
of the requirements for the degree of

Doctor of Philosophy

in

Materials

by

Lars Gunnar Tangen Bjaalie

Committee in Charge:

Professor Chris G. Van de Walle, Chair

Professor Susanne Stemmer

Professor S. James Allen

Professor Chris Palmstrøm

Professor Anderson Janotti

March 2016

The Dissertation of
Lars Gunnar Tangen Bjaalie is approved:

Professor Susanne Stemmer

Professor S. James Allen

Professor Chris Palmstrøm

Professor Anderson Janotti

Professor Chris G. Van de Walle, Committee Chairperson

March 2016

Understanding and engineering two-dimensional electron gases in complex oxides

by

Lars Gunnar Tangen Bjaalie

For Gunnar Bjålie (1914-1992).

Acknowledgements

There are many people who have helped me throughout my time as a PhD student. Naturally, the first mention goes to my advisor, Prof. Chris Van de Walle, who has guided my research over the past four and a half years. Beyond teaching me electronic structure calculations, solid state physics, and materials science, he has taught me invaluable lessons regarding presentation skills and how to be a good scientist. His clear focus on always having the audience in mind and presenting our work in such a way that it is both accessible and the most informative are skills that will serve me well in life regardless of career path. He also has a keen ability of always checking for consistency across a wide range of information sources (different experimental techniques and theoretical approaches).

In practical matters, such as learning how to run electronic structure calculations, discussing new ideas, and writing manuscript drafts, the help of Anderson Janotti was invaluable. He is also an excellent scientist, and has many important intellectual contributions to the work in this thesis. I wish him all the best in his new position as a Professor at the University of Delaware.

The postdocs and students of Chris' group also played a large role, and were always there for me to discuss ideas and get help on specific problems. I would like to thank the (past and current) group members Lars Ismer, Daniel Steiauf, Hartwin Peelaers, Qimin

Yang, Jack Lyons, Cyrus Dreyer, and Luke Gordon for answering my questions regarding electronic structure calculations and solid state physics. In particular, I would like to thank Burak Himmetoglu and Audrius Alkauskas. Burak and I worked together on a number of the projects in this thesis, where his knowledge of correlated electron systems was extremely valuable, and Audrius was of great assistance in the understanding of the optical transitions that will be presented in this work. I also owe gratitude to Karthik Krishnaswamy for helping me with problems related to device physics. The other students in the group, Wennie Wang, Jimmy Shen, and Michael Swift, and the new postdocs Zhu Zhen and Darshana Wickramaratne, have also always been helpful, and play no small part in ensuring that we have a positive and collaborative atmosphere within the group.

Outside of Chris' group, I also owe gratitude to the students in Prof. Susanne Stemmer's group (Pouya Moetakef, Tyler Cain, Clayton Jackson, Jack Zhang, Santosh Raghavan, and Evgeny Mikheev) and in Prof. S. James Allen's group (Daniel Ouellette) whom I interacted with in order to understand their experimental results. Beyond my colleagues at UCSB, I am also thankful to Amit Verma and Prof. Debdeep Jena (formerly at the University of Notre Dame, now at Cornell University) for collaborations on the study of the electronic structure of $GdTiO_3$, and to Slavomír Nemšák (formerly at UC Davis, now group leader at Forschungszentrum Jülich) and Prof. Charles Fadley (UC Davis) for collaborations on the two-dimensional electron gas in $SrTiO_3/GdTiO_3$

superlattices. I would also like to thank Profs. Jim Allen, Susanne Stemmer, and Chris Palmstrøm for serving on my committee, and the National Science Foundation for both paying my stipend through IRG-2 at the MRL at UCSB, and for providing funding for the XSEDE supercomputers where I carried out the vast majority of my calculations.

Beyond professional relationships, I must acknowledge the support of my parents, Tone Tangen and Jan Gunnar Bjålie. Especially critical to completing the work in this thesis I thank them for instilling in me patience and eagerness to learn new things, both leading by example. I also acknowledge the support of my friends, in particular José E. N. Rivera, Timothy R. Dunne, and Lei Yang, for helpful discussions about graduate school and life in general. Lastly, this work is dedicated to my grandfather, whose conviction to fight for liberty will continue to inspire me for the rest of my life.

Curriculum Vitæ

Lars Gunnar Tangen Bjaalie

Education

2016	Ph.D. in Materials, University of California, Santa Barbara. Advisor: Chris G. Van de Walle
2011	B.S. in Materials Science and Engineering, University of Illinois at Urbana-Champaign.

Awards

2016	Ovshinsky Student Travel Award
2015	UCSB Doctoral Student Travel Grant
2012 and 2015	MCC Travel Award
2012 - 16	MRL Travel Fellowship
2011	Holbrook Fellowship
2009 - 10	Louis R. Berner Materials Scholarship
2008 - 10	Dean's List

Publications

1. G. A. Ludueña, M. Wegner, **L. Bjålie**, and D. Sebastiani, "Local Disorder in Hydrogen Storage Compounds: The Case of Lithium Amide/Imide," *ChemPhysChem* 11, 2353 (2010).
2. A. Janotti, **L. Bjaalie**, L. Gordon, and C. G. Van de Walle, "Controlling the density of the two-dimensional electron gas at the $SrTiO_3/LaAlO_3$ interface," *Physical Review B: Rapid Communications* 86, 241108 (2012).
3. G. Conti, A. M. Kaiser, A. X. Gray, S. Nemšák, G. K. Palsson, J. Son, P. Moetakef, A. Janotti, **L. Bjaalie**, C. S. Conlon, D. Eiteneer, A. A. Greer, A. Keqi, A. Rattanachata, A. Y. Saw, A. Bostwick, W. C. Stolte, A. Gloskovskii, W. Drube, S. Ueda, M. Kobata, K. Kobayashi, C. G. Van de Walle, S. Stemmer, C. M. Schneider, and C. S. Fadley, "Band offsets in complex-oxide thin films and heterostructures of $SrTiO_3/LaNiO_3$ and $SrTiO_3/GdTiO_3$ by soft and hard X-ray photoelectron spectroscopy," *Journal of Applied Physics* 113, 143704 (2013).
4. **L. Bjaalie**, B. Himmetoglu, L. Weston, A. Janotti, and C. G. Van de Walle, "Oxide interfaces for novel electronic applications," *New Journal of Physics* 16, 025005 (2014).

5. A. Janotti, **L. Bjaalie**, B. Himmetoglu, and C. G. Van de Walle, "Band alignment at band-insulator/Mott-insulator interfaces," *Physica Status Solidi - Rapid Research Letters* 8, 577 (2014).

6. B. Himmetoglu, A. Janotti, **L. Bjaalie**, and C. G Van de Walle, "Interband and polaronic excitations in $YTiO_3$ from first principles," *Physical Review B: Rapid Communications* 90, 161102 (2014).

7. **L. Bjaalie**, A. Janotti, B. Himmetoglu, and C. G. Van de Walle, "Turning $SrTiO_3$ into a Mott insulator," *Physical Review B* 90, 195117 (2014).

8. **L. Bjaalie**, D. G. Ouellette, P. Moetakef, T. A. Cain, B. Himmetoglu, A. Janotti, S. J. Allen, S. Stemmer, and C. G. van de Walle, "Small hole polarons in rare-earth titanates," *Applied Physics Letters* 106, 232103 (2015).

9. **L. Bjaalie**, A. Verma, B. Himmetoglu, A. Janotti, S. Raghavan, V. Protasenko, E. H. Steenbergen, D. Jena, S. Stemmer, and C. G. Van de Walle, "Determination of the Mott-Hubbard gap in $GdTiO_3$," *Physical Review B* 92, 085111 (2015).

10. S. Nemšák, G. Conti, G. K. Pálsson, C. Conlon, S. Cho, J. Avila, M.-C. Asensio, C. Jackson, P. Moetakef, A. Janotti, **L. Bjaalie**, C. G. Van de Walle, L. Balents, C. M. Schneider, S Stemmer, "Observation by resonant angle-resolved photoemission of a critical thickness for 2-dimensional electron gas formation in $SrTiO_3$ embedded in $GdTiO_3$," *Applied Physics Letters* 107, 231602 (2015).

11. K. Krishnaswamy, **L. Bjaalie**, B. Himmetoglu, A. Janotti, L. Gordon, and C. G. Van de Walle, "$BaSnO_3$ as a channel material in perovskite oxide heterostructures," *Applied Physics Letters* 108, 083501 (2015).

12. S. Nemšák, G. Conti, A. X. Gray, G. K. Pálsson, C. Conlon, D. Eiteneer, A. Keqi, A. Rattanachata, A. Y. Saw, A. Bostwick, L. Moreschini, V. Strocov, M. Kobayashi, W. Stolte, A. Gloskovskii, W. Drube, P. Moetakef, C. Jackson, A. Janotti, **L. Bjaalie**, B. Himmetoglu, C. G. Van de Walle, J. Minar, J. Braun, H. Ebert, L. Plucinski, J. B. Kortright, C. M. Schneider, L. Balents, S. Stemmer, and C. S. Fadley, "Energetic, spatial and momentum character of a buried interface: the two-dimensional electron gas between two metal oxides," *submitted*.

13. **L. Bjaalie**, A. Janotti, B. Himmetoglu, and C. G. Van de Walle, "Metal versus insulator behavior in ultrathin $SrTiO_3$-based heterostructures," *submitted*.

14. **L. Bjaalie**, A. Janotti, K. Krishnaswamy, and C. G. Van de Walle, "Point defects as a source of small hole polarons in $GdTiO_3$," *submitted*.

Selected poster presentations

2015	International Conference on Defects in Semiconductors, Espoo, Finland Corbett Prize finalist "Defects and polarons in rare-earth titanates"

Contributed talks

2012	American Physical Society March Meeting, Boston, MA "First-principles calculations for Er impurities in Si"
2013	American Physical Society March Meeting, Baltimore, MD "Band alignments at the interface of complex oxides"
2014	American Physical Society March Meeting, Denver, CO "Evolution of the electronic structure of $SrTiO_3/GdTiO_3$ heterostructures with layer thickness"
2015	American Physical Society March Meeting, Denver, CO "Determination of the Mott-Hubbard gap in $GdTiO_3$"
2015	Compound Semiconductor Week, Santa Barbara, CA "Oxide interfaces for novel electronic applications"
2015	The International Union of Materials Research Societies, International Conference on Advanced Materials, Jeju, Korea "Determining the electronic structure of rare-earth titanates for complex oxide interfaces"

Invited Talks

2014	Materials Research Laboratory Outreach Program Symposium, Santa Barbara, CA "Oxide interfaces for novel electronic applications"

Abstract

Understanding and engineering two-dimensional electron gases in complex oxides

Lars Gunnar Tangen Bjaalie

The next generation of electronic devices faces the challenge of adequately containing and controlling extremely high charge densities within structures of nanometer dimensions. Atomic-scale transistors must be thin and be able to control extremely high charge densities ($>10^{13}$ cm^{-2}). Silicon devices typically have two-dimensional electron gas (2DEG) densities around 10^{12} cm^{-2}. Nitride-based devices can sustain densities an order of magnitude higher. The "complex oxides" have recently emerged as an attractive materials system to support these developments. The demonstration of a 2DEG at the $SrTiO_3/LaAlO_3$ interface has triggered an avalanche of research, including the unprecedentedly high density of 3×10^{14} cm^{-2} at $SrTiO_3/GdTiO_3$ and $SrTiO_3/SmTiO_3$ interfaces. Metal-insulator (Mott) transitions that are inherent to some of these complex oxides could offer even greater prospects for enhanced functionality or novel device concepts.

The materials and heterostructures that have been explored to date are clearly only a small subset of the vast number of materials combinations that could lead to interesting phenomena. In this work we use first-principles methods to build greater understanding

of the interface phenomena, so that searches can be better informed and more focused. We also develop a set of criteria that the materials and their heterostructures should satisfy to develop a high-performance 2DEG-based device. We focus in particular on the band alignment, calculating it for a variety of different potential materials.

Next, we study $GdTiO_3/SrTiO_3/GdTiO_3$ heterostructures in depth, where each interface contributes excess electrons into the $SrTiO_3$. We calculate the 2DEG formation for a superlattice containing six layers of $SrTiO_3$, and compare with angle-resolved photoemission spectroscopy results. Together, the experimental and theoretical results conclusively show that the 2DEG results from the interface itself, and does not originate from a secondary source such as oxygen vacancies. These heterostructures also exhibit a metal-to-insulator transition as the $SrTiO_3$ layer thickness decreases, which could possibly be used as a "Mott field effect transistor"—the system is very close to a metal-to-insulator transition, and modulating a small fraction of the electron density would lead to switching between the metallic and insulating phases. The mechanism behind this transition is unraveled, and we construct a bulk model of the transition based on the surprising observation that $SrTiO_3$ itself can become a Mott insulator when doped with an extremely high density of electrons.

Building on our study of the $SrTiO_3/GdTiO_3$ interfaces, we investigate the electronic structure of $GdTiO_3$ in detail—our calculated band gap differs markedly from past experimental values, but is consistent with recent photoluminescence measurements. We

find that the presence of small hole polarons leads to a feature in the optical absorption spectrum which was previously interpreted to be the band gap. Since small hole polarons are present in all the rare-earth titanates, not only $GdTiO_3$, the values of the band gaps (also based on optical absorption measurements) across the series will likely have to be revised. Lastly, to understand the formation of small hole polarons in the rare-earth titanates, we study point defects and impurities in $GdTiO_3$. We also investigate how defects may impact the behavior of $GdTiO_3$ in electronic devices.

Professor Chris G. Van de Walle
Dissertation Committee Chair

Contents

List of Figures

List of Tables

Chapter 1

Introduction: The complex oxides

The next generation of electronic devices faces the challenge of adequately containing and controlling high charge densities within structures of nanometer dimensions. Silicon-based electronics has been extremely successful. Silicon metal-oxide-semiconductor field effect transistors (MOSFETs) are based on a two-dimensional electron gas (2DEG) that is formed at the interface between Si and a dielectric, and electrostatically controlled by a gate voltage. As devices are scaled to atomic dimensions the capacitance density and the switched current density must both increase.[1] Atomic-scale transistors must be thin and be able to control extremely high charge densities ($>10^{13}$ cm^{-2}). Silicon devices typically have 2DEG densities around 10^{12} cm^{-2}. Nitride-based devices can sustain densities an order of magnitude higher. To go beyond that, novel materials that can support extremely high charge densities and high electric fields need to be explored.

The "complex oxides" have recently emerged as an attractive materials system to support these developments. These oxides are transition metal oxides with at least two other elements other than oxygen, and their study spans several sub-fields of condensed matter physics. They display a staggering number of different properties, such as superconductivity,[2] metal-insulator transitions,[3] ferroelectricity,[4] and colossal magnetoresistance.[5] These are effects that are not observed in "regular" semiconductors, insulators, and metals, but arise from the highly spatially confined transition metal *d*- and *f*-states. In addition, the electron-electron (Coulomb) interactions are linked with spin, orbital, and lattice degrees of freedom. Research interest in these compounds has recently increased substantially, with the goal of creating new electronic devices which can overcome the scaling limits inherent to the silicon-based semiconductor technology.

In this work, we will concern ourselves with perovskite oxides with the chemical formula ABO_3, with A being an alkali earth metal, a metalloid, or a rare-earth element, and B being a regular or transition metal. We will study a tiny subset of the huge array of compounds that can be formed from these elemental ingredients, motivated by the spontaneous formation of a two-dimensional electron gas at the interface between certain perovskite oxides (a full explanation of this phenomenon is given in Section 1.2). The demonstration of a 2DEG at the $SrTiO_3/LaAlO_3$ (STO/LAO) interface[6–8] has triggered an avalanche of research. 2DEG densities up to 3×10^{13} cm^{-2} can be achieved in STO/LAO, but unprecedentedly high densities of 3×10^{14} cm^{-2} have since been demon-

strated at $SrTiO_3/GdTiO_3$ (STO/GTO) and $SrTiO_3/SmTiO_3$ interfaces.[9,10] In addition, the interfaces have been reported to display unique behavior such as ferromagnetism[7] and superconductivity.[11] Metal-insulator (Mott) transitions that are inherent to some of the complex oxides could offer even greater prospects for enhanced functionality or novel device concepts.[12,13] These oxide interfaces have been made possible due to tremendous recent progress in materials growth technology, in particular in pulsed laser deposition (PLD)[14] and molecular beam epitaxy (MBE).[15]

In the next sections we will discuss the structural and electronic properties of perovksite oxides. In particular, we will discuss the properties of perovskites with a transition metal B-site atom which have conduction bands derived from *d*-states, since this is the category of compounds we will study in detail. We will also explain the formation of the interface 2DEG formation via the polar discontinuity.

1.1 The perovskites

1.1.1 Structural properties

The ideal simple cubic perovskite crystal structure is shown in Figure 1.1(a). It is a 5-atom unit cell (space group $Pm\bar{3}m$) characterized by corner-sharing BO_6 octahedra. The A-site cation is usually fully ionized, and the functionality of the material is derived from the B-site transition metal cation. Most perovskites are found in more

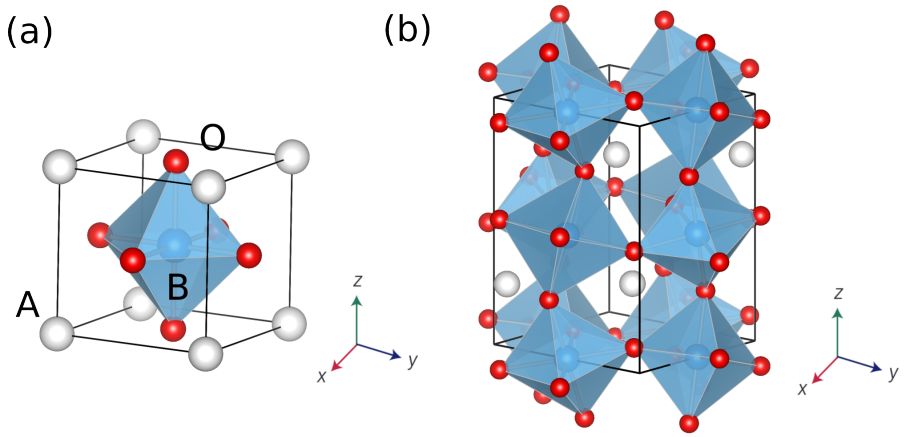

Figure 1.1: The perovskite structure. 5-atom simple cubic cell shown in (a) and 20-atom $GdFeO_3$ unit cell with octahedral rotations and A-site cation off-centering shown in (b).

complicated structures, breaking the simple cubic symmetry: Tetragonal, rhombohedral, or orthorhombic crystal structures are possible. This symmetry breaking results from BO_6 octahedral rotations and deformations (changes to the B-O bond length), which are also accompanied by A-site cation off-centering. Figure 1.2(b) shows an example: a rhombohedral 20-atom unit cell. This unit cell has the octahedral tilt pattern of all the non-cubic perovskites we will study (space group *Pbnm*). These deviations from the simple cubic structure are caused by lattice instabilities arising from ionic size mismatch, and/or the first-order Jahn-Teller effect (wherein the total energy of the system can be lowered by breaking an electronic degeneracy of the B-site *d*-states by an appropriate structural distortion).

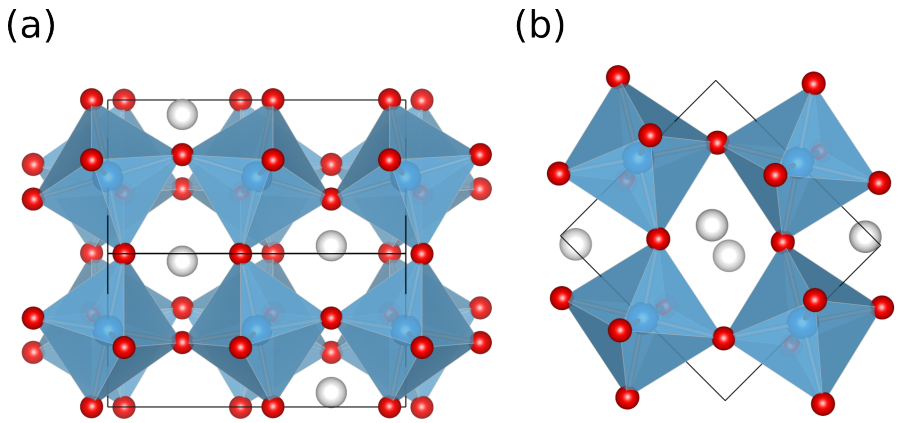

Figure 1.2: The 20-atom $GdFeO_3$ structure, looking at the (a) $(110)_o$ and (b) $(001)_o$ planes. The subscript "o" indicating that the axes are referenced to the 20-atom unit cell, and not the 5-atom simple cubic cell.

Octahedral tilts and rotations (keeping the B-O bond lengths intact) arising from ionic size mismatch can be understood via the geometric problem of packing hard spheres together in the perovskite structure, resulting in the Goldschmidt tolerance factor[16]

$$t' = \frac{r_A + r_O}{\sqrt{2}(r_B + r_O)} \tag{1.1}$$

where r_A, r_B, r_O are the ionic radii of the atomic species. If $t' > 1$, the structure tends to be hexagonal or adopt B-site ferroelectric off-centering distortions, if $1 > t' > 0.9$ it tends to be cubic, and if $t' < 0.9$ it tends to have octahedral tilts and rotations (this simple criterion cannot tell us anything about the nature of these distortions). There are 23 perovskite tilt systems and 15 space groups.[17] I will not go into detail regarding the possible relative orientations of the octahedra, and instead refer the reader to the book by R. H. Mitchell.[18] All the distorted perovskites we will study in this work have

the $GdFeO_3$ structure (space group $Pnma$). Figure 1.2 shows the octahedral rotations for this structure, and shows that the A-site cation is displaced away from the cubic positions to accommodate the octahedral rotations.

1.1.2 Electronic properties

The structural distortions are key in determining the electronic properties of the perovskite. To understand why, we first look at the bonding arrangement (Figure 1.3). The A-site cation does not usually play an important role in bonding, and the interactions between the B-site and O atoms dictate the physics of the compound. These bands are derived from the antibonding B-O π and σ bonds. The top of the O $2p$ band is predominantly non-bonding with the transition metal. In general, transition metal oxides are different from other materials such as metals, covalently bonded semiconductors, and ionic insulators. The bonding between the O and the transition metal is mainly covalent, with some ionic contribution, and the conduction bands are made up of transition metal d- or f-states. Depending on the orbital occupation and structure, these states can be either delocalized (large overlap with O $2p$ states) or localized (small overlap). Therefore, small changes in the B-O-B interactions (via bond angles and lengths) in the perovskite can completely determine the electronic properties of the material. One specific example we will see in this work (Chapter 4) is that changes to the bond angles can

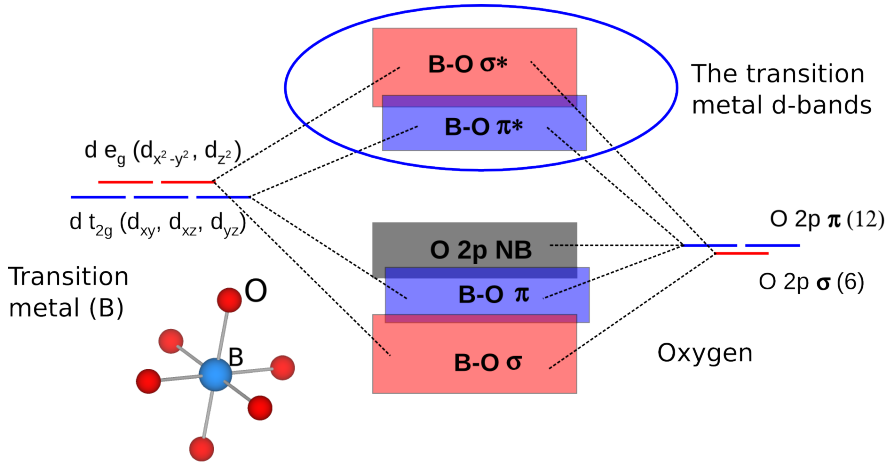

Figure 1.3: Molecular-orbital diagram for the bands arising from the bonding between transition metal d-states and oxygen $2p$-states in the perovskites. The ordering of these bands is discussed in the text.

drive a Mott metal-insulator transition. Figure 1.4 illustrates how the overlap between the d and O $2p$ states decreases as the bond angle increases.

We next examine how the surrounding atoms (in this case, oxygen) create an electric field felt by the orbitals of the transition metal atom. This is the "crystal field" felt by the d states, and it is a perturbation to the electronic system which is able to break the five-fold degenerate d orbitals in the free atom (spherical symmetry). In a simple cubic perovskite, the effective electric field leads to the splitting into the three-fold t_{2g} (d_{xy}, d_{xz}, d_{yz}) and two-fold e_g $(d_{x^2-y^2}, d_{z^2})$ orbital sets with some crystal field splitting Δ_{cf} [Figure 1.5(a)]. The ordering of the t_{2g} and e_g sets is caused by the spatial orientation of the orbital lobes with respect to those of oxygen: The e_g orbitals have a maximum near the negatively charged oxygen atoms, and the t_{2g} a minimum.

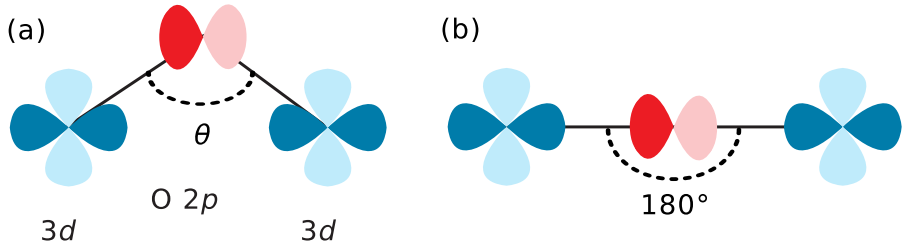

Figure 1.4: Changing overlap between transition metal (B) d-orbitals and O $2p$ orbitals as B-O-B bond angle is tuned. Smaller overlap for (a), with bond angle smaller than the cubic 180° shown in (b).

Further symmetry breaking via tetragonal elongation/compression of the octahedra (two long or short bonds) may also occur, as illustrated in Figure 1.5(a). If there is a combination of tetragonal elongations or compressions, along different axes, resulting in three pairs of B-O bonds of different length, the crystal field becomes orthorhombic, further lowering the symmetry. These results can be derived from group theory, considering the symmetry properties of the d-orbital spherical harmonic wave functions. All the orbitals can also be doubly occupied, and due to direct exchange interactions (Hund's exchange) between the spins of orthogonal and partially occupied d orbitals, there is further splitting into spin up and down components as shown in Figure 1.5(b), with an exchange splitting Δ_{ex}.

If the B-site d- or f-states are occupied, octahedral distortions can occur by lowering the total energy of the system by breaking an electronic degeneracy (the first-order Jahn-Teller effect). From our simple treatment of the crystal field, we immediately see how the

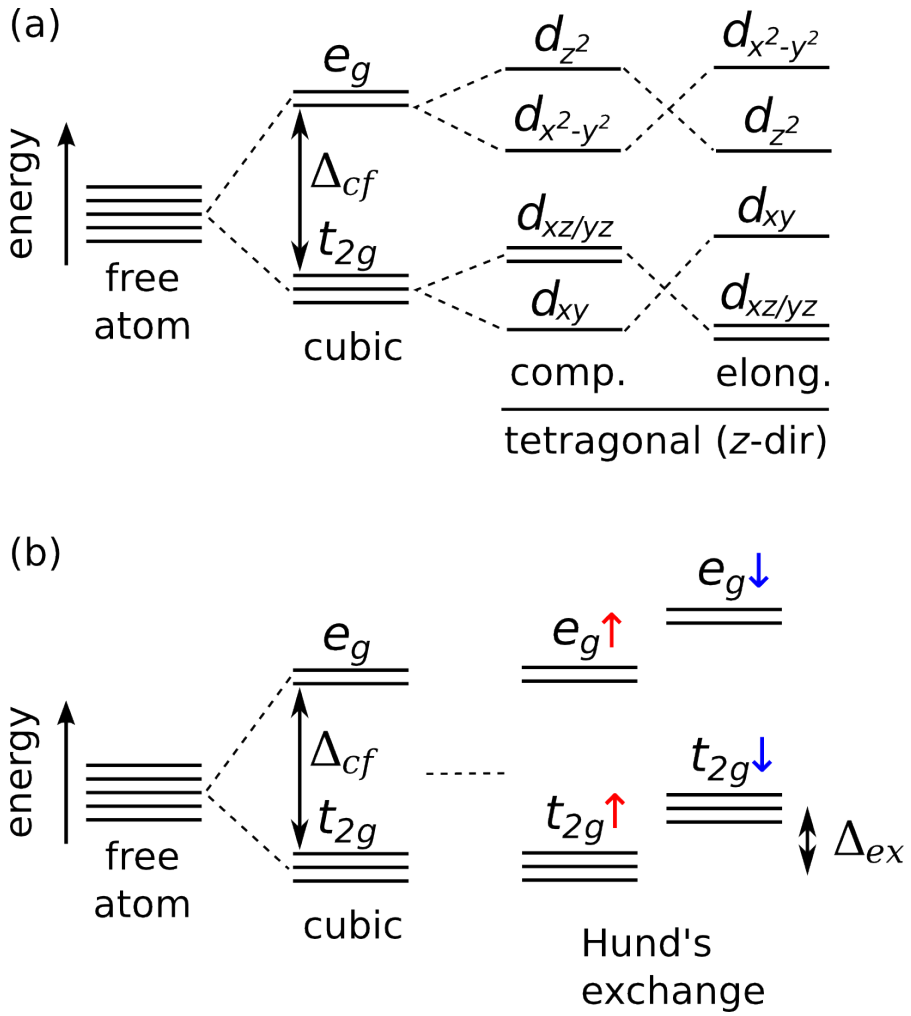

Figure 1.5: The influence of (a) crystal field splitting under cubic symmetry and tetragonal compression (comp.) and elongation (elong.), and (b) Hund's exchange on the degeneracies of the d-states.

filling of the d states can contribute to octahedral distortions by favoring bond lengths deviating from three equal pairs. The introduction of such distortions will *increase* the structural energy of the system, but it will *decrease* the electronic energy—a balance will be struck, giving the maximal lowering of the total energy. For example, in the rare-earth titanates (RTiO3, where R is a rare-earth atom in the +3 valence state), which we will study in this work, each Ti atom has one $3d$ electron associated with it (electron configuration $3d^1$), leading to octahedra with different B-O bond lengths.

1.1.3 Magnetism

In these perovskites, the magnetic interactions from the direct overlap of d orbitals on separate atoms are negligible due to the large interatomic distance (4 Å), but substantial nearest-neighbor interactions occur via the overlap with oxygen $2p$ orbitals. As mentioned above (and shown in Figure 1.4), the overlap is the largest for B-O-B bond angles of 180° and decreases as the angle diminishes. There are two types of interactions that arise from the hopping of electrons between different d orbitals, double exchange and superexchange. Double exchange (or real kinetic exchange) is the transfer of electrons between transition metal atoms (mediated via the bonding to oxygen) with different valency, which requires an individual electron to retain its spin. This interaction is therefore ferromagnetic in nature. Conversely, superexchange results from the *virtual* kinetic exchange between two spins in non-orthogonal orbitals. For two singly

occupied orbitals, the Pauli exclusion principle requires antiferromagnetic interactions. If the interactions are instead between a singly occupied and empty orbital, then the transfer of spin-up electron density into the empty orbital favors ferromagnetic coupling because of the intra-atomic exchange interactions between electrons in different orbitals.

In the rare-earth titanates ($3d^1$ electron configuration), superexchange is the cause of the magnetic behavior, since the orbitals on two neighboring Ti sites (Ti-O-Ti) are singly occupied and non-orthogonal. For the members of the series with larger rare-earth radius (for example $LaTiO_3$ and $NdTiO_3$) the bond angles are close enough to 180° for the singly occupied orbitals on two neighboring Ti atoms (Ti-O-Ti) to have significant overlap, resulting in antiferromagnetic order. As the rare-earth radius becomes smaller (for example $GdTiO_3$ and $YTiO_3$), the overlap between two occupied orbitals decreases and the overlap between occupied/empty orbitals increases, giving ferromagnetic order.

1.1.4 Electron correlation

As the bands formed by the transition metal d orbitals become filled, we need to consider the consequences of the spatially confined nature of these orbitals. This confinement results in small inter-atomic overlap and narrow bands (this also applies to bands derived from f orbitals). When electrons are placed in these narrow bands, their interactions go beyond simple band theory, in which electrons can be described as interacting with an average potential. This leads to band theory failing to predict insulating

phases of partially filled d-states. There is now an electron-electron Coulomb repulsion energy cost U of doubly occupying an orbital which cannot be neglected—the material is said to be "strongly correlated". The consequence of this electronic correlation is just as important as covalent bonding in understanding the electronic properties.

By comparing the magnitude of U to the kinetic energy of the electrons, or the orbital bandwidth W, U/W gives the degree of this correlation. If the kinetic energy W is large enough compared to U, the electrons can overcome the on-site Coulomb repulsion U and form extended metallic states. However, if W is small (narrow band) then localization will be favorable to avoid the relatively larger energy cost U, and the system is insulating. This can occur in mainly two ways; charge-transfer and Mott-Hubbard insulators.[19] Figure 1.6 shows the different cases, with Δ being the charge-transfer energy (energy to transfer an electron from the anion to the transition metal cation). The resulting filled/empty bands are referred to as the lower and upper Hubbard bands (LHB and UHB).

In the perovskites we study, the kinetic energy W is determined by the interactions between the d orbitals of neighboring B-site atoms. As for the magnetic interactions, the direct overlap of d orbitals is negligible, and it is the interactions via O $2p$ orbitals that largely determine W. Small changes in the structure (changes to B-O-B bond angles and lengths) can therefore change W, driving metal-insulator transitions (MITs). Controlling this type of MIT is one example of "Mottronic applications", where small

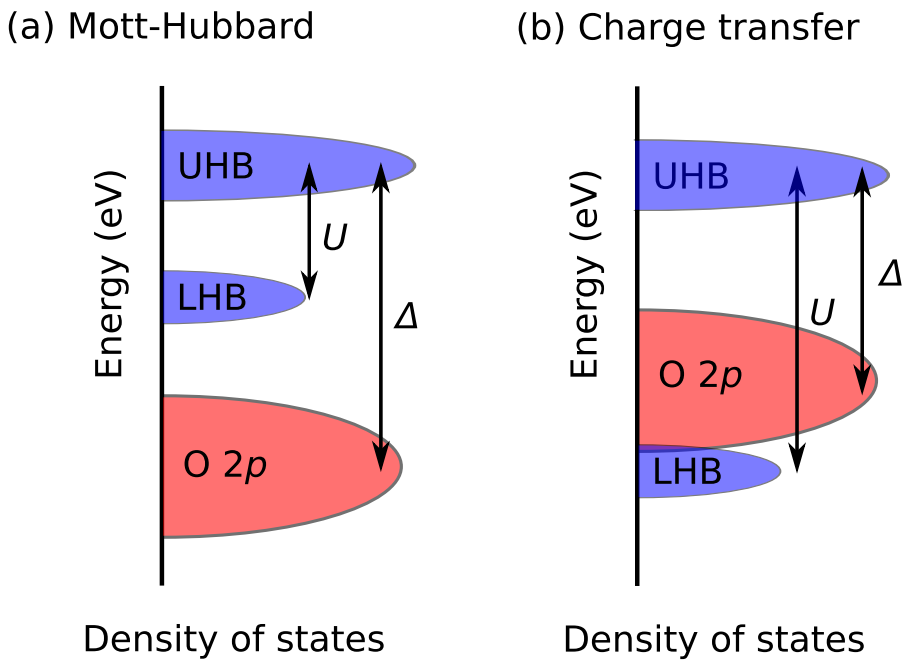

Figure 1.6: Diagram of the bands in (a) a Mott-Hubbard insulator and (b) a charge-transfer insulator.

external perturbations drive transitions between competing electronic, orbital, charge and spin orderings.[3]

As mentioned in past sections, in this work we will study the rare-earth titanates, which are Mott insulators where the $3d^1$ electrons form a LHB. The theoretical methods that we will use are applicable if U is appreciably larger than W. If U and W are of similar magnitude, then delocalized electronic states around the Fermi level dynamically screen the effective interaction between electrons residing on Ti $3d$ orbitals ("dynamical correlations"), requiring more advanced methods. In the rare-earth titanates W is the hopping amplitude between d orbitals of neighboring Ti sites, which is small in comparison to U.[20] These materials are not close to the metal-insulator transition, and we do not have delocalized electronic states around the Fermi level. However, in other systems dynamical correlations may be important, for example in correlated metals (such as $LaNiO_3$) or systems in the vicinity of a metal-insulator transition (such as VO_2). The reader is referred to the review by A. Georges *et al.*[21] for an in-depth discussion of dynamical correlation.

1.2 Formation of a 2DEG and polar discontinuity doping

In this section, I will describe in detail how one can form a 2DEG at the interface between two perovskite oxides, taking advantage of an interface "polar discontinuity", and explain how this 2DEG differs from those formed at conventional semiconductor interfaces.

To realize a 2DEG, two ingredients are required: confinement and a source of electrons. Confinement is provided by forming a heterojunction: electrons are located in a semiconducting layer in which the energy of the conduction band is lower than in an adjacent barrier material. These electrons are confined to the vicinity of the interface in a (roughly) triangular potential well, which is formed by electrostatics (through application of a gate voltage) and/or because electrons are attracted to the interface by positive charges. As to the source of carriers: in a depletion-mode MOSFET, the carriers in the channel are provided by doping of the channel, while in the more common enhancement-mode MOSFET, they arise from electrostatic manipulation of the band structure: a positive gate voltage pulls the conduction band below the Fermi level, creating an inversion layer in the p-type substrate in which electrons from the n-type source can flow.[22] In high electron mobility transistors (HEMTs), the electrons are typically provided by modulation doping.[22] III-nitride based transistors offer higher confinement

and 2DEG densities due to polarization fields intrinsic to the wurtzite structure of the nitride semiconductors. Modulation doping has recently been demonstrated for an oxide heterojunction between STO and $SrTi_{0.95}Zr_{0.05}O_3$.[23]

One could hypothesize a structure in which the source of electrons would be intrinsic to the heterojunction itself: i.e., an atomically thin layer of donors right at the interface between the two materials [see Figure 1.7 (a)]. This would have the advantage of providing a very high density of electrons right where they are needed, and simultaneously confining them due to electrostatic attraction of the electrons to the positively charged donor centers. One might think that delta doping of semiconductors could achieve this goal; however, in practice delta doping is impossible to achieve with atomic precision, and any randomness in the doping profile will cause a high degree of scattering and lower the mobility.

It turns out to be possible, however, to create such a layer of delta doping intrinsically at the interface between two materials. As a generic example, consider two materials, one polar and the other nonpolar. Assume these materials have a cubic crystal structure, with lattice parameters that are close enough that a properly bonded interface can be formed. Looking along the [001] direction, we can picture the nonpolar material as consisting of atomic layers that are all charge neutral (i.e., the electronic charge in each layer exactly equals the ionic charge). The polar material, on the other hand, consists of layers that are charged; in the example of Figure 1.7(b), charges of +1 and

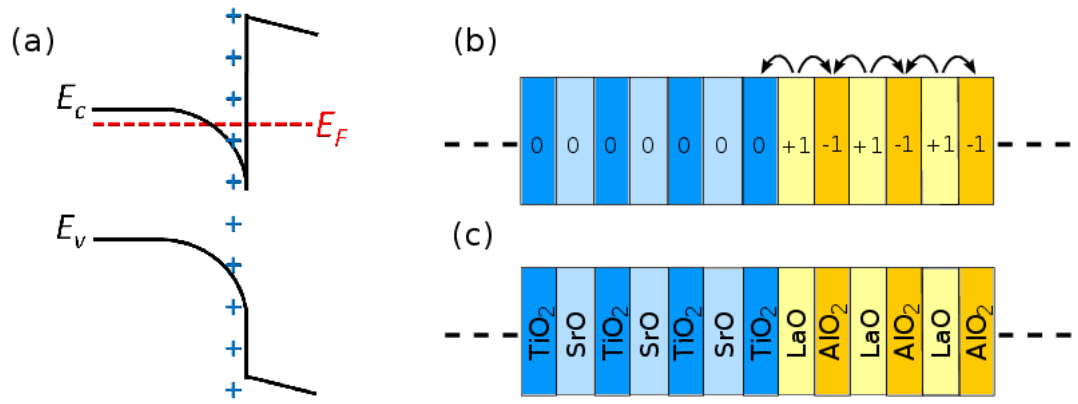

Figure 1.7: (a) Illustration of charge at a heterojunction resulting from an intrinsic interface layer of donors, providing a high density of carriers as well as electrostatically confining them to the interface. (b) Schematic showing an interface between a nonpolar and a polar material. Charges on layers are indicated, and arrows indicate electron transfer between layers in the polar material. At the interface, an excess 1/2 electron is present. (c) Polar discontinuity at the $SrTiO_3/LaAlO_3$ interface.

-1 per unit cell are assumed. The presence of such charges arises, of course, from an imbalance in the electronic and ionic charges, and arises in any material that has at least partially ionic character. Many ionic crystals exhibit such polar behavior, although regular semiconductors such as GaAs can also be considered in this fashion.[24] The local charges arise from the fact that electrons in one layer are transferred to adjacent layers: if a layer ends up with a net positive charge of $+1$, it is because 1/2 electron has been transferred to the layer to its left, and 1/2 electron to the layer to its right, leaving those layers with a net negative charge.

The bulk of the material remains, overall, charge neutral. But an interesting phenomenon occurs if an interface is formed between a polar and a nonpolar material [Figure 1.7(b)]: the layer in the polar material adjacent to the nonpolar material donates 1/2 electron to the right, i.e., to a "bulk-like" layer in the polar material. It is also trying to donate 1/2 electron to the layer to its left—but that layer belongs to a nonpolar material and does not need that electron to satisfy its bonding. This electron is therefore in principle available as a free electron, and the atomic layer on the polar side of the interface effectively acts as a layer of donors with a density of 1/2 of the areal density of atoms at the interface. In most materials, this is on the order of a few times 10^{14} cm^{-2}; i.e., a huge density compared to what is typically achieved in 2DEGs at conventional interfaces. We will refer to this situation as "polar discontinuity doping" of interfaces.

In case all of this sounds far-fetched: a concrete example was discussed in the context of conventional semiconductors such as Ge and GaAs as early as 1978, by Harrison *et al.*[25] Unfortunately, an implementation with such semiconductors has not proved feasible, mainly because the interfaces have a tendency for intermixing and/or the surfaces of semiconductors tend to be heavily reconstructed, rendering it difficult to obtain the abrupt interfaces required for self-doping. We note that the nitride interfaces, such as the AlGaN/GaN interfaces employed in HEMTs, do not exhibit polar-discontinuity doping. The nitrides, because of their wurtzite structure, exhibit *polarization discontinuities*, which enhance the density and confinement of the 2DEG—but (contrary to some early reports) the electrons in this 2DEG still need to be externally supplied, either by extrinsic doping or from surface states.

Interestingly, perovskite oxides *do* seem to enable the formation of the abrupt polar/nonpolar interfaces required for self-doping; indeed the by now famous STO/LAO interface falls into this category, as illustrated in Figure 1.7(c). Recent work, based on a combination of first-principles calculations (which I performed) and macroscopic Schrödinger-Poisson simulations, demonstrated that the electrons in the 2DEG are truly intrinsic to the STO/LAO interface and generated by the polar discontinuity.[26] This work also demonstrated that the electrons in the STO conduction band are delocalized over several atomic layers—in contrast to models where electrons are purported to reside in "Ti^{3+}" states on the STO side. Such a localization of electrons would be inconsistent

with the high mobilities that have been observed. However, as will be explained in Chapter 4, electrons *do* reside in Ti^{3+} states if the STO layer is sufficiently thin, which has been experimentally observed for STO/GTO quantum wells.[27]

The 2DEG formation at the STO/GTO interface can be understood in the same way as for STO/LAO. In STO, the valences are Sr^{2+}, Ti^{4+}, and O^{2-}; in GTO, Gd^{3+}, Ti^{3+}, and O^{2-}. Along the [001] direction, STO is non-polar since it is composed of charge-neutral $(TiO_2)^0$ and $(SrO)^0$ planes, whereas GTO is polar, composed of $(TiO_2)^-$ and $(GdO)^+$ planes. Each GdO plane donates 1/2 electron per STO unit-cell area to each of the adjacent TiO_2 planes. At the (001) interface, there is therefore a polar discontinuity, giving rise to an excess of 1/2 electron per unit-cell area. Since the conduction-band minimum of STO lies within the Mott Hubbard gap of GTO,[28] the excess electrons end up in the STO. Therefore, in a GTO/STO/GTO heterostructure (Figure 1.8), there will be an excess $2\times1/2$ electron per unit-cell area (corresponding to a 2D density of $\sim 7 \times 10^{14}$ cm^{-2}) in the STO.

1.3 Summary

Complex oxide interfaces offering unprecedentedly high interface 2DEG densities are a promising new class of materials for electronics. In the rest of this thesis we will study the properties of bulk, interfaces, and defects in this context. To do so, we need to

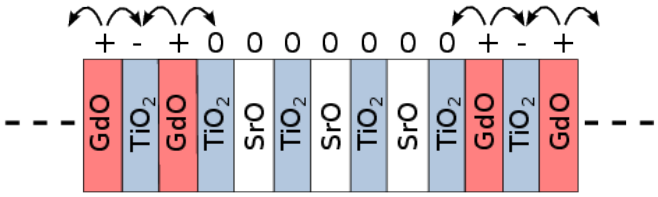

Figure 1.8: Polar discontinuities in a $SrTiO_3/GdTiO_3$ double heterostructure. Arrows indicate electron transfer between planes in the polar material. At each interface, an excess 1/2 electron per unit cell area is present, giving a 2D electron density of $\sim 7 \times 10^{14}$ cm^{-2}.

build on the understanding laid out in this chapter regarding structural and electronic properties. This is required to calculate band offsets and identify criteria for devices which we describe in Chapter 3, study the metal-insulator transition at STO/GTO interfaces in Chapter 4, and determine the band gap and impact of small hole polarons in GTO which we do in Chapters 5 and 6. Our method of investigation will be first-principles electronic structure calculations, which will be discussed in the next Chapter.

Chapter 2

First-principles calculations

To study the complex oxides described in Chapter 1, including the Mott-insulating rare-earth titanates, we will use first-principles electronic structure calculations based on density functional theory. This will allow us to obtain the electronic structure of the valence electrons, which are the electrons that participate in bonding and determine the properties of solid-state systems.

The idea behind first-principles (or *ab initio*) calculations is to start from the governing equation in (nonrelativistic) solid-state physics, the Schrödinger equation, and solve for the wave functions and eigenvalues. In principle, this means that no empirical parameters are necessary, so that the theory has predictive power. Additionally it can be used to explain and interpret experimental observations. However, in practice a number of approximations must be made. These approximations in solving the Schrödinger

equation will be described briefly below, but the discussion only touches the surface—the reader is recommended to study the textbook by R. Martin for a more in-depth treatment.[29]

2.1 The many-body problem

We start from the many-body Schrödinger equation in Hartree atomic units (neglecting relativistic effects and the influence of magnetic fields),

$$\hat{H}\Psi(\{\mathbf{r}_i\},\{\mathbf{R}_i\};t) = \Bigg[-\frac{1}{2}\sum_i \nabla_i^2 + \frac{1}{2}\sum_{i\neq j}\frac{1}{|\mathbf{r}_i-\mathbf{r}_j|} - \sum_{i,I}\frac{Z_I}{|\mathbf{r}_i-\mathbf{R}_I|} - \sum_I \frac{1}{2M_I}\nabla_I^2 + \frac{1}{2}\sum_{I\neq J}\frac{Z_I Z_J}{|\mathbf{R}_I-\mathbf{R}_J|}\Bigg]\Psi(\{\mathbf{r}_i\},\{\mathbf{R}_i\};t) = i\frac{\partial\Psi(\{\mathbf{r}_i\},\{\mathbf{R}_i\};t)}{\partial t}, \tag{2.1}$$

where lower-case subscripts denote a given electron, upper-case subscripts denote a given nucleus, the $\mathbf{r}$'s are the electron positions, the $\mathbf{R}$'s are the nuclear positions, M_I is the nuclear mass, and Z is the nuclear charge. The first term on the left-hand side of Eq. (2.1) is the kinetic energy of the electrons, the second term is the Coulomb interaction between electrons, the third term is the potential energy of the electron-nuclei interaction, the fourth term is the kinetic energy of the nuclei, and the final term represents the interactions between the nuclei. The properties of the system are determined by solving for the wave function Ψ. The solution to Eq. (2.1) will determine

the material's atomic and electronic structure—whether it is a metal or an insulator, its conductivity, its band gap, and so on.

The first approximation we will introduce to solve the Schrödinger equation is the Born-Oppenheimer (BO) approximation. We treat the nuclei classically by setting their mass to infinity ($M_I \to \infty$), so that their kinetic energy (the fourth term in $\hat{H}$) goes to zero. This allows us to determine the electronic structure for the fixed external potential of the nuclei. The nuclei-nuclei interactions (fifth term in $\hat{H}$) is then given simply by classical electrostatics. After calculating the electronic structure, we find the atomic forces via the Hellmann-Feynman theorem, and the positions of the atoms can be optimized.

We introduce a simplified notation, writing the electron kinetic energy as $\hat{T}$, the electron internal potential energy operator as $\hat{V}_{\text{int}}$, the electron external potential (from the nuclei) energy operator as $\hat{V}_{\text{ext}}$, and the classical interaction between nuclei as E_{II}. The total energy is the expectation value of the Hamiltonian

$$E = \frac{\langle \Psi | \hat{H} | \Psi \rangle}{\langle \Psi | \Psi \rangle} = \langle \hat{T} \rangle + \langle \hat{V}_{\text{int}} \rangle + \langle \hat{V}_{\text{ext}} \rangle + E_{II}. \tag{2.2}$$

Eqs. (2.1) and (2.2) seem simple enough, but finding a solution is unfortunately computationally intractable for more than a few electrons and nuclei. The main issue is the electron-electron interaction term $\hat{V}_{\text{int}}$, in which the number of terms increases exponen-

tially with the number of electrons. The next section details how we will approximate this problem using density functional theory.

2.2 Density functional theory

Even though more than 50 years old, DFT still represents the main computational tool to perform electronic structure calculations, by making the problem of calculating the electronic structure of a many-body system tractable. The basic idea is to treat the electron *density*, instead of the explicit electron wave functions, as the defining variable of the system. The groundbreaking 1964 work by Hohenberg and Kohn (HK)[30] proved that all ground- and excited-state properties of a system in a given external potential are uniquely defined by the ground-state density of the system. They also proved that for any external potential, there exists an energy functional of the density, $E[n(\mathbf{r})]$, whose global minimum (over all densities n that represent N electrons) is the ground-state energy of the system, and the density that results from minimizing this functional is the exact ground-state density. These theorems are the theoretical basis upon which DFT is founded.

Dealing with the density instead of the full wave functions makes the many-body problem a lot more tractable. Each wave function depends on the positions of *all* the electrons in the system, meaning that for N electrons, it has $3N$ variables. In com-

parison, the density $n(\mathbf{r})$ has only three spatial variables for *any* number of electrons. This makes it possible to simulate more than a handful of electrons, instead going up to about a thousand electrons.

The HK theorems do not give any practical information *how* to obtain the ground-state density of a system, or what $E[n(\mathbf{r})]$ might be, and it is not obvious how to formulate Eq. (2.2) in terms of densities. These practical details were outlined shortly after the HK theorems by Kohn and Sham (KS),[31] in their formulation of KS-DFT: Replace the many-body-interacting system of electrons by an auxiliary system of noninteracting particles in an effective potential chosen so that it reproduces the ground-state density of the many-body system.

We attempt to write an energy functional of the density for such a system in terms of *single*-particle wave functions $\psi(\mathbf{r})$. The density for N single-particle wave functions is given by

$$n(\mathbf{r}) = \sum_{i=1}^{N} |\psi_i(\mathbf{r})|^2, \tag{2.3}$$

and the kinetic energy is

$$T_e^{\mathrm{s}} = \frac{1}{2} \sum_{i=1}^{N} \int d\mathbf{r} |\nabla \psi_i(\mathbf{r})|^2, \tag{2.4}$$

where we use the superscript "S" for "single particle" to differentiate it from the full many-body kinetic energy. Since the kinetic energy is not a smoothly varying function of the density, it is difficult to construct a kinetic energy density functional. However,

this does not turn out to be an issue in practice, since we can express the kinetic energy in terms of single-particle wave functions.

Since we are operating under the BO approximation, we neglect the kinetic energy of the nuclei. We consider the potential of the nuclei as a fixed external potential, and write the nucleus-electron interaction from classical electrostatics as

$$E_{\text{ext}} = \int d\mathbf{r} V_{\text{ext}}(\mathbf{r}) n(\mathbf{r}), \tag{2.5}$$

and the nucleus-nucleus interaction is still a constant with respect to the electron density, as outlined above:

$$E_{\text{II}} = \frac{1}{2} \sum_{I \neq J} \frac{Z_I Z_J}{|\mathbf{R}_I - \mathbf{R}_J|}. \tag{2.6}$$

We can write part of the electron-electron interaction as the Hartree energy of a classical charge density interacting with itself

$$E^{\text{s}}_{\text{Hart}} = \frac{1}{2} \int d\mathbf{r} d\mathbf{r}' \frac{n(\mathbf{r}) n(\mathbf{r}')}{|\mathbf{r} - \mathbf{r}'|}. \tag{2.7}$$

The KS energy functional is then

$$E_{\text{KS}} = T^s_e + E_{\text{ext}} + E^s_{\text{Hart}} + E_{\text{II}} + E_{\text{XC}} \tag{2.8}$$

where we have lumped all the difficult total energy contributions from many-body effects (not included in the noninteracting kinetic energy and Hartree energy) in the exchange-correlation (XC) energy E_{XC}. We will soon return to how to deal with this term.

According to the HK theorems, the density that minimizes the exact energy density functional is the exact many-body ground-state density; therefore we need to minimize the functional in Eq. (2.8) with respect to the density. The derivation will not be outlined here, but can be found in Ref. 29. Doing so, we end up with

$$\left(-\frac{1}{2}\nabla^2 + V_{\text{ext}} + V^s_{\text{Hart}} + V_{\text{XC}}\right)\psi_i(\mathbf{r}) = \left(-\frac{1}{2}\nabla^2 + V_{\text{KS}}\right)\psi_i(\mathbf{r}) = \epsilon_i\psi_i(\mathbf{r}), \tag{2.9}$$

where we have written the functional derivatives above as potentials, V. For each single-particle wave function, we have a single-particle Schödinger equation (called a KS equation) with an effective KS potential chosen such that the sum of the solutions ψ_i to Eq. (2.9) squared [as in Eq. (2.3)] gives the exact, many-body ground-state density. V_{KS} also depends on the density; therefore we must solve Eq. (2.9) self-consistently.

2.3 Traditional forms for the exchange-correlation potential

In principle, Eq. (2.9) gives us the exact ground-state density, but we have yet to define the XC potential, V_{XC}—in fact, there is no known form for the exact V_{XC} for all systems. However, hope is not lost. Kohn and Sham provided an approximate version called the local density approximation (LDA).[31] $V_{\text{XC}}^{\text{LDA}}$ approximates the XC at a given point $\mathbf{r}$ as that of the uniform electron gas with the same density as the KS

density $n(\mathbf{r})$ at $\mathbf{r}$. The XC potential for the uniform electron gas can be calculated exactly using quantum Monte Carlo techniques, and tabulated with respect to density. Therefore, it is a local (only depending on the density at a given point), smooth function of the density. The LDA has been amazingly successful at capturing material properties, and is both intuitive and simply parametrized.[32,33] A further development, called the generalized gradient approximation (GGA), includes terms dependent on the gradient of the density to try to better capture the difference between the homogeneous electron gas and the inhomogeneities of a real material.[34]

2.4 The self-interaction error: over-delocalization

As one may expect, the LDA and GGA functionals often fail in capturing the properties of systems whose ground state is characterized by localized and strongly interacting electrons, such as transition metal oxides and the rare-earth elements. Phenomena such as metal-insulator transitions and heavy fermion behavior are thus not captured correctly. This can be ascribed to the tendency of the XC functionals to over-delocalize valence electrons and to over-stabilize metallic ground states, as expected since the XC functional is based on the homogeneous electron gas. One example, important for the materials studied in this thesis, is the failure to correctly describe Mott insulators (see Section 1.1.4). Here, the electronic localization on atomic-like states is not described

properly, and these materials are instead predicted to be metals. Coupled with the intrinsic difficulty in modeling the dependence of the XC functional on the electronic charge density, for these materials approximate functionals generally provide a rather poor representation of the many-body terms of the electronic interactions of the N-electron ground state. Such systems with strongly interacting electrons still represent a formidable challenge for DFT, and no single scheme has been identified that is able to capture entirely the complexity of the quantum many-body problem, while maintaining a sufficiently low computational cost.

The over-delocalization of electrons can largely be attributed to the failure of the XC functional to cancel out the electronic self-interaction contained in the classical Hartree term. This (unphysical) self-interaction makes an electron repel itself, thus inducing an excessive delocalization of the wave functions. Consider the Hartree energy in Eq. (2.7); we can write it out explicitly in terms of single-particle wave functions (now including spin)

$$E_{\mathrm{ee}}^{\mathrm{s}} = \frac{1}{2} \sum_{i,j,\sigma_i,\sigma_j} \int d\mathbf{r} d\mathbf{r}' \psi_{i,\sigma_i}^*(\mathbf{r}) \psi_{j,\sigma_j}^*(\mathbf{r}') \frac{1}{|\mathbf{r} - \mathbf{r}'|} \psi_{i,\sigma_i}(\mathbf{r}) \psi_{j,\sigma_j}(\mathbf{r}'). \tag{2.10}$$

We see that the term in the sum where $i = j$ is the interaction between the charge density of a state with itself. The next two sections will discuss methods to correct for the self-interaction on the single-particle level, which is the level of theory employed in this thesis. Going beyond single-particle theory is required to obtain a more precise description of the many-body terms and thus a better treatment of correlation effects.

Methods and corrective approaches for this purpose have been formulated and developed in the last decades, with DFT + Dynamical Mean Field Theory (DFT+DMFT)[21] being the most commonly used, significantly improving the description of correlated systems. While being less computationally demanding than wave-function based methods (as in quantum chemistry approaches), this method is significantly more expensive than DFT.

2.5 The DFT+U approach

For a comprehensive review of DFT+U, the reader is referred to the review article by Himmetoglu *et al.*;[35] the discussion here is a brief introduction and overview. DFT+U is based on a corrective functional where the missing V_{XC} is included according to the Hubbard model,[36] essentially adding an intra-atomic energy repulsion U. It is one of the simplest approaches to improve the description of the ground state of correlated systems.[37] Due to its simplicity and low computational cost (only marginally larger than that of standard DFT calculations), DFT+U has rapidly gained popularity. This method consists of adding a Hubbard $+U$ correction to conventional functionals such as LDA or GGA.

Within DFT+U the total energy of a system can be written as follows

$$E_{\mathrm{DFT+U}} = E_{\mathrm{DFT}} + E_{\mathrm{Hub}} - E_{\mathrm{DC}} \tag{2.11}$$

Here E_{DFT} is the total energy from the functional being corrected and E_{Hub} is the term containing the Hubbard Hamiltonian. Because of the additive nature of this correction, we have to correct for the interaction energy to be modeled by E_{Hub}. This is accomplished by the subtraction of the so-called "double-counting" (DC) term E_{DC} which models the contribution of correlated electrons to the total energy as a mean-field approximation of E_{Hub}. The Hubbard and DC functionals are not uniquely defined, and different possible formulations exist. A popular approach for materials whose electrons are localized on specific orbitals is the "fully localized limit" (FLL),[38] as it is able to better capture Mott localization and open up a Mott-Hubbard gap than other implementations. It consists of an energy functional that, consistent with Eq. (2.11), can be written as

$$E_{\mathrm{DFT+U}}[\rho(\mathbf{r})] = E_{\mathrm{DFT}}[\rho(\mathbf{r})] + \sum_I \left[\frac{U^I}{2} \sum_{m,\sigma \neq m',\sigma'} n_m^{I\sigma} n_{m'}^{I\sigma'} - \frac{U^I}{2} n^I (n^I - 1) \right] \tag{2.12}$$

where $n_m^{I\sigma}$ are the occupation numbers of localized orbitals identified by the atomic site index I, state index m (e.g., running over the eigenstates of L_z for a certain angular quantum number l) and by the spin σ. Although the definition of these occupations depends on the specific implementation, they are often computed from the projection of KS orbitals on the states of a localized basis set of choice (e.g., atomic states)

$$n_{mm'}^{I\sigma} = \sum_{k,v} f_{kv}^{\sigma} \langle \Psi_{kv}^{\sigma} | \Phi_{m'}^{I} \rangle \langle \Phi_{m}^{I} | \Phi_{kv}^{\sigma} \rangle \tag{2.13}$$

where the coefficients f_{kv}^{σ} represent the occupations of KS states (labeled by k-point, band, and spin indices), determined by the Fermi-Dirac distribution of the corresponding single-particle energy eigenvalues.

2.6 Hybrid functionals

Another method to approximate the wave function and energy of a many-body system is Hartree-Fock (HF). Similarly to DFT, the interacting many-body system is replaced by single-particle non-interacting equations, but the HF method attempts to include the many-body effects by incorporating the fermionic nature of the wave function in the exchange potential. The HF "exact" exchange energy of the system is given by[39]

$$E_{\mathrm{X}}^{\mathrm{HF}} = -\frac{1}{2}\sum_{i,j,\sigma}\int d\mathbf{r}d\mathbf{r}'\psi_{i,\sigma}^{*}(\mathbf{r})\psi_{j,\sigma}^{*}(\mathbf{r}')\frac{1}{|\mathbf{r}-\mathbf{r}'|}\psi_{j,\sigma}(\mathbf{r})\psi_{i,\sigma}(\mathbf{r}') \tag{2.14}$$

where the sum goes over a single spin σ. This term looks very similar to the Hartree energy described above for KS theory (for a single spin), though because the integral over $\mathbf{r}'$ involves both ψ_i and ψ_j (the terms are "exchanged" compared to the Hartree energy), it cannot be expressed in terms of densities.

Within this framework, we reformulate the Hartree energy in Eq. (2.7) explicitly in terms of single-particle wave functions (now including spin):

$$E_{\mathrm{Hart}}^{\mathrm{s}} = \frac{1}{2} \sum_{i,j,\sigma_i,\sigma_j} \int d\mathbf{r} d\mathbf{r}' \psi_{i,\sigma_i}^*(\mathbf{r}) \psi_{j,\sigma_j}^*(\mathbf{r}') \frac{1}{|\mathbf{r} - \mathbf{r}'|} \psi_{i,\sigma_i}(\mathbf{r}) \psi_{j,\sigma_j}(\mathbf{r}'). \tag{2.15}$$

We see that the term in the sum where $i = j$ is the interaction between the charge density of a state with itself. In HF, this term is exactly canceled for each i by the exchange term [Eq. (2.14)]. From the observation that the self-interaction is canceled, hybrid functionals are constructed by adding some amount of HF exchange to a traditional functional, allowing hybrids to better describe the energetics of localized systems where self-interaction is significant. Compared to DFT+U, the method is more general since there is no assumption implicitly stating that the KS orbitals are localized—in DFT+U the KS orbitals are projected onto a localized basis set in order to calculate their occupation.

The XC energy in these hybrid functionals is given by

$$E_{\mathrm{XC}} = \alpha E_{\mathrm{X}}^{\mathrm{HF}} + (1 - \alpha) E_{\mathrm{X}}^{\mathrm{LDA/GGA}} + E_{\mathrm{C}}^{\mathrm{LDA/GGA}}, \tag{2.16}$$

where α is an adjustable "mixing" parameter. This comes with the drawback of higher computational cost (about one to two orders of magnitude) due to the explicit use of the wave functions in calculating $E_{\mathrm{X}}^{\mathrm{HF}}$. Still, systems of size up to 100-200 atoms can be simulated.

In this work we use the hybrid functional developed by Heyd, Scuseria, and Ernzerhof[40] (HSE), which has a second parameter, σ that screens the long-range part of the Hartree-Fock exchange

$$E_{\mathrm{XC}} = \alpha E_{\mathrm{X}}^{\mathrm{HF,SR}}(\sigma) + (1-\alpha)E_{\mathrm{X}}^{\mathrm{GGA,SR}}(\sigma) + E_{\mathrm{X}}^{\mathrm{GGA,LR}}(\sigma) + E_{\mathrm{C}}^{\mathrm{GGA}}, \tag{2.17}$$

where the HF exchange is now replacing only the short-range exchange of the GGA XC. [Specifically, the GGA functional developed by Perdew, Burke, and Ernzerhof[34] (PBE) is used for the GGA XC part of HSE.] The motivation behind the screening is that exchange effects occur on a short-range scale, which also reduces the complexity of the exchange term, making calculations of practical systems feasible.

In general, hybrids provide an improved description of the electronic structure of semiconductors and insulators compared to LDA/GGA.[41] They open up gaps in Mott insulators,[42] and improve the accuracy of electronic and structural properties for a wide range of materials.[43,44] The gap in a given material has an approximately linear dependence on the α parameter in Eq. (2.17). The default value for HSE is 0.25,[40] which is the value used to obtain all the results in this thesis. If the band gaps of the studied materials are well established, it is also common practice to fit α so that the correct band gap is reproduced.

2.7 The band-gap problem

In Section 2.4 we discussed the shortcomings of traditional DFT related to the self-interaction error, motivated by the failure of obtaining a band gap for systems where strong electron-electron interactions are the cause of the gap opening (Mott insulators). However, traditional DFT has another problem which we must address: it significantly underestimates band gaps of conventional semiconductors and insulators (where the band gap can be understood from band theory), often by 50% or more. In DFT, the band gap is often calculated from the eigenvalues of the single-particle KS equations [Eq. (2.9)]: the energy difference between the highest occupied single-particle state and the lowest unoccupied state, i.e., between the valence-band maximum (VBM) and the conduction-band minimum (CBM). This is defined as the "KS band gap". We must therefore examine the physical meaning of these single-particle states. The derivation in Section 2.2 guaranteed only the correspondence between the KS and exact many-body ground-state density and total energy (for an exact V_{XC}). No such guarantee for physical significance was made regarding the eigenvalues and single-particle wave functions.

It can be shown that for an exact V_{XC} the highest occupied single-particle eigenvalue correctly gives the negative ionization energy,[45] but others may not represent the true energies for adding or removing electrons from the system. The best we can do is to show empirically and by perturbatively adding quasiparticle interactions[46] that the KS

eigenvalues are in fact a close approximation. However, even if we assume that the single-particle wave functions and eigenvalues are physically significant, the band gap may not be, since it is an excited-state property. In Section 2.2 we pointed out that HK theory states that any excited-state property can be found from the ground-state density, but we do not have an obvious method to obtain the excited-state properties from the density.

To see why the band gap is underestimated in DFT, we consider a semiconductor with N singly occupied valence bands, with the VBM represented by $\epsilon_N^{\mathrm{KS}}(N)$ and the CBM by $\epsilon_{N+1}^{\mathrm{KS}}(N+1)$, so we can write the gap as:

$$E_{\mathrm{gap}} \equiv \epsilon_{N+1}^{\mathrm{KS}}(N+1) - \epsilon_N^{\mathrm{KS}}(N) \tag{2.18}$$

where $\epsilon_p^{\mathrm{KS}}(q)$ denotes the p^{th} Kohn-Sham eigenvalue in a system with q electrons. We go on to define:

$$E_{\mathrm{gap}}^{\mathrm{KS}} \equiv \epsilon_{N+1}^{\mathrm{KS}}(N) - \epsilon_N^{\mathrm{KS}}(N) \tag{2.19}$$

$$\Delta_{\mathrm{XC}} \equiv \epsilon_{N+1}^{\mathrm{KS}}(N+1) - \epsilon_{N+1}^{\mathrm{KS}}(N). \tag{2.20}$$

Therefore:

$$E_{\mathrm{gap}} = E_{\mathrm{gap}}^{\mathrm{KS}} + \Delta_{\mathrm{XC}}. \tag{2.21}$$

$E_{\mathrm{gap}}^{\mathrm{KS}}$ is the KS band gap, the energy difference between the CBM and VBM, and Δ_{XC} accounts for the shift in the CBM when it becomes occupied by an electron. For

LDA/GGA, Δ_{XC} is *zero*. In a macroscopic material the neutral excitation of a single electron is an infinitesimal perturbation to the electron density of the system, and in LDA/GGA the XC functional is parameterized from the homogeneous electron gas, meaning that the contributions from the many-body effects in LDA/GGA are zero. This is known as the "derivative discontinuity",[47,48] which takes it name from the fact that for the *exact* functional the band gap can be written as the difference between the derivatives of the total energy with respect to particle number in the limits approaching N from above and below [see Eq. (64) in Ref. 49]. There are methods to overcome the band-gap problem. The hybrid functional approach is one, but it is still a single-particle theory. A common approach to evaluate excited state properties is the GW method.[50] Here a nonlocal self-energy term replaces the local XC potential, and quasi-particle Green's functions are calculated in order to take into account the presence of an extra particle.

2.8 The practical implementation of DFT

The final topic in this Chapter explains how the KS equations are solved in DFT codes, and how the results in this thesis were obtained. All calculations were done with the Vienna *Ab initio* Simulations Package (VASP)[51] using the HSE[40] functional unless otherwise explicitly stated.

The first practical aspect of numerically solving the KS equations is to choose a basis set in which to parametrize the wave functions. Our choice is plane waves, which requires periodic boundary conditions, appropriate for simulating solids. The accuracy of the expansion increases monotonically with the highest-energy plane wave included, specified by an energy cutoff parameter, making it easy to check for convergence. This is not the case with all basis sets; increasing the size of a gaussian basis set (often used in quantum chemistry), for example, does not guarantee systematic convergence.[29] Another advantage is that integrals with plane waves are relatively simple to perform numerically using Fast Fourier Transforms. One serious drawback, however, is that a very large number of plane waves is required to describe the rapidly varying potential of the atomic nuclei and core electrons. We overcome this problem by using "pseudopotentials" that reproduce the long-range behavior of the full, all-electron potential. Specifically, the calculations in this thesis use pseudopotentials generated by the Projector Augmented Wave (PAW)[52] method.

The combination of plane waves and periodic boundary conditions allows the KS equation to be efficiently solved in reciprocal space. Many important quantities, such as the total energy, can therefore be expressed as a sum over k-vectors in the first Brillouin Zone (BZ) of the simulation cell. Regarding the choice of k-vectors, it was shown, first by Baldereschi[53] and later by Chadi and Cohen[54] and Monkhorst and Pack (MP)[55] that we can take advantage of the symmetry of the system to determine which k-points will

give us the best approximation to a full integration over the BZ. We simply have to define a mesh of points in three dimensions, and use the MP procedure to choose the vectors giving the highest accuracy BZ integration. We must also check for convergence with respect to the density of the mesh.

We also have to consider the practical implications of using periodic boundary conditions. Their use means that we can simulate the properties of an infinite bulk crystal using only the unit cell. If one wants to simulate surfaces, interfaces, and point defects, one has to construct a supercell based on several unit cells, carefully considering the effect of its periodic images. For example, for a surface one constructs a supercell containing unit cells of the material and a vacuum region, and one has to ensure that the vacuum region is large enough to avoid interactions between the two surfaces. Similarly, if one wants to simulate a single interface one must make sure that the bulk regions of the materials are large enough to avoid interface-interface interactions, and in order to simulate a point defect or impurity the size of the supercell must be increased until the interactions between defects in nearby cells are sufficiently small.

Chapter 3

Criteria for the design of complex oxide interfaces

3.1 Introduction

As outlined in Chapter 1, the complex oxides have recently emerged as an attractive materials system for devices containing extremely high charge densities, with the vast majority of the research centered on the 2DEG at the $SrTiO_3/LaAlO_3$ (STO/LAO) interface.[6–8] There has also been recent developments using rare-earth titanates interfaced with STO; $GdTiO_3$ (GTO)[9] and $SmTiO_3$.[10] The materials and heterostructures that have been explored to date are clearly only a small subset of the vast number of materials combinations that could, in principle lead to interesting phenomena. System-

atic experimental exploration of all of these combinations is clearly unfeasible—not least because high-quality growth techniques have proven essential to bring out the unique properties.[9,56] Computations and simulations can greatly assist in the process of identifying suitable prospects: first and foremost, by building greater understanding of the phenomena, so that searches can be better informed and more focused (which we will see in practice for the STO/GTO interface in Chapter 4)—but also by screening and exploring a greater number of materials and junctions than is experimentally practical. Such a search should be guided by a set of criteria that the materials and their heterostructures should satisfy to develop a high-performance 2DEG-based device.

In this Chapter we propose a list of physical criteria that complex oxides and their interfaces should meet and explain how these requirements can be used in conjunction with electronic structure theory and device simulations to intelligently sort through candidate systems. We will illustrate the approach with select examples using first-principles calculations based on density functional theory (DFT), for which the theory was laid out in Chapter 2. In particular, we present comprehensive data for band alignments across a range of oxides that are being considered as candidate materials. Since the band offsets at heterojunctions control confinement, accurate knowledge of these quantities is a prerequisite for device design.

The attention that has been focused on oxides and their interfaces is of course based on the tremendous progress that has been made in epitaxial growth.[6,57–59] These achieve-

ments provide us with confidence that sensible proposals for new structures based on computational designs stand a good chance of being experimentally executable.

Section 1.2 discusses the fundamentals of formation of a 2DEG at an interface, particularly the case where electrons are provided by "polar-discontinuity doping." In Section 3.2 we present the list of criteria. Section 3.3 elaborates on band alignments, first explaining the first-principles methodology, then summarizing the results. Section 3.4 summarizes the Chapter and provides an outlook.

3.2 Criteria

In this section we describe a set of key parameters and criteria that determine the formation of a 2DEG at a given interface, or influence the 2DEG characteristics. These include the structural quality, the polar/nonpolar discontinuity at the interface, the electronic structure of the individual materials, band alignments, and parameters that affect the mobility of the electrons in the 2DEG.

3.2.1 Structural quality

Lattice parameters.

The lattice parameters of the materials to be joined at an interface should be close enough to allow for strong epitaxial bonding without formation of misfit dislocations.

Perfect matching is not required; in fact, a slight lattice mismatch can be advantageously used to induce pseudomorphic strain that can be used in band-structure engineering, as discussed in Section 3.2.5 below. Strain has also been found to be a useful parameter to affect other properties such as ferroelectricity, as has been established both experimentally[60] and computationally.[61]

Point defects.

Point defects, in particular oxygen vacancies, have often been invoked as sources of electrons in the STO/LAO 2DEG.[62–66] Previous first-principles calculations indicate that both in STO and LAO oxygen vacancies have relatively high formation energies.[67,68] However, this is an issue that would need to be evaluated in new materials being considered for heterostructures, and the methodology for addressing point defects is well established.[49,69] In Chapter 5 we will present a study of native defects and impurities in GTO, highlighting their role in forming small hole polarons, which influence the electronic behavior of the material.

Intermixing.

Cation intermixing has been shown to occur for STO/LAO interfaces,[70,71] and recent experiments also indicate a strong effect of cation (non)stoichiometry on the 2DEG density;[72] such intermixing or (non)stoichiometry will interfere with the ability to ob-

tain the full density 2DEG. Based on DFT calculations (in the generalized gradient approximation) Qiao *et al.*[71] reported that intermixed interfaces are thermodynamically more stable than abrupt interface. This is a common feature at semiconductor interfaces; it does not mean that abrupt interfaces cannot be obtained using suitable growth teachniques. Abrupt STO/GTO interfaces grown with molecular beam epitaxy (MBE) without evidence of intermixing have been reported.[9,73]

3.2.2 Avoiding the "polar catastrophe"

The interface between STO and LAO has often been described in terms of a "polar catastrophe".[70] This stems from regarding the system purely in terms of the ionic charges. In the description outlined in Section 1.2, no divergence of the potential occurs if the electrons that are generated by the polar discontinuity are kept (in conduction-band states) locally at the interface. A divergence in potential only occurs if a net charge is present at the interface—which would be a consequence of electrons leaking away.

Electrons will leak away if the system is such that those electrons can be transferred to unoccupied states at lower energy. When a thin layer of LAO is grown on STO, the LAO surface [which is usually AlO_2-terminated, as in Figure 3.1(a)] exhibits partially occupied surface states in the lower part of the band gap, i.e., well below the energy of the electrons in the conduction band of STO. Electrons therefore prefer to occupy those states; the transfer of electrons from the interface to the surface sets up an electric field

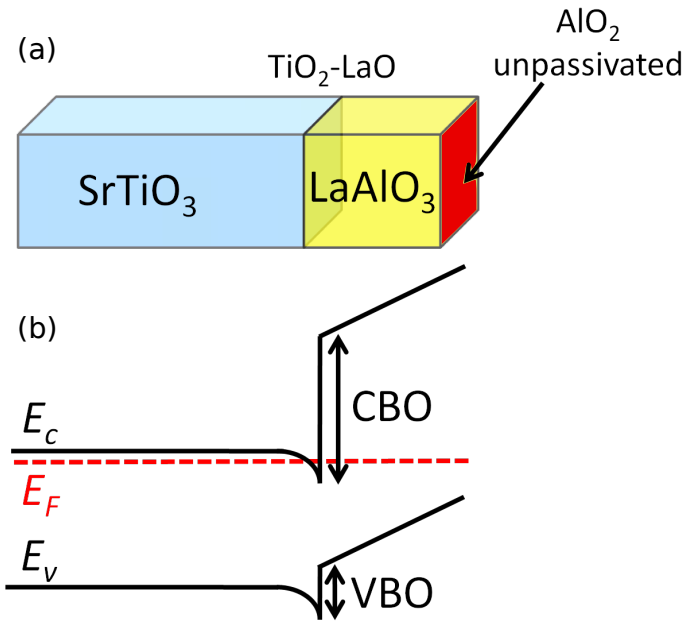

Figure 3.1: (a) Schematic of a structure with a thin $LaAlO_3$ layer on top of $SrTiO_3$. (b) Corresponding band diagram. The LAO surface serves as a sink of electrons when unpassivated, reducing the 2DEG density.

across the LAO layer, as shown in Figure 3.1(b). This leads to a potential that increases towards the surface in the LAO layer, up to the point where the partially occupied surface states cross the Fermi level. The fraction of electrons that are transferred depends on the energetic position of the surface states and the thickness of the LAO layer. Below a critical layer thickness, *all* of the electrons are transferred to the surface, consistent with experimental observations.[74] Only for large enough thickness is the potential buildup sufficient to bring the surface states above the Fermi level. This situation has often been described as charge transfer *from* the LAO surface *to* the interface,[75,76] i.e., as if the surface acts as a source of electrons. However, as should be evident from Section 1.2, the electrons actually originate at the interface.

This model was elaborated on in Refs. 26 and 77. It also explains why the observed 2DEG density at STO/LAO interfaces is one order below the expected value of 1/2 electron per unit cell.[62,65,74,78] For the present purposes, the question is: how can the loss of electrons from the interface be avoided? The key, clearly, is to avoid the presence of unoccupied states that drain away electrons from the interface. This can be addressed in two ways.

Surfaces.

If the overlayer (the layer with the larger band gap) is terminated at a surface, unoccupied surface states in the band gap should be avoided. First-principles calculations

can assess surface reconstructions and the associated electronic structure. Such calculations have been performed for many semiconducting systems (see, e.g., Ref. 79 for an example in nitrides). Aside from the recent work by my colleagues in the Van de Walle group on LAO,[80] for oxides very few studies have been performed to date. This will be a very fertile and necessary area of investigations.

It should clarify, for instance, why heterostructures with a GTO, rather than an LAO overlayer, exhibit a 2DEG with a density of 3×10^{14} cm^{-2}.[9] Clearly, the GTO surface behaves differently from the LAO surface, and first-principles calculations can address this difference. The calculations can also address how modifications of the surface could prevent surface states from serving as a sink of electrons.[26]

Interfaces.

In Ref. 26 it was demonstrated that STO/LAO/STO double heterostructures, with mirror-symmetric TiO_2-LaO interfaces, lead to a 2DEG density corresponding to 1/2 electron per unit cell at each interface. One can explain this based on the symmetry of the structure, which forces the electrostatic potential to be essentially flat across the LAO layer (as opposed to exhibiting a slope); Gauss' law then tells us that the net charge density at each interface (integrated over the width of the 2DEG) has to be zero, i.e., no electrons leak away from the interface. An alternative viewpoint is that the interface

that terminates the LAO layer does not contain any unoccupied states that can act as a sink for electrons.

In STO/LAO, growing such symmetric interfaces has proven very difficult.[81] Once again, STO/GTO has proven to be different, with superlattices containing a number of periods having been demonstrated.[9] One reason is that symmetric interfaces are inherent in the STO/GTO system, due to the TiO_2 layer that is common to both the STO and GTO structure. I.e., there is only one type of interface possible, containing an $SrO/TiO_2/GdO$ sequence of layers. In contrast, STO/LAO exhibits two types of interfaces, namely SrO/AlO_2 and TiO_2/LaO, and it is apparently not possible to control the growth process to force symmetric interfaces.

3.2.3 Electronic structure

Density of states.

Achieving a high electron density in the 2DEG obviously depends on the density of states (DOS) of the conduction band. Oxides with conduction bands comprised of transition-metal d states (as is the case in STO) will tend to provide high DOS, since d bands tend to have relatively low dispersion. Low dispersion also implies large effective mass, which could limit mobility. Fortunately, these issues can be decoupled, as discussed in Section 3.2.5 below. In oxides with conduction bands arising from sp bonding, the

DOS should be carefully evaluated. Accurate first-principles calculations provide reliable band structures, which in turn directly determine DOS. For modeling purposes, effective masses can also be extracted from the calculations.[82] It should be noted that parabolic band models are often inadequate.

wave function spread and dielectric constant.

Tight confinement of the electrons in the 2DEG is beneficial since it avoids capacitance degradation. The characteristic length for the wave-function spread decreases with increasing effective mass. Just like for the DOS, a high effective mass in the direction perpendicular to the interface is thus beneficial.

The dielectric constant is also a key parameter in confinement: the higher the dielectric constant, the less tightly the electrons are confined to the interface. An interesting complication arises due to the fact that dielectric constants can depend on the strength of the electric field.[83] The tight confinement of electrons means that the confining potential well is narrow, corresponding to large electric fields, which in turn will affect the confinement of the 2DEG near the interface. The confinement problem therefore needs to be solved self-consistently.[84] For STO, the dielectric constant is known to decrease with applied field.[85]

Breakdown strength.

To render the 2DEG useful for device applications, being able to modulate these high electron densities is essential. This requires a high breakdown strength, which is the product of dielectric constant and breakdown field.[86] Breakdown field tends to scale as the square of the band gap. Conventional semiconductors such as Si and GaAs exhibit breakdown fields on the order of 0.1 MV/cm, while the value for GaN (E_g=3.5 eV) is around 3 MV/cm. The perovskite oxides discussed here have band gaps comparable to that of GaN, so we expect a similarly high breakdown field. Since the dielectric constants of complex oxides are larger than those of conventional semiconductors, the breakdown strengths will be superior.

Metal/insulator transitions.

Some of the complex oxides in which the conduction band is comprised of d states behave as Mott insulators (discussed in detail in Chapter 1), i.e., an occupied d band is split into an occupied lower Hubbard band (valence band) and an unoccupied upper Hubbard band (conduction band). Changing the occupation of these d states can trigger a metal-insulator transition,[87] which has been proposed as the basis for a novel "charge-gain" transistor structure.[12] The physics of these Mott insulators is an active area of research, and first-principles calculations can contribute to both qualitative and quantitative understanding, as will be demonstrated in Chapter 4.

Alloying.

Forming alloys increases the flexibility in device design and band-structure engineering, as has been demonstrated with STO/$SrTi_{0.95}Zr_{0.05}O_3$ interfaces, at which modulation doping can be performed.[23] To first order, the electronic properties of alloys can be obtained by linear interpolation between the end compounds but nonlinearities (such as band-gap bowing) can often be significant, and can be obtained from first-principles calculations.[88]

3.2.4 Band alignments.

In the discussion of the STO/LAO interface in Section 1.2 and Figure 3.1, we showed a band alignment in which the conduction-band minimum (CBM) in STO lies well below the CBM in LAO. Given the large difference in band gaps between STO (3.2 eV)[89] and LAO (5.6 eV),[90] and considering that the valence-band offset is expected to be small (because the valence-band states are mainly derived from $2p$ states of oxygen, which is the common anion[91]), this seems like a reasonable assumption. However, for many other materials combinations this alignment is not *a priori* known. The alignment is a key parameter for heterojunction design, both qualitatively (since it determines which material the electrons will reside in) and quantitatively (since the CB offset needs to be sufficiently large to ensure adequate confinement).

While the alignment can be determined experimentally, very few results have been reported for oxide interfaces to date. First-principles calculations are a powerful tool for determining such alignments, as has been demonstrated in the many calculations reported for semiconductors.[92–94] Because of the importance of this topic, and to serve as an illustration of the power of the first-principles approach, we devote a separate Section of this Chapter to the band alignment problem (see Section 3.3).

3.2.5 Mobility

For electronic devices, the mobility of electrons in the 2DEG needs to be high. This is actually a major problem for many oxides: low-temperature mobility is high (32,000 $cm^2V^{-1}s^{-1}$ in STO at 1.8 K[95]) but decreases to low values at room-temperature (10 $cm^2V^{-1}s^{-1}$ in STO at 300 K[96]). While cooling to cryogenic temperatures may be acceptable in some applications, widespread adoption will clearly depend on the ability to achieve higher room-temperature mobilities. Two main factors enter: carrier effective masses and scattering.

Effective mass.

To achieve high mobility, the effective mass of carriers should be small. At first sight this seems incompatible with the requirement for a high density of states, but as pointed out in Ref. 97, clever band-structure engineering can circumvent the issue. Effective

masses may exhibit an anisotropy, either intrinsic due to the symmetry of the material, or induced by strain. The orientation of the heterostructure should then be chosen such that light electron masses occur in the in-plane direction (particularly, the transport direction), while the out-of-plane direction should exhibit heavy electron masses, which lead to large densities of states.

One way to avoid the problem of electrons occupying the Ti $3d$-derived bands would be to replace $SrTiO_3$ with a material that instead contains $4d$ or $5d$-derived bands (as in $SrZrO_3$ or $SrHfO_3$), or s or p-derived bands (as in $BaSnO_3$). The less localized nature of these states will result in smaller electron effective masses, potentially leading to higher mobilities.

Strain can be used to engineer the ordering of conduction-band valleys as well as effective masses. Strain can be induced through pseudomorphic growth, in which a material is grown epitaxially on a substrate with a different lattice constant. This leads to tensile or compressive strain as the in-plane lattice constant is expanded or contracted to match that of the substrate, and the out-of-plane lattice constant adjusts according to the elastic properties of the layer. This approach is widely used in silicon technology, particularly in SiGe heterostructures; in addition, other methods of process-induced strain have been developed in silicon technology.[98]

Understanding the effects of strain on the band structure is thus of great importance, and first-principles calculations can yield detailed and comprehensive information. For

STO, strain-induced changes of the energetic ordering and effective mass of conduction-band states results based on hybrid functional calculations (a methodology discussed in detail in Chapter 2) has been published.[82]

Scattering.

Ionized impurity scattering can lead to strong decreases in mobility; this is an important reason why modulation doping (in which carriers are located in a different spatial region from the ionized donors) is widely applied in HEMTs. One might think that the high density of effective donor centers at the polar/nonpolar interface [Figure 1.7(a)] would lead to unacceptably high scattering rates. This does not happen, however, because these charged centers are arranged in a perfectly periodic array, which does not lead to scattering—the analogy being the charged atomic cores that constitute the periodic lattice in which valence electrons move in a crystal. However, any deviation from periodicity (e.g., due to interfacial roughness) will lead to reductions in mobility.

In addition to impurity scattering, scattering from optical phonons leads to a strong reduction of mobility at finite temperatures, responsible for the large difference in mobility at low and room temperatures, as has recently been highlighted for STO.[99]

3.3 Band alignments

Band alignments of complex oxides can be obtained by a variety of experimental methods; to date, mainly x-ray photoelectron spectroscopy (PES) has been employed, but the focus has been almost exclusively on STO/LAO. First-principles theory is a powerful tool for obtaining these offsets, but the calculated values for valence-band (VB) offsets that have been reported to date differ significantly in both magnitude and sign. The sign determines whether the valence-band maximum (VBM) is higher in STO or in LAO; we adopt the convention that at an A/B interface the VB offset is positive if the VBM in B is higher in energy than in A. DFT calculations, using either the local density (LDA) or the generalized gradient (GGA) approximation, for superlattices with symmetric TiO_2-LaO terminations resulted in VB offsets of –0.15 eV (GGA),[100] 0.51 eV (LDA),[101] and 0.9 eV (GGA).[102] Qiao *et al.* (GGA)[71] also reported a VB offset of 0.7 eV for a perfect interface, and 0.2 eV for an interface that included cation intermixing.

In the following Section we will outline the methodology followed in the calculations. We note that band-alignment results are relevant not only for the case of polar-discontinuity-doped (polar/nonpolar) heterostructures, but also for interfaces between nonpolar materials, such as STO/$SrZrO_3$.[103] As noted in Section 1.2, modulation doping at STO/$SrTi_{0.95}Zr_{0.05}O_3$ interfaces was recently reported.[23]

3.3.1 Methodology

Band alignments are in principle properties of a specific interface; i.e., a new calculation should be performed for every pair of materials. In practice however, it turns out that band offsets for lattice-matched non-polar interfaces exhibit transitivity.[92,94,104] I.e., if the offsets A/B and B/C are known, the offset A/C can be derived. This implies that the offsets can be obtained based on the alignment of the band structure of each material on an absolute energy scale (e.g, with respect to the vacuum level).

Surface calculations can in principle be used to obtain this alignment.[88,105] In the present the band alignments are obtained from explicit interface calculations.[93] First, separate calculations for each bulk material are performed in which the VBM and conduction-band minimum (CBM) are determined with respect to the average electrostatic potential in the respective material. Then, the average electrostatic potentials in the two materials are aligned by performing a calculation for a superlattice and determining the difference in the average electrostatic potential in the bulk regions of the heterostructure, i.e., far enough from the interface (see Figure 3.2). Therefore, the thickness of each material in the superlattice has to be large enough to contain a bulk-like region.

In our present work, the band alignments were determined by systematically using STO as one of the materials in the interface calculations. STO was chosen because

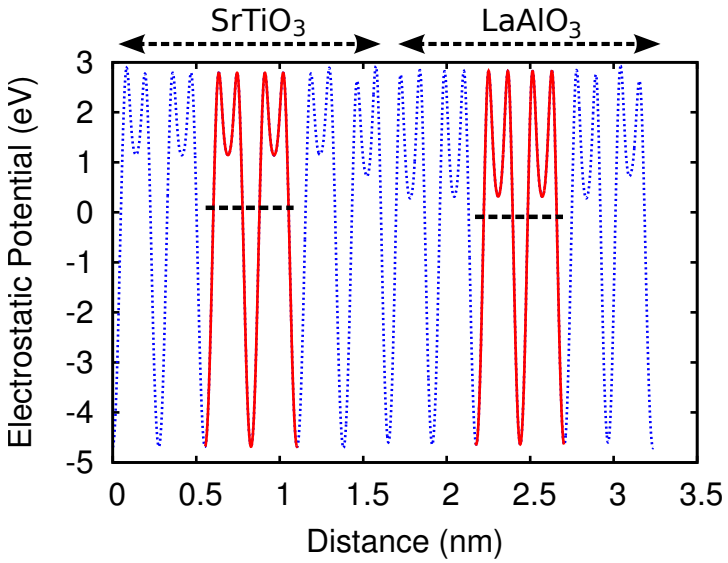

Figure 3.2: Planar-averaged electrostatic potential plotted along the [110] direction for the $SrTiO_3/LaAlO_3$ heterostructure (blue dotted line). Bulk-like regions in the center of each layer are highlighted (red solid lines), and the average potentials determined for these regions are shown as dashed black lines.

it is widely used as a substrate due to the availability of large single crystals with high crystalline quality. It also exhibits reasonably good lattice matching to the other materials considered here.

Usually the two materials have different equilibrium lattice parameters, posing an additional complication in the calculation of band alignments. In this case, the interface calculation is performed by fixing the in-plane lattice parameters to those of the non-STO material, and allow the out-of-plane lattice parameter of STO and the atomic positions near the interface (cation layer of each material, and interface oxygen layer) to relax.

In general, the volume of the STO in the superlattice will end up at a value different from its equilibrium value due to the Poisson effect, i.e., a material that is compressed (stretched) in the plane tends to expand (contract) in the perpendicular direction according to the Poisson ratio. The superlattice calculations thus provide the alignment of the electrostatic potential between strained STO and another material in its equilibrium structure. Combined with bulk calculations for STO in the same strain state, this provides the band alignment between a complex oxide in equilibrium and a strained STO overlayer.

We are often interested, however, in the "natural" band alignment between the materials at their equilibrium volume. To obtain this alignment, we have to account for the effect of the volume change in the STO. This is done by performing a similar calculation

as for the band alignment at a heterojunction, but instead calculating the alignment of the electrostatic potential between strained and unstrained volumes of the same material,[93] in a homojunction supercell with equilibrium in-plane lattice parameters.

Finally, we discuss the issue of the interface orientation. Many of the oxide interfaces grown to date have been grown along the [001] direction, where a polar discontinuity occurs at the interface. However, if we carry out the calculations for a superlattice including this polar discontinuety, we unavoidably introduce the doping due to the polar discontinuity at the interface and the compensating 2DEG, and the presence of these charges and the resulting dipole could affect the calculated band alignment. For the record, we are of the opinion that these additional effects are not part of the true intrinsic band alignment, for reasons that have been discussed at length in previous publications.[92,104] Indeed, in the absence of the polar-discontinuity-doping effects, we expect only small differences between band alignments for different orientations. This has been tested in the case of alignments between nonpolar materials, in which the 2DEG is absent in the [001] direction, and found that calculations for this direction (with up to 8 layers of each material in the superlattice) produce results that are within 0.05 eV of those obtained for [110].

One could argue that the 2DEG-related effects may be present in experimental determinations of the offsets—however, that is an issue that depends on the details of how the experiments are carried out. In the calculations, if one did include these effects by

using the [001] direction, one might also introduce additional uncertainties due to incomplete description of the 2DEG in our limited-width superlattices. Indeed, while the thickness of the layers in our superlattices is adequate to describe the rapid convergence of the electrostatic potential to its bulk value away from the interface, we do not claim to accurately describe the full spatial extent of a 2DEG.

We have avoided all these issues by performing our calculations for superlattices with an (110) interface orientation. No polar discontinuity exists in this orientation, since the planes parallel to the interface are composed of $(SrTiO)^{4+}$ and $(O_2)^{4-}$ on the STO side and, for example, $(LaAlO)^{4+}$ and $(O_2)^{4-}$ on the LAO side. For the cubic oxides we used superlattices containing 6 layers of each material in the [110] direction, with an in-plane area of $a \times \sqrt{2}a$, and for the distorted oxides we used a superlattice with 5 layers of each material with in-plane area $2a \times \sqrt{2}a$ in order to accommodate the lattice distortions. Convergence tests as a function of layer thickness indicated that increasing the thickness of each material from 6 layers to 8 layers for the cubic materials changed the potential alignment by less than 0.05 eV, and for the distorted materials increasing the layers from 5 to 7 changed the potential alignment by less than 0.1 eV.

3.3.2 Results for bulk materials

We considered ABO_3 perovskite oxides, with A=Ca, Sr, Ba, La, K, Y, and Gd, and B=Ti, Zr, Hf, Al, Ta, and Sn, as listed in Tables 3.1 and 3.2. The materials investigated

can be divided into cubic band insulators, distorted band insulators, and distorted Mott insulators. The choice of materials covers B-site transition metals from the $3d$, $4d$, and $5d$ rows (Ti, Zr, Hf, and Ta). The valences include +1, +2, and +3 for the A site, and +3, +4, and +5 for the B site. This also allows for comparing materials with conduction bands derived from d states versus s states (as in the case of $BaSnO_3$, $SrSnO_3$, and $CaSnO_3$).

The band insulators can be divided in nonpolar and polar according to the charge of the alternating planes along the [001] direction: STO, $BaTiO_3$ (BTO), $CaTiO_3$ (CTO), $SrZrO_3$ (SZO), $SrHfO_3$ (SHO), $BaSnO_3$ (BSO), $SrSnO_3$ (SSO), and $CaSnO_3$ (CSO) are nonpolar since the alternating planes consisting of either AO or BO_2 are all charge neutral. LAO and $KTaO_3$ (KTO) are polar: LAO is composed of alternating planes of $(LaO)^+$ and $(AlO_2)^-$, and KTO is composed of $(KO)^-$ and $(TaO_2)^+$. The Mott insulators, $YTiO_3$ (YTO) and GTO are also polar materials along the [001] direction, with alternating planes of $(TiO_2)^-$ (Ti assumes valence +3 in these Mott materials) and $(YO)^+$ or $(GdO)^+$. We remind the reader that our band-offset calculations are all carried out with an (110) interface orientation, which does not exhibit any polar discontinuity.

For bulk calculations we considered both the 5-atom simple cubic perovskite unit cells ($a \times a \times a$, where a is the lattice constant) and 20-atom distorted $GdFeO_3$ unit cells (roughly $\sqrt{2}a \times \sqrt{2}a \times 2a$). The latter allow for octahedral rotations and tilts that are characteristic of the room-temperature phase for a number of the complex oxides

Table 3.1: Calculated and experimental lattice constants and band gaps of studied oxides in the simple cubic structure at room temperature. The simple cubic structure has an indirect ($R \rightarrow \Gamma$) band gap; the direct ($\Gamma \rightarrow \Gamma$) band gap is given in parentheses.

		Calculated			Experimental		
		a	E_g^{ind}	E_g^{dir}	a	E_g^{ind}	E_g^{dir}
Material		(Å)	(eV)	(eV)	(Å)	(eV)	(eV)
$SrTiO_3$	STO	3.903	3.27	3.63	3.905[106]	3.20	3.75[89]
$BaTiO_3$	BTO	3.992	3.13	3.22	3.992[107]		3.20[108]
$KTaO_3$	KTO	3.994	3.40	4.36	3.988[109]	3.64	4.35[110]
$LaAlO_3$	LAO	3.787	4.88	5.04	3.791[111]		5.6[90]
$BaSnO_3$	BSO	4.130	2.40	2.88	4.119[112]		3.1[112]

Table 3.2: Calculated and experimental lattice constants and band gaps of oxides stable in the $GdFeO_3$ distorted phase at room temperature. Note that $GdTiO_3$ and $YTiO_3$ are Mott insulators, with band gaps still debated in the literature. The band gap is direct for the $GdFeO_3$ structure.

		Calculated				Experimental			
		a	b	c	E_g^{dir}	a	b	c	E_g^{dir}
Material		(Å)	(Å)	(Å)	(eV)	(Å)	(Å)	(Å)	(eV)
$CaTiO_3$	CTO	5.363	5.445	7.627	3.84	5.380	5.442	7.640[113]	3.57[114]
$SrZrO_3$	SZO	5.786	5.833	8.198	5.36	5.791	5.811	8.196[115]	5.6[116]
$SrHfO_3$	SHO	5.752	5.783	8.153	5.76	5.752	5.765	8.134[115]	6.1[116]
$CaSnO_3$	CSO	5.511	5.675	7.892	4.31	5.532	5.681	7.906[117]	4.4[118]
$SrSnO_3$	SSO	5.711	5.725	8.090	3.55	5.708	5.704	8.066[119]	3.93[120]
$GdTiO_3$	GTO	5.350	5.726	7.624	2.05	5.393	5.691	7.664[121]	–
$YTiO_3$	YTO	5.324	5.697	7.611	2.11	5.316	5.679	7.611[121]	–

considered in the present work (see Table 2). The calculations for the 5-atom cubic unit cell were performed using a 6×6×6 Γ-centered k-point mesh, and the calculations for the 20-atom cells were performed using a 4×4×2 k-point mesh.

As discussed in Section 1.1.4, in the Mott insulators GTO and YTO the VBM and CBM are derived from the Ti 3*d* states. Here the Ti atoms assume the +3 oxidation state, in contrast to the titanate band insulators discussed above in which the Ti atoms assume the +4 oxidation state. Starting from STO, replacing Sr by Y or Gd results in one extra electron per Ti that would occupy the conduction band. This extra electron causes the degenerate Ti bands to split in an occupied lower Hubbard band, constituting the valence band, and an empty upper Hubbard band, which constitutes the conduction band. This opening of a gap is accompanied by a structural distortion, with rotations and tilts of the TiO_6 octahedra; the size of the gap strongly depends on the lattice distortion.

The primitive cell of GTO and YTO contains 20 atoms, i.e., four formula units, as they both are stable in the $GdFeO_3$ distorted phase. Spin polarization is essential in the description of the ground state of GTO and YTO: the lower Hubbard band and the upper Hubbard band occur in the same spin-up channel, with a ferromagnetic ordering of the Ti moments.

3.3.3 Results for band alignments

The calculated band alignments are shown in Figure 3.3 and listed in Tables 3.3 and 3.4. In the band insulators the valence band is composed mainly of O $2p$ states, with the VBM at the R point $\pi/(2a)(\pm1,\pm1,\pm1)$ of the Brillouin zone of the cubic crystal structure. Because of the similarity of these valence-band states, one might expect them to be approximately aligned (an expectation that formed the basis for the "common-anion" rule for band offsets[91]). Figure 3.3 indeed shows that the variation of the VBM (and the O $2p$ edge for the Mott insulators) across the different materials is generally smaller than the variation of the CBM; still, the position of the VBM varies by as much as 1.2 eV, and thus a blanket application of the common-anion rule would lead to significant inaccuracies. The larger variation of the CBM reflects the variety in cations in these perovskites. For instance, in the case of STO the CBM is derived from the Ti $3d$ t_{2g} states, while in SZO it is derived from Zr $4d$ t_{2g} states. Atomic Zr $4d$ states are higher in energy than Ti $3d$ states,[24] placing the CBM in SZO at a higher energy than in STO. The CBM of SHO lies even higher. While insights like this are very useful to analyze and predict trends, quantitative results require full-fledged calculations.

For STO/LAO interfaces, a number of experimental results have appeared in the literature, all obtained with PES: Chambers *et al.*[122] reported a VB offset for STO/LAO of +0.24±0.20 eV; Qiao *et al.*:[123] 0.16±0.10 eV; Segal *et al.*:[124] 0.35±0.18 eV, and

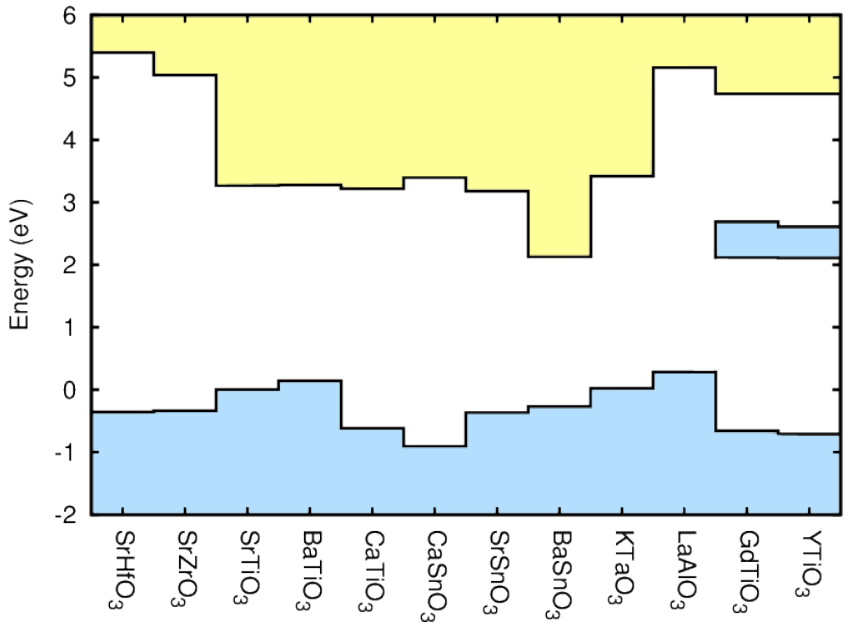

Figure 3.3: Natural band alignments for oxides considered in the present work. The valence-band maximum of STO was used as the zero of energy.

Table 3.3: Natural band alignments between band insulators and STO. Valence- and conduction-band offsets (VBO and CBO) are referenced to the STO band edges.

Material	VBO (eV)	CBO (eV)	Material	VBO (eV)	CBO (eV)
$SrHfO_3$	–0.36	2.13	$BaSnO_3$	–0.27	–1.14
$SrZrO_3$	–0.34	1.74	$SrSnO_3$	–0.37	–0.09
$BaTiO_3$	0.14	–0.01	$KTaO_3$	0.02	0.15
$CaTiO_3$	–0.62	–0.05	$LaAlO_3$	0.28	1.89
$CaSnO_3$	–0.91	0.13			

Table 3.4: Natural band alignments between Mott insulators and STO. Offsets are given for the O 2*p* edge and the minimum and maximum of the lower Hubbard band (all referenced to the VBM of STO), and for the bottom edge of the upper Hubbard band (referenced to the CBM of STO).

	O 2*p* (eV)	LHB-bottom (eV)	LHB-top (eV)	UHB (eV)
$GdTiO_3$	–0.66	2.12	2.69	1.47
$YTiO_3$	–0.71	2.11	2.61	1.47

Berner *et al.*:[125] 0.35±0.10. All of these values are in reasonable agreement with our calculated VBO of 0.28 eV. PES measurements of the STO/SZO band alignment produced a VBO of –0.5 eV,[103] again close to our calculated value of –0.34 eV. For the Mott insulator GTO, our calculated offset between the VBM of STO and the top of the LHB is 2.69 eV, in good agreement with the measured value of 2.94 eV,[126] lending further support to our approach.

3.3.4 Discussion

As described in Section 1.2, a 2DEG can spontaneously form at a polar/nonpolar heterostructure. For the materials discussed in this manuscript, this includes a combination of any of the nonpolar band insulators with the polar LAO or KTO, or with the Mott insulators GTO or YTO. The band alignments reported in the previous Section then determine on which side of the interface the 2DEG will reside—and whether the

magnitude of the offset is sufficient to provide adequate confinement. For instance, the 0.17 eV offset between STO and KTO may only be marginal. This offset results in the interface electrons being confined to the STO. By combining KTO with, for example, SZO as a barrier, the electrons will be confined within KTO. This would both minimize the lattice mismatch compared to the STO/KTO case, and result in a 2DEG residing in higher-mobility KTO Ta 5d states.

Other potentially interesting combinations involve the stannates. BSO has already been flagged as a promising transparent conducting oxide material because of its high conductivity,[127] with a CBM consisting of Sn s states. According to our band alignments, a heterojunction with KTO or LAO would create a 2DEG situated on the BSO side. Another way of increasing electron mobility would be to have the 2DEG reside in a material with conduction bands derived from $4d$ or $5d$ such as SZO or SHO, since such d states are less localized (and hence more dispersive) than the $3d$ states of STO. But due to the high-lying conduction band energies of these two materials, this might be difficult to achieve in practice.

The STO/GTO interface was the first interface to exhibit a full 2DEG density (1/2 electron per unit cell area) as expected from the polar discontinuity.[9] In accord with the band alignment shown in Figure 3.3, the 2DEG resides on the STO side of the interface, and the Mott insulator GTO serves as a potential barrier. We expect this to hold in the case of STO/YTO as well, due to the similar band gap and band alignments. To

achieve a "charge-gain" transistor structure[12] in which the electron density in GTO or YTO can be modulated would require a band insulator with a CBM significantly higher than in STO; possibly SHO. Alternatively, Mott insulators with lower *d*-state energies could be explored.

3.4 Summary

The design of novel complex-oxide heterostructures can greatly benefit from first-principles calculations. We reported hybrid density functional calculations for band alignments, which are useful for assessing and analyzing all types of heterostructures, including those in which a 2DEG would be formed by extrinsic doping as well as those exhibiting a polar discontinuity that leads to spontaneous formation of a 2DEG. We also proposed a list of criteria to screen useful heterostructures, highlighting in which areas first-principles calculations can contribute. The examples that were discussed illustrate that the first-principles computational approach can fruitfully contribute to the design of novel complex oxide heterostructures.

Chapter 4

The metal-insulator transition in $SrTiO_3$ quantum wells

4.1 Introduction

As explained in Chapter 1, experiments in the group of Prof. Susanne Stemmer have revealed the formation of a two-dimensional electron gas (2DEG) at the interface between the band insulator $SrTiO_3$ (STO) and the Mott insulators $GdTiO_3$ (GTO) $SmTiO_3$ (SmTO), with an electron density of 1/2 electron per unit-cell area.[9,10] The 2DEG resides on the STO side, and the electron density ($\sim 3\times10^{14}$ cm^{-2}) is more than one order of magnitude higher than those obtained using conventional semiconductors, opening a path towards novel electronic device applications, as described in Chapter 3. For

the STO/GTO heterostructures, sheet resistance measurements indicate a remarkable dependence of the electronic structure on the thickness of the STO: GTO/STO/GTO structures are metallic if the STO is three or more layers thick, but insulating for fewer layers.[27,128] This metal-to-insulator transition with decreasing STO layer thickness and increasing 3D electron density has been attributed to on-site Mott-Hubbard-type correlation physics, where a correlation-induced mass enhancement is followed by a transition to a correlated insulator.[27] This observation is corrobrated by measurements of the distortons of the atomic positions, which are found to be larger than what would be expected from simple lattice geometrical considerations based on the bulk structure.[10,73] Computational studies for one-layer-thick STO[129] have also been reported. However, the microscopic mechanisms that trigger the change in the electronic structure with STO layer thickness are yet to be fully explored.

The specific question we will address here is why and how GTO/STO/GTO structures become insulating when the STO thickness is reduced to one or two layers. We show that for a sufficiently high number of STO layers a 2DEG forms at each interface, but that once the number of layers become small enough the excess electrons localize within the interface TiO_2 planes. Building on suggestions in the experimental papers,[10,27] we attribute this transition to the high electron density in the STO conduction band, coupled with large structural distortions at the interface.

Bulk STO is stable in a cubic perovskite crystal structure at room temperature, described by a 5-atom cubic unit cell (space group $Pm\bar{3}m$). Bulk GTO is stable in a $GdFeO_3$ crystal structure (space group $Pbnm$), described by a 20-atom orthorhombic unit cell which includes rotation and tilts of TiO_6 octahedra. We use the hybrid functional methodology outlined in Chapter 2 to simulate these bulk cells. The Gd f electrons were included in the pseudopotential. Integrations over the Brillouin zone are replaced with sums over a mesh of 6×6×6 Γ-centered special k-points for STO, and 4×4×2 for GTO, both with a 500 eV plane-wave basis set energy cutoff.

For STO, the calculated lattice parameter of 3.903 Å is within 0.1% of the experimental value,[106] and the indirect and direct band gaps are 3.27 eV and 3.63 eV, close to the experimental values of 3.25 eV and 3.75 eV.[89] The HSE functional also gives an accurate description of the lattice parameters of GTO, giving 5.350 Å, 5.726 Å, and 7.624 Å, each within 0.8% of the experimental lattice parameters.[121] The band gap in GTO derives from a splitting of the Ti 3d derived bands into an occupied lower Hubbard (LHB) band and an empty upper Hubbard band (UHB), as explained in Chapter 1. These Hubbard bands occur in the same spin channel, so that the magnetic moments on the Ti atoms exhibit ferromagnetic ordering, consistent with experiment.[130,131] The LHB and UHB have relatively low dispersion, and the calculated Mott-Hubbard gap is 2.02 eV. This value is markedly different than the commonly accepted experimental value of 0.7 eV,[59,132,133] and Chapter 5 reexamines the electronic structure of GTO in

detail, concluding that the 2 eV value is indeed correct. We are therefore confident that we are correctly simulating both bulk materials of the STO/GTO heterostructures.

We investigate the evolution of the electronic structure of GTO/STO/GTO heterostructures as a function of decreasing STO thickness by carrying out calculations for $(\mathrm{STO})_n/(\mathrm{GTO})_3$ superlattices, with $n = 6$ to 1. A 2×2×1 k-point mesh is used with a 500 eV plane-wave cutoff for relaxations, and electronic properties are calculated with a 4×4×1 k-point mesh with a 400 eV plane-wave cutoff. The direction perpendicular to the interface is [001] in the coordinate systems of both the STO and GTO unit cells. To allow for the type of octahedral rotations and tilts as in bulk GTO, the in-plane area is thus $\sqrt{2}a \times \sqrt{2}a$, where we fix a to the lattice parameter of STO. Each interface in the superlattice thus provides one excess electron going into the STO. Internal atomic positions and the lattice parameter perpendicular to the interface are allowed to relax. We use an odd number of GTO layers in order to make the interfaces symmetric, while satisfying the periodic boundary conditions and the connectivity of the octahedra. A comparison between $(\mathrm{STO})_1/(\mathrm{GTO})_3$ and $(\mathrm{STO})_1/(\mathrm{GTO})_5$ superlattices indicates that a greater GTO thickness leads to very small changes in the electronic and atomic structure: the width of the GTO LHB changes by less than 0.02 eV, and bond angles by less than 0.5°.

4.2 Results

4.2.1 Thick STO layers: Metal

We start by presenting the results for thicker STO layers. In Figure 4.1(a) we show the electronic band structure of $(STO)_6/(GTO)_3$ in the energy range comprising the LHB and UHB of GTO, also encompassing the STO conduction band. Our results show that $(STO)_6/(GTO)_3$ has a metallic state confined to the STO layer, indicative of the 2DEG. The STO subbands can be clearly distinguished from the GTO LHB, which consists of four bands derived from the $3d$ states associated with the four Ti atoms within the bulk GTO. We note that there is a sizable spin splitting of the STO conduction band, with the majority of the electrons in the 2DEG occupying spin-up bands, and a small fraction occupying spin-down bands near the Fermi level. The spin splitting is in fact so large that the partially occupied STO conduction band overlaps the GTO LHB.

The crystal structure and the electronic charge density associated with the STO subbands in the $(STO)_6/(GTO)_3$ superlattice are shown in Figure 4.2(a). The TiO_6 octahedra in the interfacial plane on the STO side exhibit large rotations in order to accommodate the connectivity across the interface. Octahedra deeper in the STO layer are close in structure to those in bulk STO; the relaxation largely occurs within a single interface TiO_2 plane. Two electrons occupy the STO conduction band, forming a 2DEG

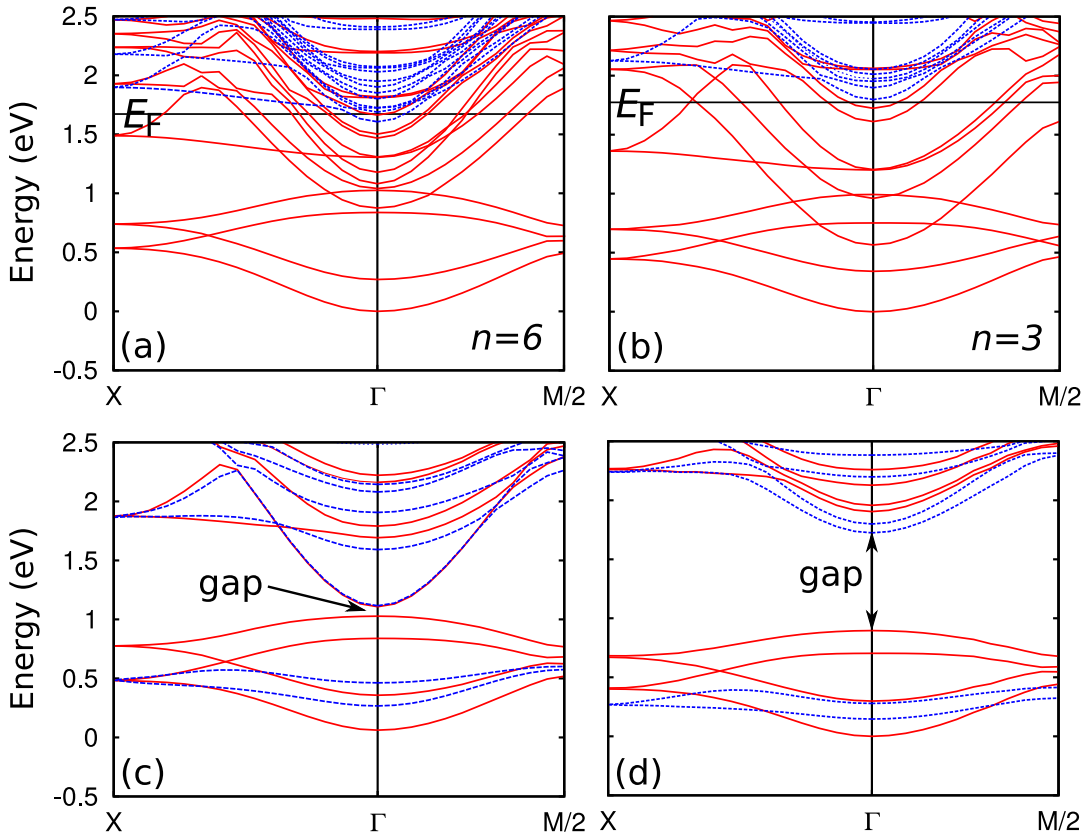

Figure 4.1: Electronic band structure of $(GdTiO_3)_3/(SrTiO_3)_n$ superlattices for (a) n=6, (b) n=3, (c) n=2, and (d) n=1. The bands are plotted along the in-plane directions $\Gamma \rightarrow$ M/2 and $\Gamma \rightarrow$ X, where M=($\frac{1}{2}$,$\frac{1}{2}$,0) and X=($\frac{1}{2}$,0,0), with coordinates referenced to the reciprocal basis vectors of the cubic perovskite 5-atom primitive cell. The energy axis is referenced to the bottom of the $GdTiO_3$ lower Hubbard band. Solid black line indicates Fermi level in the case of metallic systems (n=6 and n=3). Red (solid) indicates spin up, and blue (dashed) indicates spin down.

with a density corresponding to 1/2 electrons per 5-atom unit-cell area per interface, consistent with having two identical STO/GTO interfaces.

The charge density reveals that the orbital character of the occupied subbands varies depending on the position in the structure: In the two TiO_2 planes nearest to the interface the orbital character is d_{xy}, while it is d_{yz} and d_{xz} deeper in the STO. A consequence of the different orbital character is that the planar-averaged electron density [Figure 4.2(b)] appears narrower and more peaked in the two TiO_2 planes nearest to the interface; the double-peaked structure in the interior of the STO reflects the d_{yz}/d_{xz} nature. Macroscopic averaging (running average along the z direction over one period of the lattice)[134] reveals, however, that the distribution of the electrons is quite uniform among the different TiO_2 planes in the STO layer.

Figure 4.3 compares the calculated superlattice band structure with an angle-resolved photoemission plot (ARPES) obtained by a team of experimental collaborators in the group of Prof. Charles Fadley, performed on superlattices grown in the group of Prof. Susanne Stemmer.[135] There is in general excellent agreement as to where one expects to see intensity, including the more localized nature of the 2DEG in k-space. The ARPES measurements probe the 2DEG in the multilayer, as well as the position of the LHB in the GTO with respect to the 2DEG and the bands associated with the oxygen $2p$ orbitals. The calculated density of states was also compared with hard x-ray photoemission measurements, finding good agreement (Figure 4.4). These results

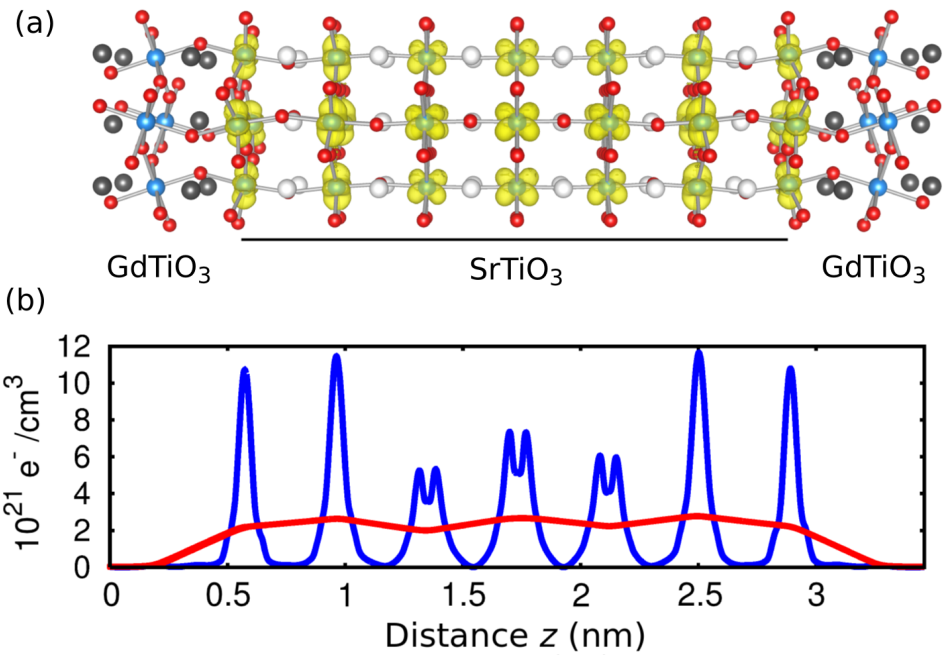

Figure 4.2: (a) Charge density of the occupied $SrTiO_3$ conduction bands (isosurface plotted at 10% of maximum value) and (b) in-plane averaged electron density (blue) and macroscopic average (red) for the $(GdTiO_3)_3/(SrTiO_3)_6$ superlattice.

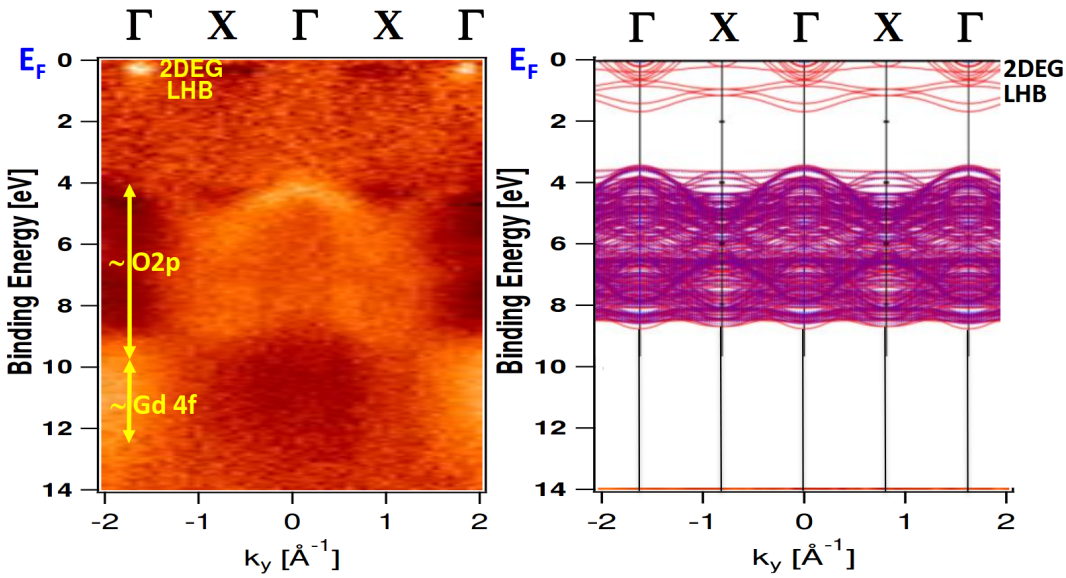

Figure 4.3: Comparison of an ARPES map obtained in the group of Prof. C. Fadley on an $(STO)_6/(GTO)_3$ superlattice grown in the group of Prof. S. Stemmer[135] with the band structure from Figure 4.1(a) shown along the Γ-X-Γ-X-Γ directions.

give us confidence that we are able to simulate the metallic STO/GTO interface, as the positions of the GTO LHB and the 2DEG are consistent with the measurements.

For smaller STO thicknesses, down to $(STO)_3/(GTO)_3$, we also find a metallic ground state with integrated charge corresponding to 1/2 electron per unit-cell area per interface. For the three-layer case, the rotations of the octahedra are again large in the interfacial layer, relaxing towards cubic in the interior of the STO [Figure 4.5(a)]. In contrast to the six-layer case, the in-plane macroscopic average of the electron density is now distinctly higher at the interface [Figure 4.5(b)], with smaller contributions from the TiO_2 planes inside the STO layer.

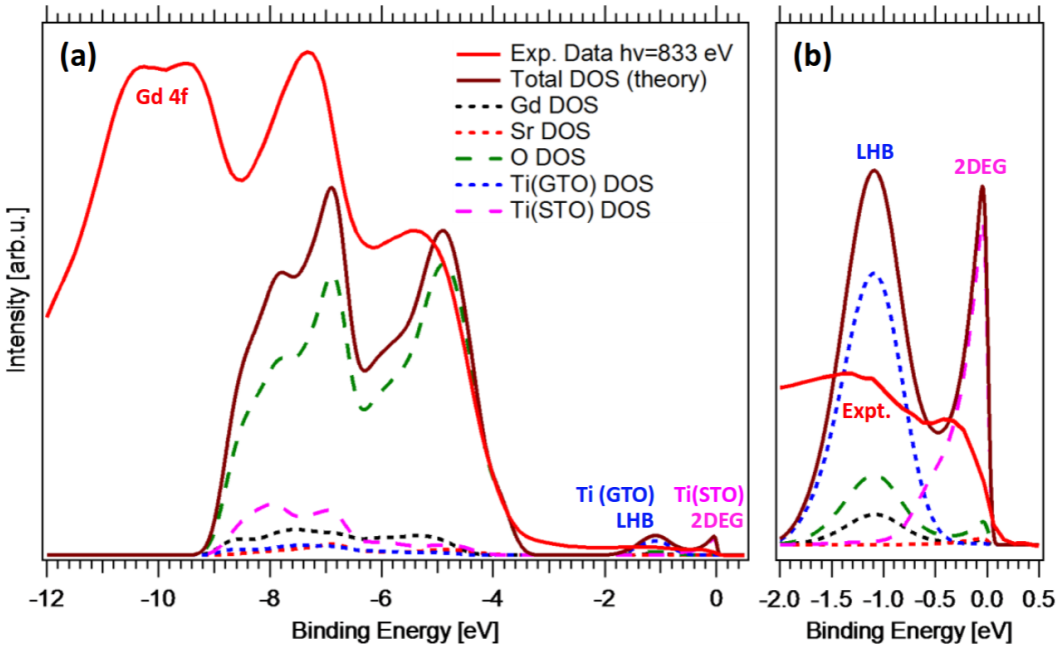

Figure 4.4: (a) Experimental valence-band spectra obtained in the group of Prof. C. Fadley from hard x-ray photoemission on an $(STO)_6/(GTO)_3$ superlattice grown in the group of Prof. S. Stemmer[135] compared to the calculated density of states (DOS) for the same structure. The atom-projected DOS is multiplied by the appropriate differential photoelectric cross section. The Gd $4f$ states were not included in the calculation. (b) Magnification of the region near the Fermi level.

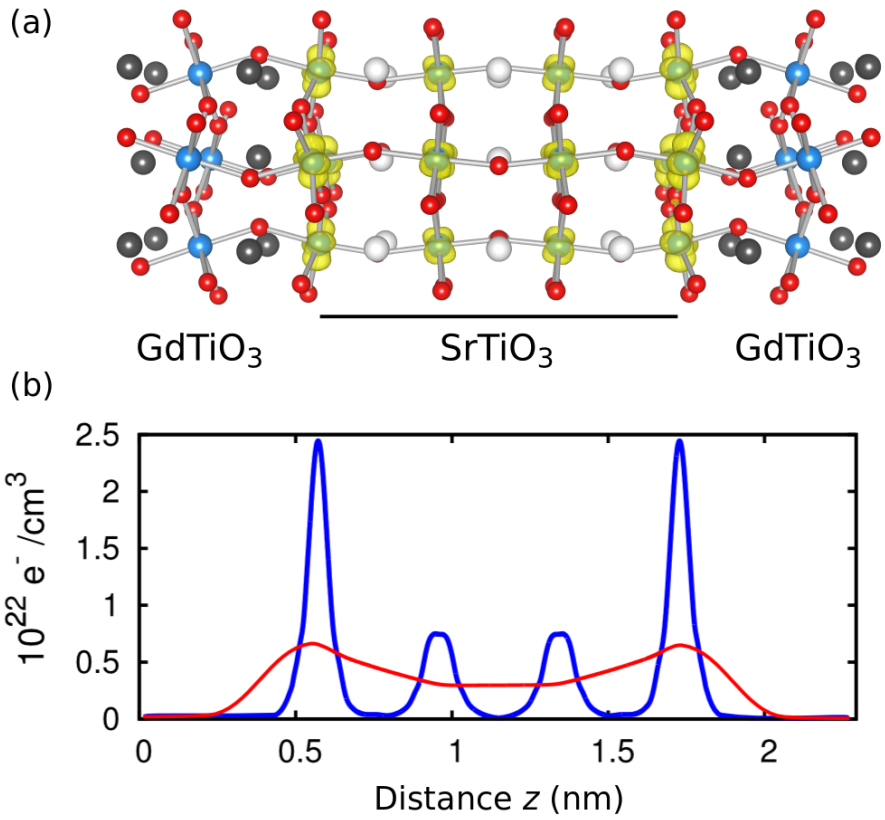

Figure 4.5: (a) Charge density of the occupied $SrTiO_3$ conduction bands and (b) in-plane averaged electron density (blue) and macroscopic average (red) for the $(GdTiO_3)_3/(SrTiO_3)_3$ superlattice.

As the thickness of the STO layer decreases, going from six to three layers, we see a downward shift of the lower-lying subbands; the overlap with the LHB is larger for the three-layer than the six-layer case [compare Figures 4.1(a) and (b)]. This is caused by a large spin splitting within the subbands, which increases with electron density. This large spin splitting corresponds to ferromagnetism in the STO layer, which has been observed experimentally for a GTO/$(STO)_3$/GTO heterostructure.[136]

4.2.2 Thin STO layers: Insulator

Decreasing the STO thickness to two or one unit cells, we see a drastic change in the electronic structure: $(STO)_2/(GTO)_3$ and $(STO)_1/(GTO)_3$ are no longer metallic, and display a band gap. In the case of $(STO)_2/(GTO)_3$ we observe localization and charge-ordering of the excess electrons on every other interface Ti atom, shown in Figure 4.6(a). These localized states form two bands, both with spin down, which lie within the LHB of the GTO, as can be seen in Figure 4.1(c). Each of these two bands is associated with a single TiO_2 interface plane. The lowest-energy unoccupied band originates from the central TiO_2 plane in the STO layer, and it exhibits a large dispersion as it is composed of Ti d_{xy} states, shown in Figure 4.6(b). The calculated band gap is 90 meV. The octahedra within the central TiO_2 plane are practically cubic as a consequence of the $(STO)_2/(GTO)_3$ superlattice geometry. To check that our results were not an artifact of this imposed high symmetry, we also performed calculations for $(STO)_2/(GTO)_4$. The

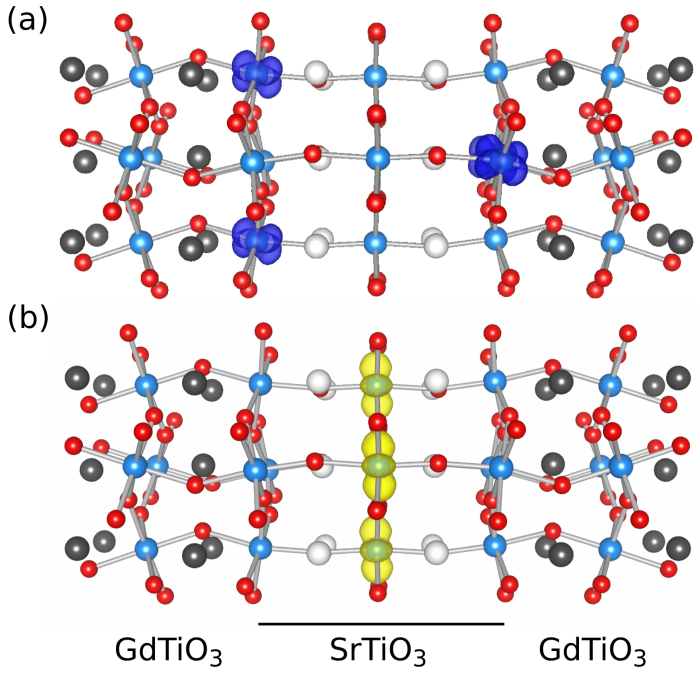

Figure 4.6: Γ-point charge density of (a) the two bands occupied by the excess electrons and (b) the conduction-band minimum, for the $(GdTiO_3)_3/(SrTiO_3)_2$ superlattice. Blue indicates spin down, and yellow no spin polarization.

same localization of electrons on interfacial Ti atoms was found, with the same band gap. This result is similar to a GGA+U study on STO/$LaAlO_3$ and STO/$NdGaO_3$ superlattices (both forming polar discontinuities with excess electrons in STO),[137] indicating that the thickness-dependent metal-to-insulator transition is a general feature of STO and not dependent on the details of the interface.

In the limit of a single STO layer we also obtain an insulating ground state, in agreement with experiment.[128] In contrast to the two-layer case, we now obtain a sizeable band gap of 0.82 eV, but the nature of the insulating state is the same: the TiO_2 layers

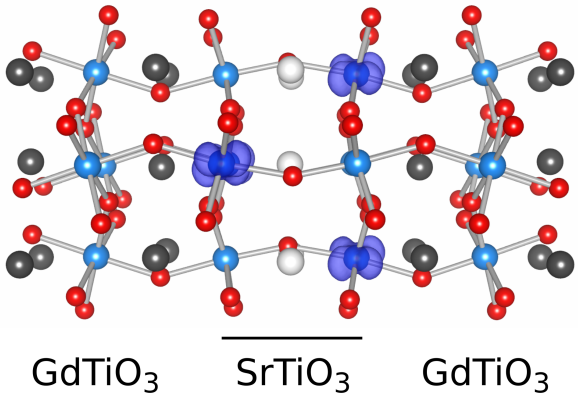

Figure 4.7: Γ-point charge density of the two bands occupied by the excess electrons in $SrTiO_3$ for the $(GdTiO_3)_3/(SrTiO_3)_1$ superlattice. Blue indicates spin down.

located between GdO and SrO layers display large rotations of the octahedra, the excess electrons are localized on every other Ti interface atom (Figure 4.7), and the electrons are distributed in two bands that overlap with the GTO LHB [Figure 4.1(d)]. These results differ from previous theoretical work on the n=1 case, using GGA+U and a model Hamiltonian based on GGA calculations, which resulted in a dimer Mott ground state with a 0.2 eV band gap.[129]

4.2.3 Understanding the transition

To understand why the system is no longer metallic for the n=2 and n=1 cases, we examine the atomic structure of the superlattices and the contributions to the total energy. First, we note that the GTO atomic structure and LHB energies remain largely intact as the thickness of the STO decreases from six to one layer—the Ti-O-Ti angles

differ by less than a degree, the Ti-Ti distances by less than 0.005 Å, and the bandwidth by less than 0.1 eV. For all investigated STO thicknesses, the relaxation in Ti-O-Ti bond angles required to accommodate the connectivity of the octahedra occurs predominately right at the interface—in the octahedra between planes of SrO and GdO. These interface octahedra are thus appreciably distorted, in contrast to the cubic structure of bulk STO, and these distortions are key to understanding why the system transitions from a metal to an insulator as the thickness decreases: The distortions break the degeneracy of the t_{2g} orbitals, allowing the minimization of the strong on-site electron-electron repulsion via the localization of the $3d$ electrons in single orbitals, each giving rise to a single band. This localization is what we observe at the interface for the one- and two-layer cases [as can be seen in Figures 4.1(c) and (d), which have two spin-down bands overlapping with the GTO LHB representing the localized interface electrons].

If the system can lower its electronic energy by localizing the excess electrons on every second interface Ti atom (alternating between Ti^{3+} and Ti^{4+}), why do we not observe this localization for *all* STO thicknesses? The answer is that there is a structural energy penalty associated with the localization; the TiO_6 octahedra have to distort. In addition to tilts and rotations, the Ti-O bond lengths also have to change; in the interface layer the Ti^{3+} atoms have longer Ti-O bonds than the Ti^{4+} atoms. For $n = 1$ ($n = 2$), the average Ti-O bond length is 2.05 Å (2.04 Å) for Ti^{3+} and 1.98 Å (1.98 Å) for Ti^{4+}. These changes in bond lengths cost energy, and therefore localization becomes favorable only

if the energy gain due to minimization of electron-electron repulsion is sufficiently large. The amount of energy gain is proportional to the magnitude of the electron density associated with a specific band. This density will be high in the case of thin STO layers, since then the number of STO conduction-band states is low and they are filled to high energies.

To quantify this argument, we inspect the $n = 2$ case. Here, in contrast to all the other STO thicknesses investigated, we can obtain both a metallic (delocalized) and insulating (localized) solution. The metallic solution has average Ti-O bond lengths in the interfacial TiO_2 layer of 2.00 Å, the same for all Ti sites, and a total energy 0.26 eV [per $(STO)_2(GTO)_3$ supercell] higher than the insulating solution. To estimate the structural energy penalty associated with localization, we remove the Ti $3d$ electrons from the system (i.e., we remove six electrons from the supercell, meaning that there are no excess electrons in STO and no LHB in GTO), and compare the energy of the metallic structure to that of the insulating structure; the former is 1.15 eV *lower* in energy. Since the *total* energy of the metallic phase is 0.26 eV higher than the insulating phase, this means that the electronic energy gained by going from a metallic to an insulating state is 0.26–(–1.15)=1.41 eV. Since the structural energy penalty is associated mainly with distortions in the interfacial layers, we expect our estimate of 1.15 eV to apply also to cases with thicker STO layers ($n > 2$); however, the amount of electronic energy gain decreases in thicker layers due to the fact that the number of STO conduction-band

states increases. For $n > 2$ electrons are spread over a larger number of bands, and the electronic energy gained by localization is insufficient to overcome the energy cost of the structural rearrangement.

4.3 Electron localization in *bulk* STO

Inspired by the intriguing result of electron localization for very thin STO layers in the GTO/STO/GTO heterostructures, we next show that STO this can also occur when *bulk* STO is doped at very high levels. Rather than behaving as a heavily doped semiconductor, a charge-ordered Mott insulating state emerges when 1/2 electron per Ti atom is added, with an occupied lower Hubbard band (LHB) separated by an energy gap from an unoccupied upper Hubbard band (UHB), derived from the Ti 3*d* states. This Mott insulating state is characterized by a large distortion of the crystal structure, with Ti-O-Ti angles of 165°, compared to 180° in the perfect cubic phase.

We first consider STO in a unit cell of 20 atoms (four $SrTiO_3$ formula units), to which we add one or two electrons and allow the volume and all the atomic positions to relax. A 6×6×2 special k-point mesh for integrations over the Brillouin zone and an energy cutoff of 500 eV for the plane-wave basis set were used. Figure 4.8(a) shows the relaxed atomic structure and the corresponding conduction-band structure of a neutral 20-atom cell of STO. The crystal structure is very close to cubic, with lattice parameters

of 3.903 Å (a, b) and 7.807 Å (c). Ti-O-Ti angles in this structure should be 180° (our choice of k-point mesh breaks the cubic symmetry and leads to inaccuracies on the order of 0.5°). Due to the octahedral crystal field, the $3d$ orbitals of Ti are split into lower-energy triply degenerate states with t_{2g} symmetry, and higher-energy doubly degenerate states with e_g symmetry. The conduction band derived from the t_{2g} orbitals is triply degenerate at the Γ point. Adding electrons to STO leads to partial occupation of the t_{2g}-derived bands, and within band theory, a metallic behavior is expected.

Upon adding one electron to the 20-atom cell, corresponding to an excess electron density of 1/4 per Ti atom, and allowing the crystal structure to relax we find that the system is metallic and remains in an almost perfectly cubic structure. The resulting band structure and the charge density corresponding to the partially filled conduction bands are shown in Figure 4.8(b). The lattice parameters increase by 1.3% (a, b) and 1.2% (c) compared to undoped STO. The change in lattice parameters upon electron doping is in line with experimental results.[138] An additional feature that arises as a result of doping STO with 1/4 per Ti atom is strong exchange splitting within the conduction band.

Attempts to localize the extra electron on a particular Ti atom in the 20-atom cell by slightly displacing the surrounding O atoms to accommodate the extra charge were unsuccessful. Calculations were also done for a 135-atom supercell, again finding that

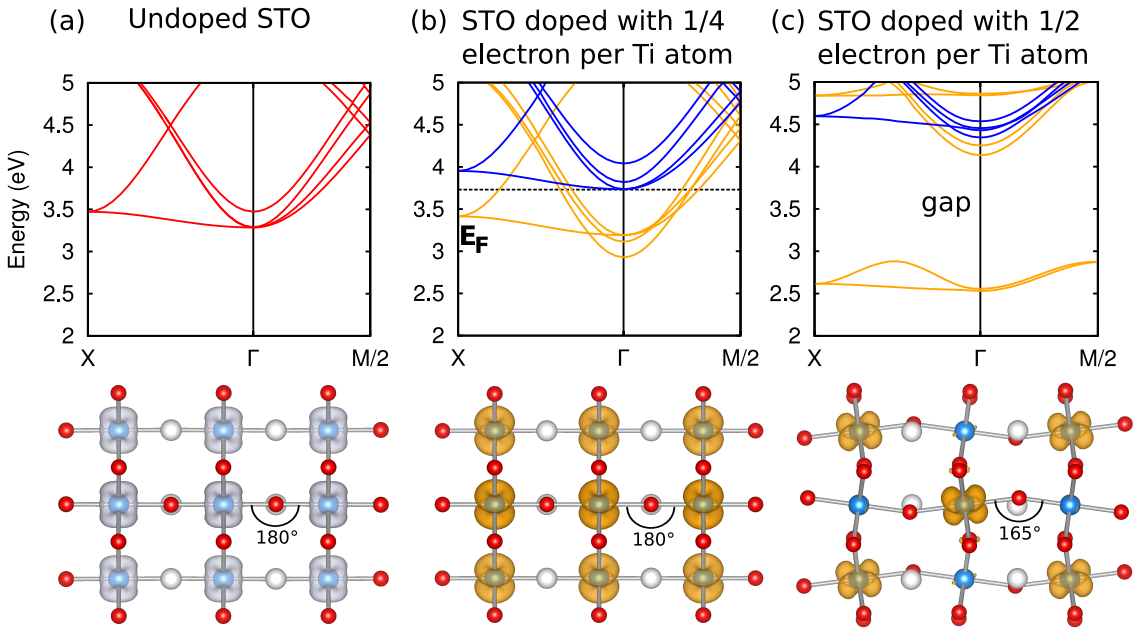

Figure 4.8: Evolution of electronic and atomic structure of STO as electrons are added. The conduction bands are plotted along the Γ-X and Γ-M/2 directions in the Brillouin zone (BZ) of the 5-atom cubic perovskite unit cell, which correspond to Γ-M and Γ-X in the BZ of the 20-atom cell. Red lines correspond to bands that are non-spin-polarized, orange to spin-up, and blue to spin-down bands. The top of the valence band is set as the reference. For the doped cells, the charge density of the occupied conduction-band states is shown (in orange) superimposed on the crystal structure, and for the undoped cells the charge density of the (unoccupied) lowest-lying conduction-band states at the Γ-point (in grey) is shown. In all cases the isosurface is set to 10% of the maximum. Undoped STO is shown in (a), STO doped with 1/4 electrons per Ti in (b), and STO doped with 1/2 electrons per Ti in (c).

an excess electron prefers to stay delocalized, with a charge distribution equally shared by all the Ti atoms.

For a doping level of 1/2 electron per Ti (i.e., adding two electrons to the 20-atom cell), the structure displays $GdFeO_3$-type distortions and a 1.26 eV gap opens within the t_{2g} derived bands, as shown in Figure 4.8(c). The calculated density of states (not

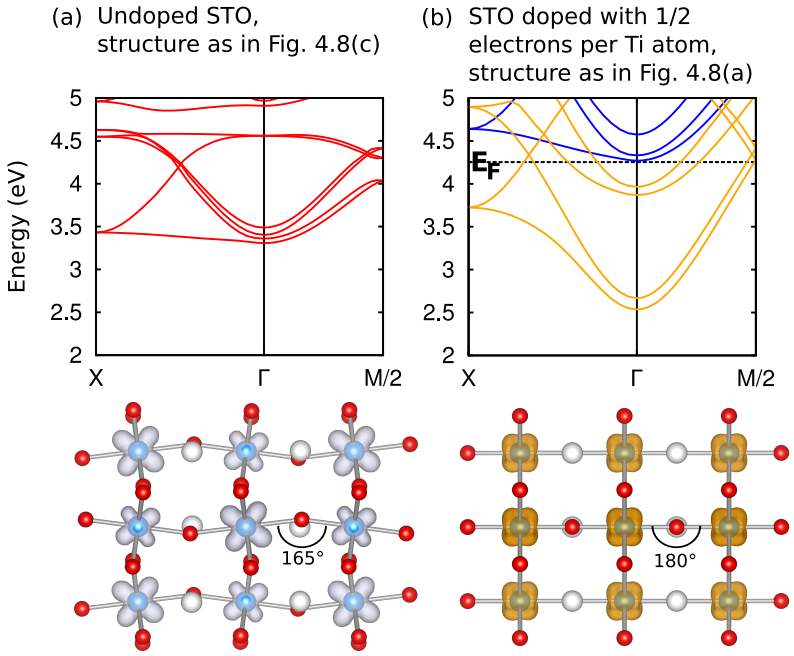

Figure 4.9: Continuation of Figure 4.8. In (a), the crystal structure is the same as in Figure 4.8(c), but the excess electrons are removed. In (b) the crystal structure is the same as in Figure 4.8(a), but doped with 1/2 electrons per Ti.

shown) confirms this result. The Ti-O-Ti angles decrease to 165° and 163°, and the lattice parameters increase by 2.6% (a, b) and 3.7% (c) compared to undoped STO. Based on the structural distortions we would expect a decrease in the lattice parameters; the observed increase is attributed to the effect of electron addition.[139] The distortions break the cubic symmetry seen by the Ti atoms, leading to a splitting of degenerate Ti $3d$ t_{2g} states, with a corresponding change in the orbital character of the bands. This is illustrated for the lowest-lying conduction band at the Γ point for the undoped cubic and distorted cases in Figurs 4.8(a) and 4.9(a). It therefore becomes possible to

split off a band derived from a single occupied orbital, which is what we observe upon electron addition: a LHB splits off, with each band derived from a single orbital (d_{xz} and d_{yz}) localized on a single Ti atom. Exchange splitting is also required to form the LHB, as it splits off the corresponding spin-down bands. We thus see the formation of a charge-ordered insulating ground state, with the added electrons residing on every other Ti atom in a three-dimensional checkerboard arrangement. In Figure 4.8(c) the charge density of the added electrons is plotted. The insulating state exhibits a ferromagnetic order with the antiferromagnetic arrangement higher in energy by 5 meV per Ti atom.

We speculate that this Mott insulating phase would be stable with respect to small deviations in the doping level, since phase separation is likely to occur. For a doping level below 1/2 electrons per Ti, a small fraction of the system would be undoped STO, also insulating. For doping levels above 1/2 electrons per Ti, a small fraction would be STO doped with 1 electron per Ti, which is insulating, with a distorted crystal structure (same situation as in, e.g., GTO). Unfortunately, explicit calculations investigating this behavior would require much larger supercells than computationally tractable.

In order to separate the effects of lattice distortions and electron-electron interactions, it is instructive to consider two test cases: (1) a distorted STO structure with the same atomic positions as in Figure 4.8(c) but without the extra electrons; and (2) undistorted STO with the same structure as in Figure 4.8(a) but with doping of 1/2 electron per Ti atom. The band structure for the distorted but undoped case is shown in Figure 4.9(a).

Despite the large structural distortion, the conduction bands look remarkably similar to those in Figure 4.8(a): degeneracies are split and avoided crossings occur, but no gap is observed.

The second case, where two electrons are added to the undistorted structure without allowing atomic relaxation, leads to a metallic state, as shown in Figure 4.9(e). The conduction bands are partially occupied, leading to a metallic ground state, again with strong exchange splitting, but with no evidence of gap formation. These results provide powerful evidence that structural distortions are key to achieving the insulating state. In the absence of such distortions [case (2), Figure 4.9(e)] the system remains metallic, even for the 1/2-electron-per-Ti case. Electron-electron interactions play a strong role as well, of course, evidenced by the significant differences in band structure between Figure 4.8(c) and Figure 4.9(a): structural distortions alone do not open up a gap, and electron localization is required to trigger gap formation. We conclude that *both* structural distortions and electron-electron interactions are *necessary* to trigger a metal-insulator transition, but neither is *sufficient* by itself.

4.4 Localization vs delocalization in bulk STO

In the previous Section we saw that bulk STO can host a charge-ordered phase of localized electrons when doped with 1/2 electron per Ti. Next, we construct a bulk

model for understanding the physical mechanisms involved in the balance of localization versus delocalization. In Section 4.2.3 the localized (insulating) configuration was shown to be 0.26 eV lower in energy than the delocalized (metallic) configuration for the $n = 2$ heterostructure. Similarly, for the bulk model we will calculate the increase in total energy upon adding electrons to STO, in either a localized or a delocalized configuration. By varying the added electron density q (corresponding to the excess number of electrons per Ti atom in STO in a heterostrucutre with layer thickness n), and comparing the energy of the localized and delocalized configurations, we can investigate when the metal-to-insulator transition occurs in the absence of the interface with GTO.

To find the energy of the delocalized configuration, $E_{\mathrm{deloc}}(n)$, for a given layer thickness n, we add $q = 1/(n+1)$ electrons (the number of excess electrons per STO Ti atom for a layer thickness n; for $n = 1$ there are *two* TiO_2 layers in the STO region) to a 5-atom unit cell of STO, and calculate the total energy ($E^q_{5,\mathrm{tot}}$). We reference this energy to the total energy of the neutral 5-atom cell ($E^0_{5,\mathrm{tot}}$) plus $q = 1/(n+1)$ electrons at the conduction-band minimum (CBM) of the neutral cell (E_{CBM}). Since we want the calculated energy to apply to the heterostructure supercells, in which two electrons are added to the STO layer, we multiply the resulting energy difference by $2(n+1)$:

$$E_{\mathrm{deloc}}(n) = [E^q_{5,\mathrm{tot}} - (E^0_{5,\mathrm{tot}} + q \times E_{\mathrm{CBM}})] \times 2(n+1). \tag{4.1}$$

The result is shown as the red curve in Figure 4.10.

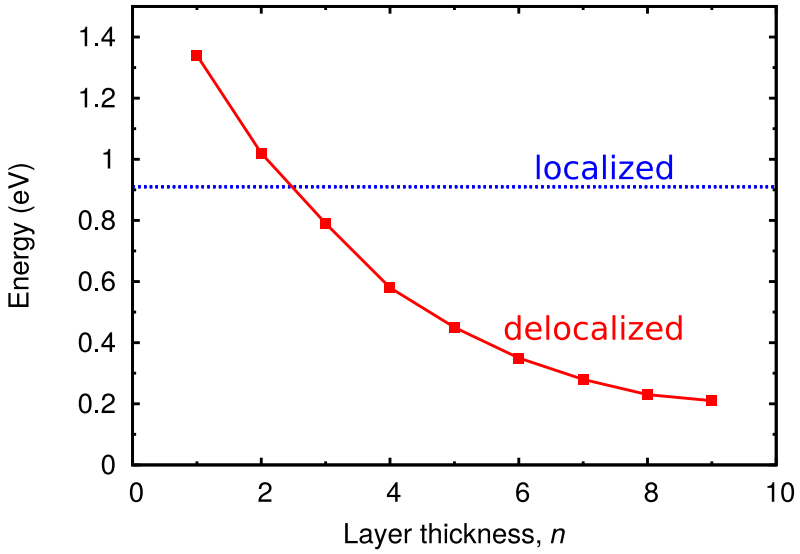

Figure 4.10: Energy of a bulk model for delocalized (red) and localized (blue) configurations of a system with two excess electrons in an STO layer of thickness n. The system mimics the situation of the GTO/$(STO)_n$/GTO heterostructure with two excess electrons added per $\sqrt{2} \times \sqrt{2}$ interface area. The energies are referenced to the energy of an undistorted bulk STO crystal in which the added electrons would all be placed at the CBM. Localization is favored for systems with layer thickness $n < 3$, just like in the full heterostructures.

To find the energy for the localized configuration, we need to work with a unit cell of STO large enough to accommodate charge ordering and distortions. A 20-atom unit cell of STO (i.e., a $\sqrt{2} \times \sqrt{2} \times 2$ enlargement of the 5-atom unit cell) allows for such internal structural relaxations; note this is similar to crystal structure of GTO. Upon addition of two electrons to this 20-atom cell (1/2 electron per Ti atom), the material turns into a Mott insulator. The electrons localize on every other Ti atom, and the structure displays $GdFeO_3$-type distortions.[140] The energy of this structure ($E^2_{20,\mathrm{tot}}$) is again referenced to the total energy of four neutral 5-atom $E^0_{5,\mathrm{tot}}$ cells plus 2 electrons at the CBM of the neutral cell (E_{CBM}), yielding the energy of the localized configuration:

$$E_{\mathrm{loc}} = E^2_{20,\mathrm{tot}} - [4E^0_{5,\mathrm{tot}} + 2E_{\mathrm{CBM}}]. \tag{4.2}$$

This energy of the localized configuration would apply to any thickness of STO in the heterostructure, since the excess electrons always localize in the interfacial TiO_2 layers, and therefore the STO layers away from the interface do not contribute.

Since the reference energy is the same for E_{deloc} and E_{loc}, they can be plotted on the same energy scale, as shown in Figure 4.10. E_{deloc} decreases as the electron density decreases, corresponding to smaller filling of conduction-band states. In the limit of very thick STO layers (i.e., if the added electron density q per Ti atom approaches zero), E_{deloc} goes to zero. For very thin layers, the localized configuration is more favorable;

the crossover occurs between n=2 and n=3, which is the same thickness at which the crossover occurs in the actual heterostructures.

The bulk model thus captures the key features of the behavior of thin STO layers, indicating that the mechanism for electron localization at high electron densities is independent of the nature or details of the interface, but rather a consequence of the properties of bulk STO. Naturally, this model is a "first-order" approximation since it builds only on bulk quantities. As such, it should not be expected to equally accurately describe *all* sytems. In particular, interface-specific effects might be more important in some cases. From inspecting Figure 4.10, we see that if such effects shift the energies of localization/delocalization by a few 0.1 eV per $\sqrt{2}a \times \sqrt{2}a$ interface area the transition from the metallic to insulating phase with decreasing STO thickness could be shifted or even suppressed. Experimental observations for SmTO/STO/SmTO quantum wells have shown no evidence of a transition to an insulating phase, even at the smallest STO layer thicknesses.[10] Here, the distortions at the interface are measured to be smaller than in the GTO/STO/GTO case for one and two STO layers. It may therefore be possible that the SmTO interface changes the bulk properties of doped STO, turning it metallic.

4.5 Summary

We have used first-principles calculations to describe the mechanism behind the metal-to-insulator transition in GTO/STO/GTO heterostructures as the STO thickness decreases below three layers.[27] For the one- and two-layer thick STO cases, a charge-ordered ground state is found, where every other interface Ti atom is occupied with one $3d^1$ electron, in contrast to the delocalized ground state found for three or more STO layers. We find that this charge-ordered ground state is also stable in *bulk* STO, and use this result to construct a bulk model. This model shows that the localized ground state becomes favored at very high electron densities because localizing electrons in specific orbitals becomes more favorable than having to fill the conduction band up to very high energies—this in spite of the cost of the lattice distortions required to enable localization. The fact that a bulk model can reproduce the main features of the transition from metal to insulator indicates that the physical mechanisms do not depend on the specifics of the interface. This fundamental understanding of the transition is key to designing a "Mott field effect transistor" based on a GTO/STO/GTO heterostructure, where small changes in the excess electron concentration in the STO (via an applied voltage) could switch the structure between the metallic and insulating phases.

Chapter 5

The electronic structure of $GdTiO_3$ and the impact of small polarons

5.1 Introduction

In this chapter we will investigate the electronic structure of GTO in detail. This is motivated by the explicit calculations of GTO/STO/GTO heterojunctions in Chapter 4, where the value of the GTO gap determines on which side of the interface these excess electrons reside and the degree of electron confinement, thus being an important design parameter. As described in Chapter 1, the rare-earth titanates are Mott insulators (Ti electron configuration $3d^1$), in which the energy band gap (Mott-Hubbard gap) arises from strong intra-atomic Coulomb electron-electron interactions that split partially filled

d or f bands, separating an occupied lower Hubbard band (LHB) from an unoccupied upper Hubbard band (UHB).[19] The magnitude of the gap reflects both the strength of the intra-atomic interactions U and the bandwidth W, and is therefore a key descriptor of the material.

Past experimental efforts to determine the Mott-Hubbard gap of GTO were based on optical absorption obtained by Kramers-Kronig analysis of reflectivity data on bulk crystals[132] or thin films grown on $(LaAlO_3)_{0.3}(Sr_2AlTaO_6)_{0.7}$ (LSAT),[59] or on transmission spectroscopy of films grown on $SrLaGaO_4$.[133] These measurements revealed an onset of optical absorption at around 0.7 eV, which was interpreted to correspond to the Mott-Hubbard gap. More generally, optical conductivity spectra of rare-earth titanates typically display onsets in the range 0.2 to 0.7 eV,[3,59,132,141] which have been attributed to excitations across the Mott-Hubbard gap.

However, recent photoluminescence (PL) and PL excitation (PLE) measurements on GTO conducted by our experimental colleagues in a collaboration with the groups of Prof. Susanne Stemmer and Prof. Debdeep Jena, paint a very different picture. PL produces a strong signal around 1.8 eV (Figure 5.1).[142] To reconcile a GTO bandgap of 0.7 eV with the 1.8 eV PL observation, one possibility would be to assume that 0.7 eV is the indirect bandgap of GTO while 1.8 eV corresponds to the direct transition. However, given that the LHB and UHB arise from d orbitals that are very localized, band dispersions greater than 1 eV are highly unlikely. Another possibility is that the PL arises

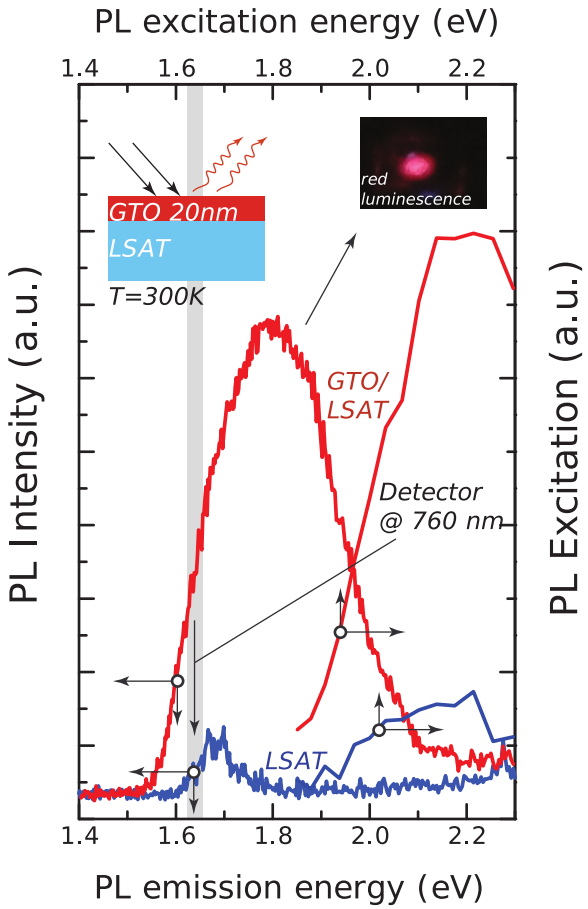

Figure 5.1: (Left+Bottom Axes) Room-temperature PL spectrum at 488 nm laser excitation of a 20-nm thin film of GTO grown on LSAT (red). Films were grown in the group of Prof. S. Stemmer, and measurements made in the group of Prof. D. Jena.[142] A peak at 1.8 eV is observed. (Inset) Visually observable red PL from the GTO sample when pumped with a 325 nm laser. (Right+Top Axes) Room-temperature PLE spectrum (red) of 20-nm thin film of GTO showing a bandedge like feature near ∼1.8 eV. The pump laser energy was varied, and the detector was tuned to measure the PL intensity at 760 nm. The control measurements of PL and PLE from the bare LSAT substrate are shown in blue.

not from band-to-band recombination, but from excitonic recombination, defect-to-band transitions, or defect-to-defect transitions.[143] However, all of these recombination mechanisms lead to PL emission either equal to or smaller than the band gap. Therefore, while the PL measurements alone do not allow identifying the precise recombination pathway, the observed PL emission from GTO puts a lower limit on its band gap and indicates this band gap to be greater than or equal to 1.8 eV.

This apparent discrepancy between photoluminesence and optical absorption begs for a reexamination of the electronic structure of GTO. Both the HSE and the GGA+U approach (see Chapter 2) produce a Mott-Hubbard gap around 2 eV, in close agreement with the PL result. The conclusion will be that the actual Mott-Hubbard gap of GTO is $\sim$ 2 eV, and we will attribute the absorption onset at 0.7 eV to self-trapped holes (small hole polarons).

5.2 Calculations on bulk GTO

Both the HSE and DFT+U methods were employed to simulate the 20-atom orthorhombic unit cell shown in Figure 5.2(a). The HSE calculations were done using a 500-eV energy cutoff for the expansion of plane waves and a $4 \times 4 \times 2$ Γ-centered k-point mesh for the Brillouin-zone integrations. The DFT+U calculations were performed by B. Himmetoglu, using $U = 4.38$ eV for Gd f orbitals and $U = 3.86$ eV for Ti d orbitals,

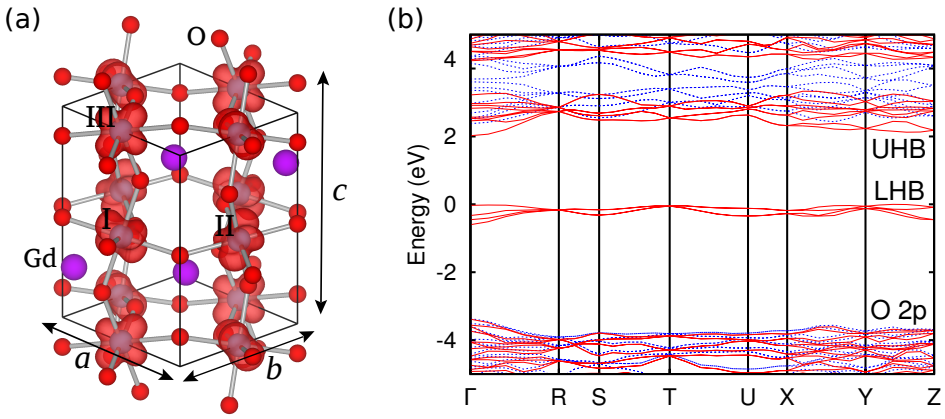

Figure 5.2: (a) Ball-and-stick model of the $GdFeO_3$ crystal structure of GTO. The Ti atoms used to define the Ti-O-Ti angles are indicated with I, II, and III. The lower Hubbard band charge density is shown in red (isosurface set to 10% of maximum). (b) Band structure of GTO calculated using HSE, with red (solid) lines corresponding to spin up states, and blue (dotted) lines to spin down states. The lower Hubbard band is filled, and the upper Hubbard band is empty—the Mott-Hubbard gap occurs between these bands. The zero of energy is set to the highest occupied eigenvalue.

computed self-consistently using a linear response method.[144] Ultra-soft pseudopotentials[145] were employed, as implemented in the Quantum ESPRESSO package.[146] A 60-Ry energy cutoff was used for the expansion of Kohn-Sham states, and a 720-Ry cutoff for the charge-density expansion, using a $6 \times 6 \times 6$ Monkhorst-Pack k-point mesh. For both methods, the Gd f electrons were included in the valence, and all calculations were done using spin polarization.

Both HSE and DFT+U find the ground state to be ferromagnetic, with the Ti $3d^1$ spins aligned, consistent with experiment.[130,131] The occupied f states are located in the low-energy part of the O $2p$ valence bands, and the unoccupied ones in the high-energy

part of the Ti $3d$ conduction bands, as can be seen in the density of states (Figure 5.3). The main difference between HSE [Figure 5.3(a)] and DFT+U [Figure 5.3(b)] calculations is the position of the O $2p$ bands, which are located about 2 eV higher in DFT+U. This is expected since DFT+U is not meant to correct the position of these bands.

Full structural relaxations yield lattice parameters and angles in close agreement with experimental values for bulk GTO, as shown in Table 5.1. The volume is underestimated by 0.7% in HSE, and overestimated by 5.0% in DFT+U, typical for the accuracy provided by these methods.

The band structure from the HSE calculation is shown in Figure 5.2(b), giving an indirect band gap of 2.02 eV. The top of the LHB occurs at a point along the Y-Z direction, while the bottom of the UHB occurs at Γ. The direct $\Gamma \rightarrow \Gamma$ band gap occurs at only slightly higher energy, namely 2.05 eV. The dispersion of the individual Hubbard bands is less than 0.7 eV, and the LHB is spin-up, corresponding to ferromagnetic alignment of the Ti $3d^1$ electrons. The LHB charge density is plotted in Figure 5.2(a), where orbital ordering of the LHB electrons can be seen. This is a consequence of the large crystal-field splitting of the Ti $3d$ t_{2g} states introduced by the $GdFeO_3$-type distortions, as described in previous work.[147,148] These localized electrons occupy bands derived primarily from d_{xz} and d_{yz} orbitals alternating on every second Ti atom. The band structures from DFT+U calculations (not shown) are very similar, yielding an indirect band gap of 2.21 eV, consistent with a recent study on GTO also using DFT+U.[149] The

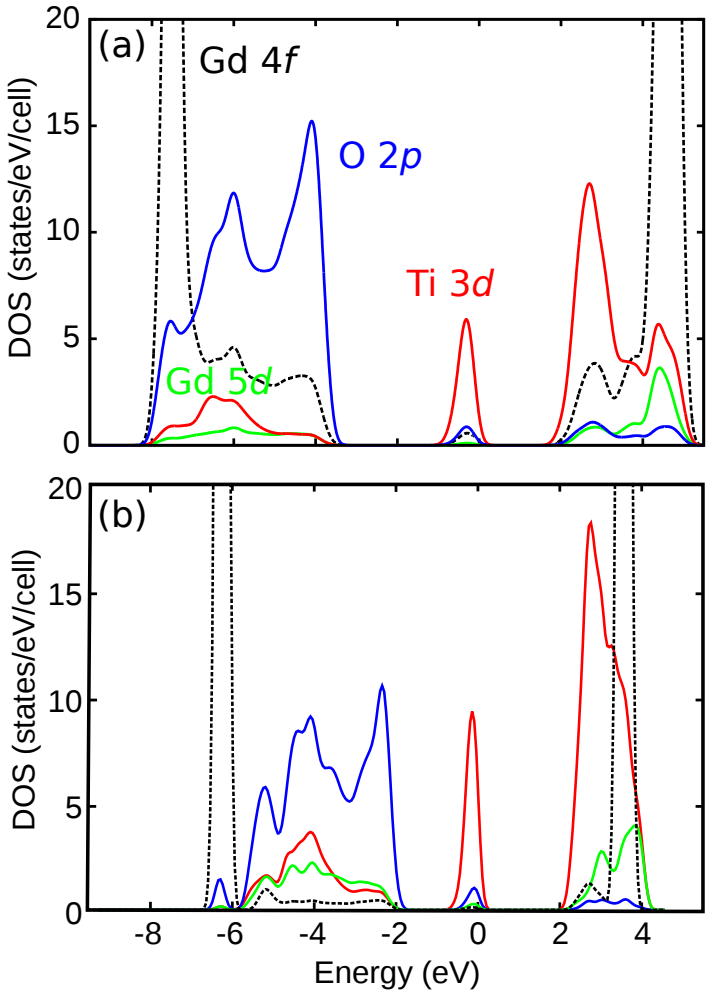

Figure 5.3: Atom-projected density of states for GTO calculated (a) using HSE and (b) using DFT+U (calculations performed by B. Himmetoglu in the group of Prof. C. G. Van de Walle). The zero of energy is set to the highest occupied eigenvalue.

Table 5.1: Equilibrium lattice parameters and Ti-O-Ti angles for bulk GTO. Angles referenced to Ti atoms as shown in Figure 5.2(a).

	HSE	DFT+U	Exp.[121]
a (Å)	5.351	5.464	5.393
b (Å)	5.725	5.820	5.691
c (Å)	7.627	7.781	7.664
Volume (Å^3)	233.65	247.43	235.22
Ti^I-O-Ti^{II} (°)	144.4	144.1	145.8
Ti^I-O-Ti^{III} (°)	140.4	144.2	144.1

slight overestimate compared to HSE can be largely attributed to the larger equilibrium volume in DFT+U.

Based on this band structure, we expect an onset of direct interband transitions at 2.05 eV. While electric dipole transitions within the d manifold, which gives rise to the LHB and UHB, are forbidden by symmetry, the hybridization with other orbitals, most significantly with O $2p$, leads to finite optical transition elements. The effect of hybridization of Ti d states with O p, Gd d and Gd f states is clearly visible in the atom-projected density of states shown in Figure 5.3. The presence of strong optical transitions is confirmed by our first-principles calculations of the absorption coefficient,

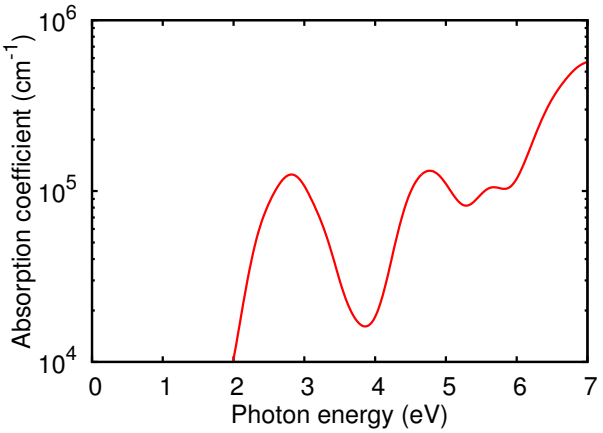

Figure 5.4: Total optical absorption for bulk GTO, calculated with HSE and averaged over the x, y, and z directions.

defined by

$$\alpha_i(\omega) = \frac{\sqrt{2}\omega}{c}\sqrt{|\epsilon_{ii}| - \mathrm{Re}(\epsilon_{ii}(\omega))}, \tag{5.1}$$

where $\epsilon_{ii'}$ is the dielectric tensor and ω the frequency. The dielectric tensor was computed with the HSE functional within the PAW formalism as described in Ref. 150. A 0.2 eV Gaussian smearing of the band occupancies was used, leading to a broadening of the absorption coefficient. The results shown in Figure 5.4 indicate strong optical transitions starting around 2.0 eV, with a peak at 2.8 eV. Recombination will occur at lower energies, closer to the band edge, since electrons excited to higher energies in the UHB will lower their energy nonradiatively before recombining with holes.

5.3 Small hole polarons in GTO

Both PL/PLE measurements and first-principles calculations are therefore consistent with a Mott-Hubbard gap of around 2 eV in GTO. This raises the question of the origin of absorption with an onset around 0.7 eV observed in reflectivity measurements.[59,132,133] For the similar material $YTiO_3$, this onset has been previously attributed to transitions between self-trapped holes and the LHB, in work led by B. Himmetoglu in the group of Prof. Van de Walle.[20] The presence of small hole polarons in GTO has been inferred from the *p*-type thermally activated transport.[132,151] Zhou and Goodenough[151] pointed out the discrepancy between the activation energies in DC transport and the band gap and proposed that the transport is caused by small polaron hopping. The formation of such polarons due to strong coupling with the lattice is well documented;[128,141,152] however, their role in optical conductivity has not been fully appreciated until now. Optical excitations of electrons from the LHB to the self-trapped hole state can then occur.

This section is devoted to the calculation of absorption spectra corresponding to the excitation of a small polaron either from a localized site to an adjacent site[153–155] or from a localized to a delocalized configuration.[156] In collaboration with co-workers at UCSB, we find an excellent match between the low-energy feature in the optical conductivity spectra (measured by D. G. Ouellette and S. J. Allen) of high-quality

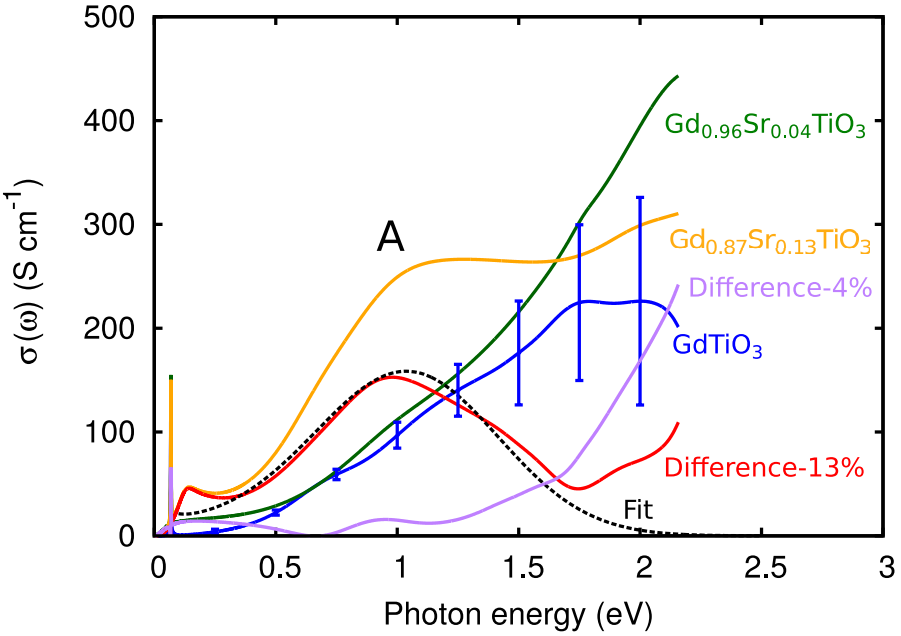

Figure 5.5: Real part of the optical conductivity of $Gd_{1-x}Sr_xTiO_3$ thin films at 10 K. Films were grown in the group of Prof. S. Stemmer, and measured in the group of Prof. S. J. Allen. The "Difference-13%" curve (red) represents the difference between the spectra of $Gd_{0.87}Sr_{0.13}TiO_3$ and of GTO, and the "Difference-4%" curve (purple) the difference between $Gd_{0.96}Sr_{0.04}TiO_3$ and GTO. The dashed line is the fit of the "Difference-13%" curve to the small polaron model [Eq. (5.2)].

.

epitaxial $Gd_{1-x}Sr_xTiO_3$ films grown by MBE (by P. Moetakef, T. Cain, and S. Stemmer), shown in Figure 5.5.[157] Here the Sr-alloying introduces small hole polarons; Sr is valence +2 and Gd +3.

To explain the behavior of feature A, we first consider the excitation of the small polaron out of its self-trapping potential well via a hopping process, with the structure subsequently relaxing by creating a lattice distortion at a neighboring site [Figure 5.6(a)].

In this process, the optical absorption is expected to peak near twice the polaron self-trapping energy, E_{ST} [defined in Figure 5.6(b)].[155] Considering the probability of hopping to an adjacent site within perturbative solutions to the Holstein model, the optical absorption peak is expected to be four times as large as the DC conductivity activation energy.[158–160] Therefore, we also expect the self-trapping energy to be twice as large as the activation energy.

Our collaborators D. G. Ouellette and S. J. Allen at UCSB compared the incoherent absorption below the Mott-Hubbard gap to an approximate expression for the optical conductivity of a small polaron:[153–155]

$$\sigma_1(\omega) = n_p \frac{\pi^{1/2} e^2}{m\omega} \frac{t}{\Delta} \exp\left[-\frac{(2E_{\mathrm{ST}} - \hbar\omega)^2}{\Delta^2}\right] \tag{5.2}$$

where n_p is the polaron density and $t = \frac{\hbar^2}{2ma^2}$ is the electronic bandwidth parameter with a being the lattice constant and m the effective mass. At low temperatures, $kT \ll \hbar\omega_0$, the width is determined by the zero-point phonon motion, $\Delta = (4E_{\mathrm{ST}}\hbar\omega_0)^{1/2}$, where ω_0 is the frequency of the relevant phonon mode. The factor t/Δ represents a transition probability and should be replaced by unity in the adiabatic limit, $t > \Delta$.[155]

To separate the polaron contribution from the Mott-Hubbard feature at higher energy, the optical conductivity of the undoped GTO film was subtracted from that of the $Gd_{0.87}Sr_{0.13}TiO_3$ film at 10 K and the difference was fitted to Eq. (5.2). The fit is shown as the dashed line in Figure 5.5. The resulting self-trapping energy is $E_{\mathrm{ST}} = 0.58$ eV,

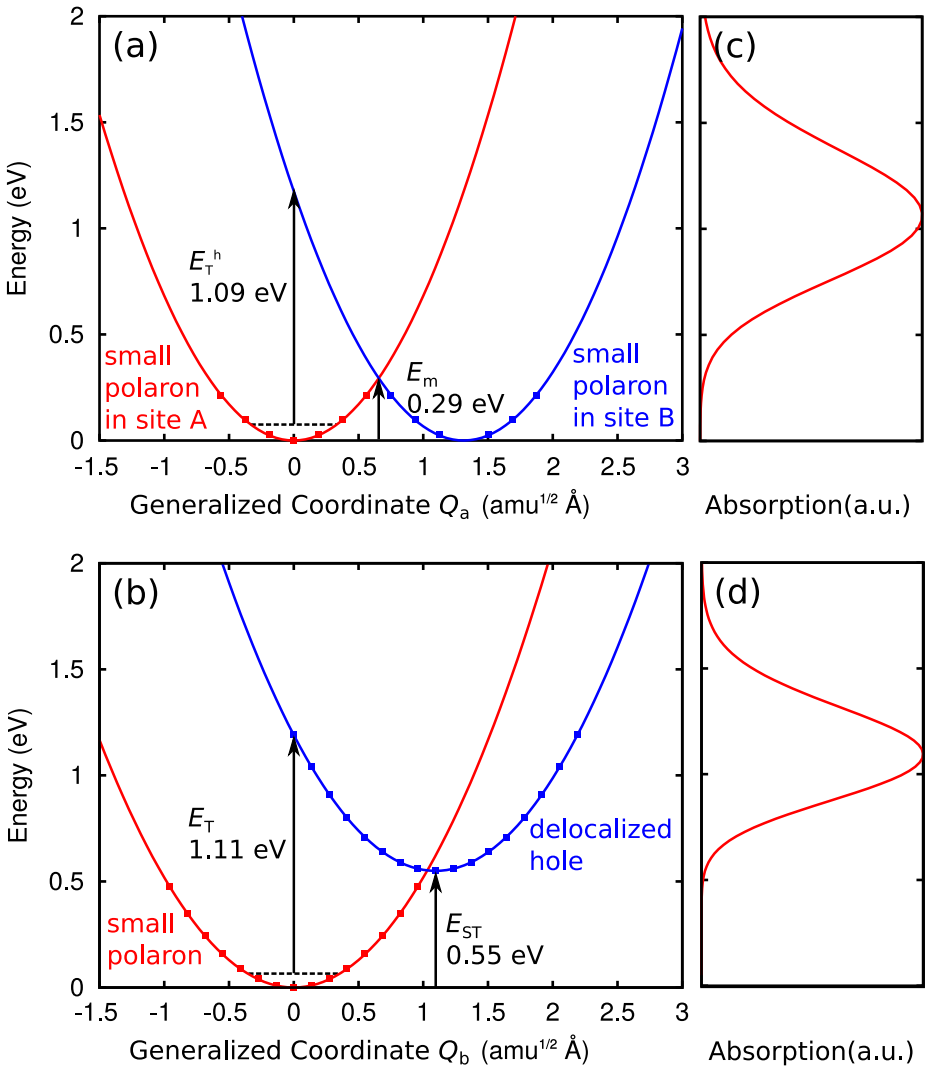

Figure 5.6: Calculated one-dimensional configuration-coordinate diagrams for (a) the excitation of a small hole polaron to a nearest-neighbor site and (b) the excitation of a small hole polaron to a delocalized-hole configuration. Symbols correspond to calculated values and the solid lines are parabolic fits. The dashed horizontal lines correspond to the vibronic ground state in the starting configurations. E_T^h and E_T are the transition energies of the two processes, E_{ST} is the small-polaron self-trapping energy, and E_m is the polaron migration barrier energy. Note that the atomic displacements are different for (a) and (b), giving different generalized coordinates Q_a and Q_b. In (c) and (d) the calculated broadening of each transition is plotted.

about twice as large as the 0.24 eV activation energy that has been reported for bulk samples.[151] The broadening factor, $\Delta = 0.51$ eV, corresponds to a phonon energy $\hbar\omega_0 = 110$ meV, which is larger than the highest-frequency optical phonon mode (67 meV) reported for GTO.[161] That there is some difference is expected, since Eq. (5.2) is an approximate expression involving multiple fitting parameters. The presence of Sr_{Gd} substitutional impurities will also lead to an increased mode energy, as will be discussed further below. Taking the polaron density as $n_p = x = 0.13$, we obtain a bandwidth, $t = 0.18$ eV and mass, $m = 1.4\ m_e$, where m_e is the free-electron mass.

To perform first-principles calculations for the small polarons, a single electron was removed from a 160-atom supercell, which is constructed based on a $2\times2\times2$ replication of the 20-atom GTO unit cell. The crystal symmetry was broken by slightly displacing the O atoms around a given Ti atom, followed by the relaxation of the atomic positions in the supercell. A 400 eV cutoff for the plane-wave expansion was used, and the integrations over the Brillouin zone were performed with a $(1/4, 1/4, 1/4)$ special k-point.

The atomic structure of a small hole polaron, as obtained from the first-principles calculations, is shown in Figure 5.7. We consider two types of excitation processes: (a) the hopping process described above, and (b) the excitation of a small hole polaron to a delocalized-hole configuration. The calculated configuration coordinate diagrams associated with these two mechanisms are shown in Figure 5.6. The generalized coordinate Q describes the displacement of the atoms with respect to the initial state ($Q = 0$)

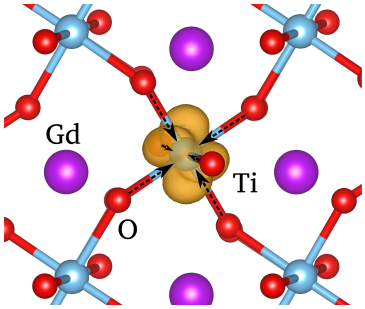

Figure 5.7: Atomic configuration and charge-density isosurface (10% of maximum value) for a small hole polaron in GTO. The Ti-O bonds surrounding the Ti atom where the polaron resides shrink relative to the bulk bond length, as indicated by the dashed arrows.

weighted by the mass of each atomic species:

$$Q^2 = \sum_{\alpha} m_{\alpha}(R_{\alpha} - R_{i;\alpha})^2 s \tag{5.3}$$

Here m_{α} are the atomic masses of the atoms, labeled with index α. The atomic positions of the intermediate configurations were obtained by interpolation between the initial and final configurations. A parabola was fitted to the data points.

Based on the configuration coordinate diagrams, the broadening of the transition energies due to lattice vibrations was calculated using the formalism developed by Huang and Rhys.[162] Each configuration corresponds to a harmonic oscillator, with quantized levels corresponding to different vibronic states. The vibrational problem is therefore approximated by a single effective phonon frequency. The calculated vibrational modes are 75 meV for the harmonic oscillators in transition (a), and 65 meV for those of

transition (b), which are both close to the highest-frequency optical phonon mode in bulk GTO (67 meV).[161]

As seen in the configuration coordinate diagram in Figure 5.6(b) we find a polaron self-trapping energy of 0.55 eV (E_{ST}), and in Figure 5.6(a) we find the energy barrier for polaron migration to be 0.29 eV (E_{m}). This is close to half of the polaron self-trapping energy, consistent with the Holstein model.[158] The calculated peak energy for the excitation of an electron from the lower Hubbard band to the polaron state in the gap is 1.12 eV (E_{T}), and for the excitation of the polaron out of its self-trapping potential well via a hopping process it is 1.09 eV ($E_{\mathrm{T}}^{\mathrm{h}}$). Both of these values are in good agreement with the observed 1 eV peak (Figure 5.5), and once again consistent with the Holstein model, being about twice as large as the polaron self-trapping energy.

The calculated absorption curves for the two mechanisms are shown in Figs. 5.6(c) and (d). Since the experiments were performed at 10 K, we only take transitions from the first vibronic state of the initial configuration into account. The onsets are at a slightly higher energy than in experiment. We attribute this to the presence of the $\mathrm{Sr_{Gd}}$ substitutional impurities in the samples, which is likely to lead to a broadening of the absorption peak that is not included in the calculations. This is consistent with the phonon mode found by fitting the experimental data to Eq. (5.2) being larger (110 meV) than the calculated modes [75 meV for transition (a), and 65 meV for transition (b)].

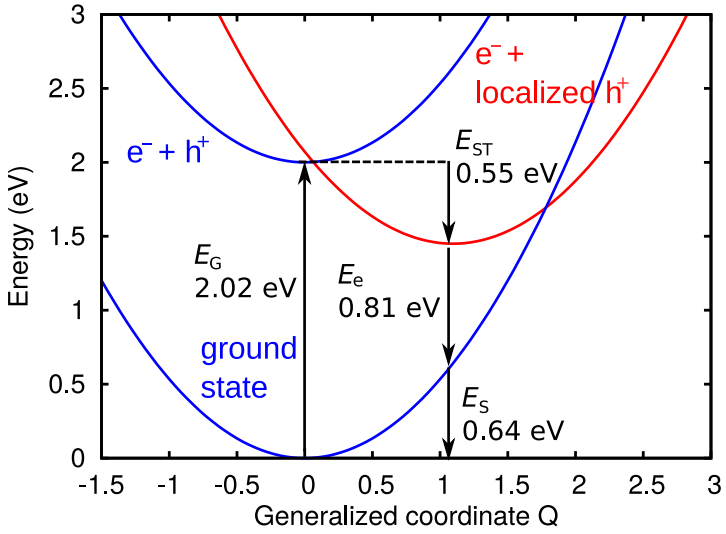

Figure 5.8: (Color online) Configuration coordinate diagram for the recombination of an electron with a localized hole (small polaron). E_G is the band-gap energy, E_{ST} the polaron self-trapping energy, E_e the optical emission energy, and E_S is the lattice energy cost (strain energy).

We also need to consider the possible role of small hole polarons in luminescence. There are two conceivable mechanisms that could be probed using PL/PLE. First, excitation of an electron from the LHB to the self-trapped hole state could occur, but after this excitation the small-polaron state is gone—all that remains is a local distortion of the crystal structure, which will decay via phonon emission. Second, an electron excited to the UHB could recombine with a small-hole-polaron state. For a polaron in bulk GTO we calculate the peak of this emission to occur around 0.8 eV, as illustrated in the configuration coordinate diagram of Figure 5.8. A transition at this energy is actually more likely to be nonradiative,[163] and indeed, PL measurements around 0.7 eV do not show any signal in this energy range.[142]

5.4 Summary

First-principles results for GTO indicate that the Mott-Hubbard gap is significantly larger than the previously accepted value of 0.7 eV. The calculations predict a gap of 2.0 eV, in good agreement with the observed 1.8 eV PL peak, which constitutes a lower limit to the band gap. The previous 0.7 eV value came from the onset of optical absorption. Instead, we propose that this optical excitation is caused by small hole polarons. The self-trapping energy is found to be 0.6 eV, both from optical conductivity measurements (performed by experimental collaborators at UCSB) as well as from first-principles calculations. Calculations for excitation of a small hole polaron to a delocalized-hole configuration and for excitation of the small polaron out of its self-trapping potential well via a hopping process both yield an optical excitation peak at 1.1 eV, in good agreement with the experimental peak at 1 eV. We conclude that this feature in the optical conductivity spectra is caused by small hole polarons, and not by excitations across the Mott-Hubbard gap.

Chapter 6

Point defects and impurities as a source of small hole polarons in $GdTiO_3$

6.1 Introduction

In this Chapter our goal is to investigate the origin of the small polarons observed in GTO, as discussed in Section 5.3. We present a comprehensive study of native point defects (vacancies, interstitials, and antisites), and investigate the likelihood of various impurities being incorporated. In general, such defects introduce states that affect electronic and optical properties by acting as carrier traps or recombination centers.

Surprisingly, we find that in GTO *all* the native defects and the considered impurities (except H_i) act as a source of small hole polarons, including oxygen vacancies. We identify which point defects are most likely to form and how they impact electronic and optical properties. We also evaluate how the resulting defect transition levels may impact devices based on the tunneling of the 2DEG electrons at the STO/GTO interface through the GTO.

Electronic and structural properties of an array of native defects are described in Section. 6.4. In addition to the native defects, in Section 6.5 we investigate C, Sr, and H impurities, which are likely to be present during growth of GTO on STO. Section 6.6, finally, discusses the impact of defects on conductivity, optical properties, and devices.

6.2 Formation energy and transition levels

Once again our approach is DFT with a hybrid functional, which provides reliable values for defect formation energies and transition levels in semiconductors and insulators.[164–168] As for the study of bulk polarons in Section 5.3, defect calculations were performed in a 160-atom $2 \times 2 \times 2$ supercell. wave functions were expanded in a plane-wave basis set with a 400 eV energy cutoff, and the $(1/4, 1/4, 1/4)$ special k-point was used for integrations over the Brillouin zone. Atomic structure was considered con-

verged when Hellman-Feynman forces were less than 0.01 eV/Å. Symmetry breaking was explicitly allowed by choosing low-symmetry initial structural configurations.

The formation energy of a defect D in a charge state q is defined as:[49]

$$E^f(D^q) = E_{\text{tot}}(D^q) - E_{\text{tot}} - \sum_i n_i \mu_i + q\epsilon_F + \Delta^q \,, \tag{6.1}$$

where $E_{\text{tot}}(D^q)$ is the total energy of a supercell containing a defect D in charge state q, and E_{tot} is the total energy of the perfect GTO supercell. n_i is the number of atoms of species i (i = Gd, Ti, O, Sr, H, or C) added to ($n_i > 0$) and/or removed from ($n_i < 0$) the perfect crystal to form the defect, and μ_i are the atomic chemical potentials. ϵ_F is the Fermi level referenced to the valence band maximum (for GTO, the top of the LHB). Δ^q is a correction term to align the electrostatic potential in the perfect bulk and defect supercells and to account for finite-cell size effects on the total energies of charged defects, using the approach of Freysoldt *et al.*[169,170]

The charge-state transition level (q/q') is defined as the Fermi-level position below which the defect is most stable in charge state q and above which the defect is most stable in charge state q'. It can be derived from the formation energies:

$$(q/q') = \frac{E^f(D^q; \epsilon_F = 0) - E^f(D^{q'}; \epsilon_F = 0)}{(q' - q)} \,, \tag{6.2}$$

where $E_f(D^q; \epsilon_F = 0)$ is the defect formation energy for charge state q when ϵ_F is at the top of the LHB. The position of the transition level in the band gap is independent of the choice of chemical potentials.

6.3 Atomic chemical potentials

The defect formation energies depend on the atomic chemical potentials μ_i, which are taken with respect to the total energy per atom of the standard phase of the species i. I.e., μ_{Gd} is referenced to the total energy per atom of Gd metal (hcp), and μ_{H} to half of the total energy of an isolated H_2 molecule. The chemical potentials are variables, but restricted by the formation of limiting phases containing the relevant species. The chemical potentials must satisfy the stability condition of GTO:

$$\mu_{\mathrm{Gd}} + \mu_{\mathrm{Ti}} + 3\mu_{\mathrm{O}} = \Delta H_f(\mathrm{GTO})\,, \tag{6.3}$$

with $\mu_{\mathrm{Gd}} \leq 0$, $\mu_{\mathrm{Ti}} \leq 0$, and $\mu_{\mathrm{O}} \leq 0$, and $\Delta H_f(\mathrm{GTO})$ the formation enthalpy.

The chemical potentials are further restricted by the formation of TiO_2, Gd_2O_3, and $Gd_2Ti_2O_7$ phases:

$$\mu_{\mathrm{Ti}} + 2\mu_{\mathrm{O}} \leq \Delta H_f(\mathrm{TiO_2})\,, \tag{6.4}$$

$$2\mu_{\mathrm{Gd}} + 3\mu_{\mathrm{O}} \leq \Delta H_f(\mathrm{Gd_2O_3})\,, \text{and} \tag{6.5}$$

$$2\mu_{\mathrm{Gd}} + 2\mu_{\mathrm{Ti}} + 7\mu_{\mathrm{O}} \leq \Delta H_f(\mathrm{Gd_2Ti_2O_7})\,, \tag{6.6}$$

Calculated and experimental formation enthalpies are listed in Table 6.1. By using Eqs. (6.3)–(6.6) we can define a region in the μ_{O} vs. μ_{Ti} plane in which GTO is stable, as shown in Figure 6.1.

Table 6.1: Calculated and experimental formation enthalpies.

Material	Present work (eV)	Experiment (eV)
GTO	-17.22	
TiO_2	-9.13	-9.74[171]
Gd_2O_3	-18.67	-18.8[172]
$Gd_2Ti_2O_7$	-38.05	-39.62[173]
H_2O	-2.68	-2.51[172]
CO_2	-3.89	-4.07[172]
SrO	-5.64	-6.12[171]
$SrTiO_3$	-16.05	-17.14[174]

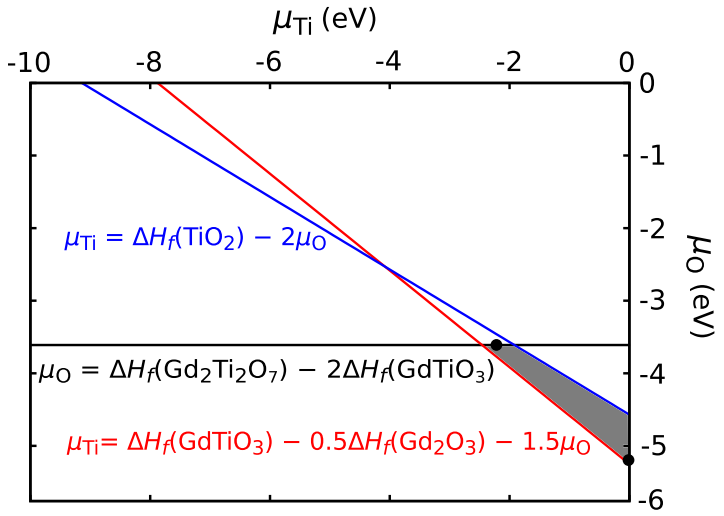

Figure 6.1: Allowed values of O and Ti chemical potentials (gray shaded region) defining the stability of GTO. The chemical potentials μ_{Ti}, μ_O, and μ_{Gd} are limited by the formation of secondary phases TiO_2 (rutile), Gd_2O_3, and $Gd_2Ti_2O_7$. The filled black circles correspond to $\mu_O = -3.61$ eV and $\mu_O = -5.25$ eV, spanning the range of possible values of μ_O.

For calculating the formation energies we focus on two extreme cases, indicated with filled black circles in Figure 6.1. The first is defined by $Gd_2Ti_2O_7$ (pyrochlore) as the limiting phase, with $\mu_O = -3.61$ eV; since this sets an upper limit on μ_O we refer to this as "oxygen-rich", though it should be noted that the value of μ_O is quite low. While this does not strictly specify the value of μ_{Ti}, the stability region is sufficiently narrow that μ_{Ti} can vary by only 0.55 eV, and we chose a value at the center of this region: $\mu_{Ti} = -2.20$ eV. "Oxygen-poor" conditions correspond to Gd_2O_3 as the limiting phase, with $\mu_O = -5.25$ eV and $\mu_{Ti} = 0$ eV.

When considering impurity atoms, we also need to take into account limiting phases for H, C, and Sr; these are also included in Table 6.1. μ_H is subject to the constraint $2\mu_H + \mu_O \leq \Delta H_f(H_2O)$, but due to the low values of μ_O needed to stabilize GTO, H_2O turns out not to be a limiting phase. Similarly for C, CO_2 is not a limiting phase. For Sr, SrO and $SrTiO_3$ are possible limiting phases. We find that for our choice of oxygen-rich conditions, $SrTiO_3$ limits μ_{Sr} to -3.02 eV, and for oxygen-poor conditions, SrO limits μ_{Sr} to -0.39 eV.

6.4 Results: Native defects

The formation energies of all native defects considered in our study are shown in Figure 6.2. The intrinsic defects include vacancies (V_{Gd}, V_{Ti}, and V_O), antisites (Ti_{Gd}

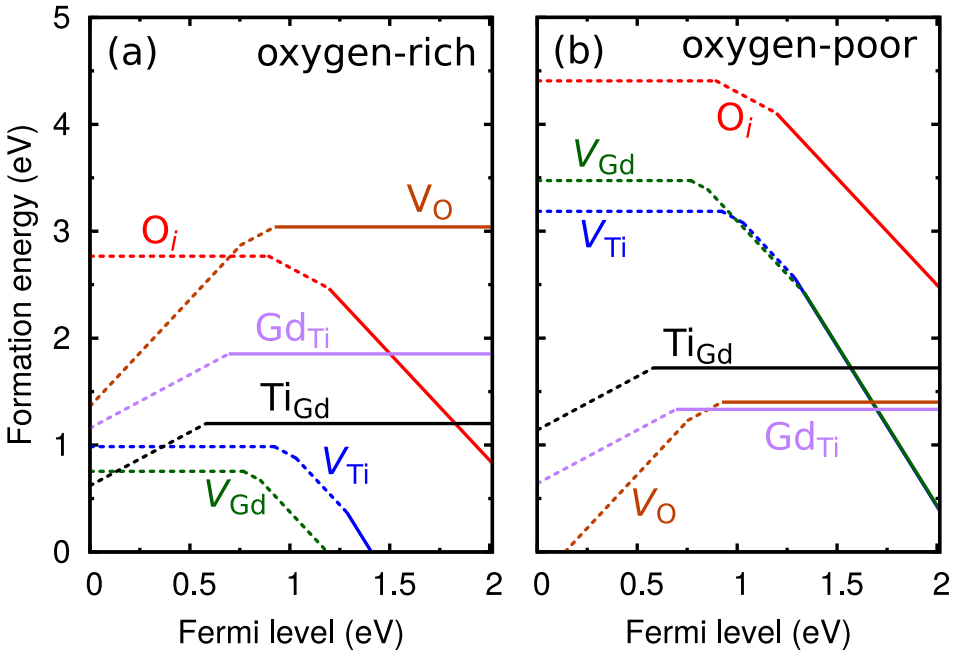

Figure 6.2: (Color online) Formation energies as a function of Fermi level for native defects in GTO under (a) oxygen-rich and (b) oxygen-poor conditions. The slopes of the lines indicate the charge state of the defect, and the kinks in the lines correspond to the position of the charge-state transition levels in the gap [Eq. (6.2)]. The dotted lines indicate charge states corresponding to hole polarons bound to the defect center.

and Gd_{Ti}), oxygen interstitials (O_i), and cation interstitials (Ti_i and Gd_i). The cation interstitials are found to have high formation energies (due to the highly compact perovskite structure and their large atomic radius) and a discussion of their behavior is not included.

6.4.1 Polarons in bulk $GdTiO_3$

In Section 5.3 we discussed the presence of small hole polarons in bulk GTO. The Ti atoms are in a Ti^{3+} configuration, and removing an electron leads to a hole in the LHB, which localizes in the form of a small polaron, corresponding to a single Ti^{4+}. The Ti-O bonds surrounding this Ti^{4+} atom shrink relative to the bulk bond lengths. Such small polarons are stable in bulk GTO with a self-trapping energy of 0.55 eV; i.e., the localized state is 0.55 eV lower in energy than the delocalized state of the hole (at the top of the LHB). Within a defect model, this corresponds to a (+1/0) transition level at 0.55 eV above the VBM (top of the LHB).

6.4.2 Oxygen vacancies

As expected, the formation energy of V_O in GTO is low for oxygen-poor conditions [Figure 6.2(b)]. Oxygen is two-fold coordinated, and the removal of an oxygen atom leaves two Ti 3*d* "dangling bonds." These dangling bonds form an occupied bonding state resonant in the LHB (Figure 6.3) and an empty antibonding state resonant in the UHB. In the neutral charge state, the Ti-Ti distance is 3.69 Å (compared to 3.81Å in bulk GTO), and the bonding state is doubly occupied.

This atomic and electronic structure is similar to what is found for V_O in other perovskite oxides such as STO,[175] $SrZrO_3$,[176] or $LaAlO_3$.[177] Those other oxides are band

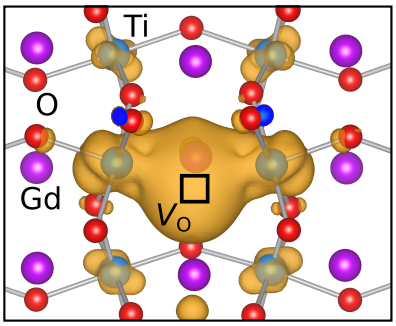

Figure 6.3: (Color online) Charge density for the Ti-Ti bonding state in an oxygen vacancy (V_O), with isosurface set to 10% of the maximum.

insulators, however, and the bonding state is located within the band gap of the oxide; +1 and +2 charge states can then be stabilized by taking electrons out of this state. In contrast, in GTO the bonding state overlaps with the LHB and hence removing electrons from this state corresponds to inducing holes in the LHB. These holes stabilize in the form of one or two small polarons localized on the Ti atoms neighboring the vacancy, while the Ti-Ti bonding state itself remains doubly occupied. The structure of these polarons is similar to that of bulk polarons,[157] and the structure of the "center" of the defect remains very similar to that of the neutral charge state.

The neutral charge state is therefore in principle the only "stable" charge state of the defect, within the traditional view of defects in semiconductors and insulators.[49] To indicate that the +1 and +2 charge states correspond to polarons bound to the neutral defect center, we show the corresponding formation energies in dotted lines in Figure 6.2. The (+2/+1) transition level occurs at 0.75 eV and (+1/0) at 0.92 eV. Since in the bulk

a hole polaron is stabilized by 0.55 eV compared to a free hole, as discussed in Sec. 6.4.1, the values indicate that the first polaron is bound to the defect center by 0.37 eV, and the second by 0.20 eV.

6.4.3 Cation vacancies

Gd and Ti both have valence 3 in GTO; removing either a Gd or Ti therefore leads to a deficiency of three electrons (in the neutral charge state of the defect). One expects the most stable charge state of these defects to be the -3 charge state, in which these electrons are added back into the lattice; this is indeed reflected in the low formation energy of this charge state, at least when the Fermi level is high (Figure 6.2). The occupied bonding states corresponding to the -3 charge state are located well below the top of the LHB, and hence hanging the charge state to -2, -1, or neutral requires taking electrons from states within the LHB; these missing electrons then manifest themselves in the form of small hole polarons on nearby Ti atoms. Figure 6.4 illustrates the situation for the $q = -2$ charge state of V_{Gd}, in which a single polaron is located adjacent to the vacancy. The -1 charge state has two polarons, and the neutral charge state has three.

In the -3 charge state of V_{Ti} (no polarons) the O atoms with a missing Ti neighbor shorten their remaining Ti-O bond, and the nearby Gd atoms displace inwards towards the vacancy. For V_{Gd} the predominant change in atomic structure is in the increase in bond angles of the Ti and O atoms surrounding the Gd vacancy.

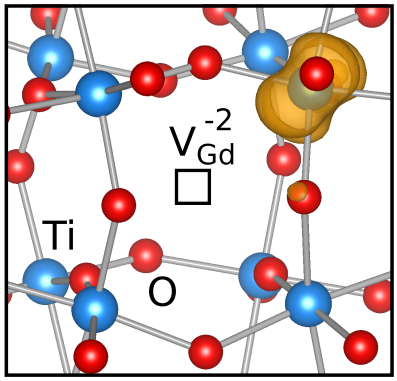

Figure 6.4: (Color online) Formation of a single small hole polaron for V_{Gd}^{-2}. The charge-density isosurface illustrating the wave function of the polaron state is set to 10% of the maximum value.

The formation energies for all charge states are shown in Figure 6.2; as expected, they are lowest under oxygen-poor conditions. Cation vacancies act as deep acceptors. V_{Ti} has transition levels at 0.92 eV $(0/-1)$, 1.03 eV $(-1/-2)$, and 1.29 eV $(-2/-3)$, and V_{Gd} at 0.77 eV $(0/-1)$, 0.85 eV $(-1/-2)$, and 1.34 eV $(-2/-3)$. The binding energy of the polarons to the defect center is clearly larger than it was for binding to a neutral oxygen vacancy, which can be attributed to the defect center now being triply negatively charged rather than neutral.

6.4.4 Antisites

$\mathrm{Ti_{Gd}}$ and $\mathrm{Gd_{Ti}}$ antisites have moderately low formation energies for both oxygen-rich and oxygen-poor conditions [Figures. 6.2(a) and (b)]. Ti has 4 valence electrons, and therefore one more electron than the Gd atom which it replaces (which transfers its

electrons to low-lying oxygen states). This extra electron is localized on the Ti atom, as for a Ti atom in bulk GTO, but with the electron in a state 0.38 eV below the LHB. We therefore expect the Ti_{Gd} defect to be stable in a neutral charge state, which is indeed the case over most of the range of Fermi levels. However, a hole polaron can occur in the vicinity of the defect, which effectively gives the appearance of the +1 charge state being stabilized when the Fermi level is below the (+1/0) transition level at 0.58 eV. The similarity of this transition-level value to the value of 0.55 eV for the bulk polaron indicates the interaction between the polaron and the Ti_{Gd} defect is quite weak, with a binding energy of only 0.03 eV.

For the case of Gd_{Ti} there is now a missing electron, and the number of LHBs is reduced by one. Again the defect is most stable in a neutral charge state, but a small polaron can be formed in the vicinity, seemingly stabilizing a $q = +1$ charge state with a (+1/0) transition level at 0.69 eV (corresponding to a binding energy for the polaron of 0.14 eV).

6.4.5 Oxygen interstitials

The oxygen interstitial is stable in a asymmetric dumbbell configuration for all charge states (0, −1 and −2). The adjacent O host atom is displaced, and the Ti-O-Ti bond angles for both O atoms are strongly distorted. The interstitial bonds to two Ti atoms and introduces two Ti-O bonding states 0.75 eV above the O $2p$ band. The −2 charge

state is the "natural" charge state for this defect. Forming a -1 or 0 charge state requires removing electrons, which need to be taken from the LHB, thus leading to the formation of one or two hole polarons; the transition levels are at 0.89 eV (0/+1) and 1.20 eV (+1/+2). Oxygen interstitials have higher formation energies than the other defects considered here (Figure 6.2), meaning that they are not likely to form.

6.5 Results: Impurities

The formation energies of impurities considered in our study are shown in Figure 6.5. We studied Sr substitutional impurities (Sr_{Gd}), H interstitials (H_i), and carbon-related defects: carbon interstitials (C_i), and substitutional C on Gd (C_{Gd}), Ti (C_{Ti}), and O sites (C_O). All these elements are candidates for unintentional doping that may occur during growth. H and C are ubiquitious impurities, and in particular are part of the metallorganic precursors used in hybrid MBE.[59] Sr is present during the growth of STO/GTO interfaces, and has also been used in intentional doping of GTO.[128,157,178,179]

6.5.1 Strontium

The calculated formation energy of Sr on a Gd site (Sr_{Gd}) is very low (Figure 6.5). Indeed, experimentally it is straightforward to dope GTO with Sr[157] or form $Gd_{1-x}Sr_xTiO_3$ alloys.[178,179] The atomic structure of Sr_{Gd} is similar to that of the Gd vacancy: the bond

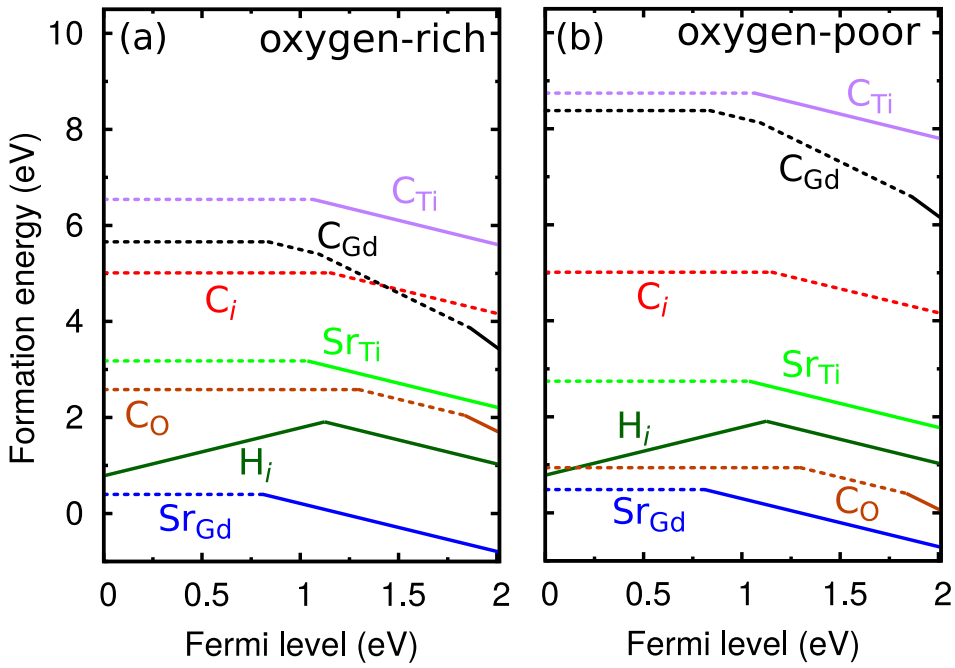

Figure 6.5: (Color online) Formation energies as a function of Fermi level for impurities in GTO under (a) oxygen-rich and (b) oxygen-poor conditions. The dotted lines indicate charge states corresponding to hole polarons bound to the impurity.

angles of the surrounding Ti and O atoms increase slightly. As expected from the 2+ valence of Sr (compared to 3+ for Gd), the impurity acts as an acceptor: over most of the range of Fermi levels it occurs in a -1 charge state, and a $(-1/0)$ transition level occurs at 0.81 eV. The neutral charge state is characterized by a small hole polaron on a neighboring Ti atom, with a binding energy of 0.26 eV. Evidently this binding energy is low enough to lead to easy ionization of the polaron and the observation of p-type conductivity in Sr-doped GTO.[179] Strontium on a Ti site behaves similarly to Sr_{Gd}, with a $(-1/0)$ transition level at 1.04 eV and the neutral charge state corresponding to a small polaron on a nearby Ti site, but with a significantly higher formation energy.

6.5.2 Hydrogen

The hydrogen interstitial can occur in two charge states. In the +1 charge state (essentially a proton) it bonds to an O atom, with a H-O bonding state resonant in the O $2p$ band, while in the -1 charge state it bonds to a Ti atom, introducing a H-Ti bonding state 1.33 eV above the O $2p$ band. The $(+1/-1)$ transition level occurs at 1.12 eV (Figure 6.5). Note that this is the first example we have encountered where a "true" charge-state transition level occurs, i.e., a transition that is truly associated with a change in the electronic structure of the defect center (including even a change in atomic structure, in this case), as opposed to merely binding a polaron to the center.

6.5.3 Carbon

Carbon substituting on an oxygen site (C_O) bonds with the two nearby Ti atoms, with slightly smaller Ti-C bond lengths (1.94 Å) than the comparable Ti-O bonds in the bulk (2.02 Å), which necessitates a larger Ti-C-Ti bond angle (150.3°) than the bulk Ti-O-Ti angle (140.4°). It introduces states between the O $2p$ band and the LHB; a spin-polarized pair of Ti-C bonding states (1.88 eV and 2.01 eV above the O $2p$ band), and four C lone-pair states (spin up states 1.93 eV and 2.17 eV above the O $2p$ band, and spin-down states at 2.09 eV and 2.34 eV). Since carbon is nominally a double acceptor when placed on the oxygen site, the "natural" charge state would be -2; Figure 6.5 shows that this charge state only occurs when the Fermi level is very high in the gap. In the -1 and neutral charge states, one or two holes are bound to the center. Figure 6.6 illustrates that in the neutral charge state, a polaron is localized on each of the Ti atoms bonded to C. The polarons are strongly bound to the center, as indicated by the high values of the transition level: at 1.30 eV for $(0/-1)$ and 1.84 eV for $(-1/-2)$ (Figure 6.5). C_O is the carbon-related defect with the lowest formation energy for both limits of chemical potentials.

The carbon interstitial bonds with a substitutional O atom in a dumbbell configuration, similar to O_i. The O atom is significantly displaced from its substitutional site, increasing the distortion of the Ti-O-Ti bond angle. The interstitial introduces four

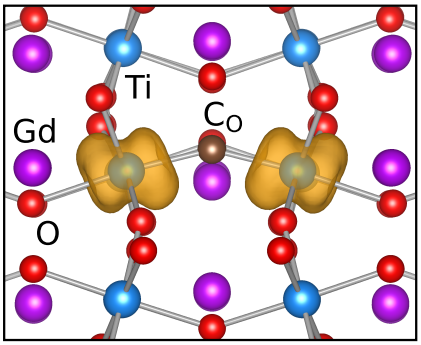

Figure 6.6: (Color online) Charge density of the small hole polaron states for C_O^0, with the isosurface set to 10% of the maximum value.

spin-polarized C states above the O $2p$ band (1.81 eV and 2.33 eV above for spin-up, and 2.00 eV and 2.67 eV for spin-down). Similar to O_i, the -2 charge state is expected to be the natural charge state for C_i. It turns out that the Fermi level would need to be pushed very high (into the UHB) to achieve this charge state: the $(-1/-2)$ level is at 2.09 eV. The $(0/-1)$ transition level occurs at 1.15 eV (Figure 6.5). In the -1 and neutral charge states, one or two polarons are bound to the defect center. C_i has high formation energies.

Carbon has 4 valence electrons and therefore might be expected to form a good "chemical match" when substituting on the Ti site; however, its size is significantly smaller, and the C atom moves off-site to form two 1.35 Å C-O bonds. For this bonding configuration of C_{Ti} we observe a doubly occupied C state 2.14 eV (spin-up) and 2.23 eV (spin-down) above the O $2p$ band. The -1 charge state is the "natural" charge state for this defect. Forming the 0 charge state leads to the formation of a hole polaron, with

$(-1/0)$ transition level at 1.07 eV [Figures 6.5(a) and (b)]. We note that the formation energy of C_{Ti} is quite high; this is mainly due to the chemical potential of Ti being high to maintain stability of GTO [Figure 6.1], which suppresses incorporation of impurities on the Ti site.

Carbon on a Gd site moves off-site and forms a 1.30 Å C-O bond. It introduces a spin-polarized C state (spin-up 0.15 eV above the O $2p$ band and spin-down 2.11 eV above). Its "natural" charge state is -3, and for the higher charge states polarons are localized on the nearby Ti atoms. The transition levels are at 0.84 eV $(0/-1)$, 1.09 eV $(-1/-2)$, and 1.87 eV $(-2/-3)$ [Figures 6.5(a) and (b)]. The formation energy of C_{Gd} is again high, for the same reasons related to chemical potentials as mentioned above for C_{Ti}.

6.6 Discussion

6.6.1 Formation energies, transition levels, and binding of hole polarons

For the native defects Figure 6.2 shows that under oxygen-rich conditions ($\mu_O = -3.61$ eV) the cation vacancies (V_{Ti} and V_{Gd}) have the lowest formation energies, and under oxygen-poor conditions ($\mu_O = -5.25$ eV) oxygen vacancies (V_O) and Gd antisites

(Gd_{Ti}) have the lowest formation energies. From Figure 6.5 we see that among the C-related defects C_O has by far the lowest formation energy.

For all the studied defects except H_i, *all* the charge transition levels represent the addition/removal of a small hole polaron. The polaron-related transition levels range from 0.58 eV [(+1/0) level for Ti_{Gd}] to 1.87 eV [(−2/−3) level for C_{Gd}]. Energies higher than the 0.55 eV (+1/0) transition level for the polaron in bulk GTO indicate that the polaron has a finite binding energy to the defect center. In the case of the oxygen vacancy or the antisites, where the defect center itself is neutral, these binding energies are quite small (see Section 6.4.4); in the other cases, the defect centers themselves are negatively charged centers, leading to stronger binding of the hole polarons.

6.6.2 Optical properties

In Section 5.3 we investigated the impact of small hole polarons on optical absorption. The transition corresponding to the excitation of a small hole polaron to a delocalized hole state is shown in the configuration coordinate diagram in Figure 6.7(a). The strain energy E_S is the energy difference between GTO in its equilibrium configuration and in the configuration corresponding to a small polaron, and the polaron self-trapping energy E_{ST} is the energy difference between the delocalized and localized hole in their relaxed atomic configurations.

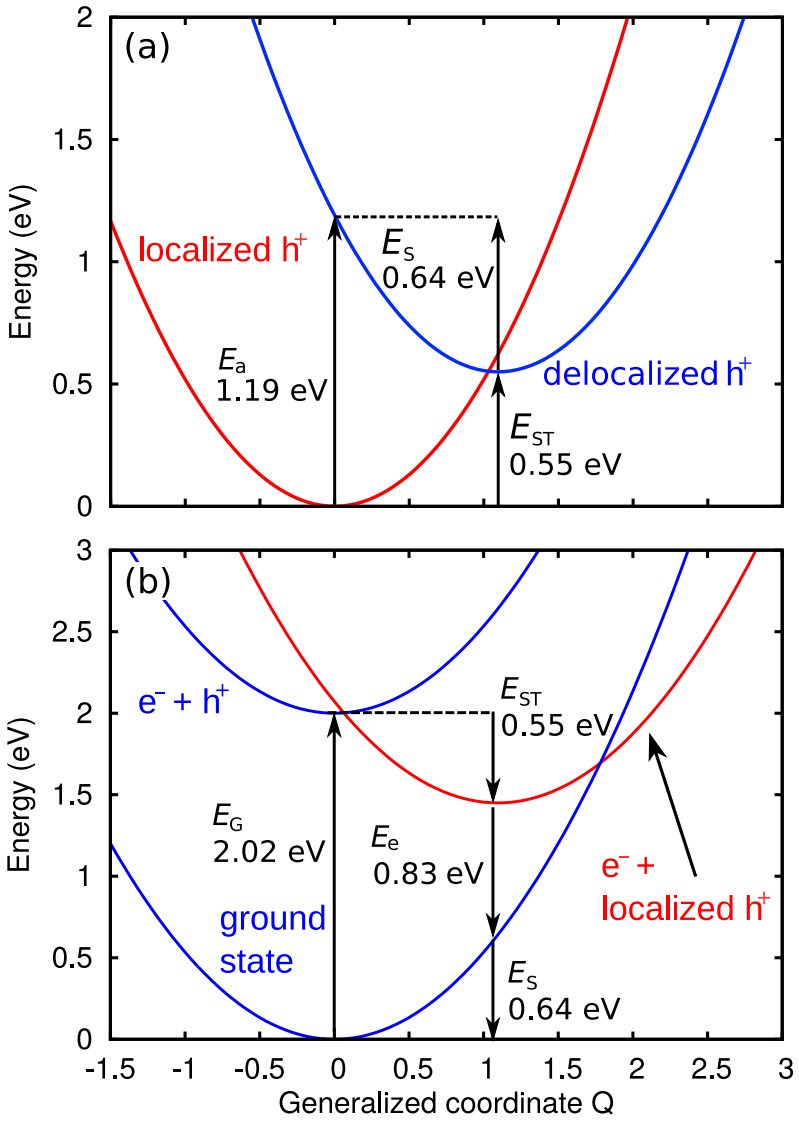

Figure 6.7: (Color online) Configuration coordinate diagrams for (a) the optical excitation of a hole from a localized to a delocalized state and (b) the recombination of an electron with a localized hole (small polaron). E_a is the absorption energy, E_G is the band-gap energy, E_{ST} the polaron self-trapping energy, E_e the optical emission energy, and E_S is the lattice energy cost (strain energy).

Regarding the role played by small hole polarons in luminescence, an electron excited to the UHB could recombine with a small hole polaron. For a polaron in bulk GTO we calculate the peak of this emission to occur around 0.8 eV, as illustrated in Figure 6.7(b). Since the defects introduce polaron transition levels that are higher than the bulk self-trapping energy E_{ST}=0.55 eV (i.e., the polaron is more strongly bound), the 0.8 eV constitutes an upper limit on the optical emission energy E_{e} (assuming that the strain energy E_{S} is not significantly affected by the proximity of the polaron to the defect). However, defect-related transitions at such low energies are more likely to be nonradiative than radiative.[180]

6.6.3 Defects as electron traps

GTO acts as the barrier layer that confines the 2DEG at STO/GTO interfaces;[9] it is therefore of interest to investigate the potential impact of defects on electron trapping. This could affect the performance of field effect transistors[181] and also of novel devices that would be based on tunneling through the GTO layer.[182] In the latter, electrons would tunnel between the 2DEG subbands at the interface and the subbands at another interface (in an STO/GTO/STO heterostructure) or a metal contact. In both cases tunneling electrons could be trapped/de-trapped at defects in GTO. It is therefore important to assess the alignment of the charge-state transition levels in GTO with the band structure of the STO.

Figure 6.8 shows this alignment for the defects in GTO with a low formation energy, using the previously calculated band offset between GTO and STO.[28] In the "flat-band" diagram of Figure 6.8, all transition levels (except that associated with a hole polaron in the bulk) are above the STO conduction-band minimum (CBM). However, in an actual heterostructure there will be band bending at the interface associated with the presence of the 2DEG in the GTO, thus raising the energy of the tunneling electrons. This band bending has been predicted to be as large as 1 eV,[84] meaning that the highest Fermi level position would be about 1.6 eV above the GTO LHB. The application of a voltage to control the tunneling process may also lower the energy of the transition levels relative to the tunneling electrons. Taken together, this means that the tunneling electrons may line up in energy with the defect-related trapping levels.

To assess the impact of defects on leakage currents or on tunneling through a GTO barrier layer, we consider trapping/de-trapping processes based on the formalism outlined by Fowler *et al.*,[183] which has previously been applied to study leakage currents in SiO_2.[184] Within this methodology, tunneling processes are approximated as Franck-Condon transitions, with atomic relaxation occurring after charge-state switching. Thus we define the "charge-state switching level" for trapping by adding the strain energy to the thermodynamic transition level [since this strain energy will be gained back only *after* the transition takes place, similar to the absorption event in Figure 6.7(a)]. Similarly, the level for detrapping is defined by subtracting the strain energy from the thermodynamic

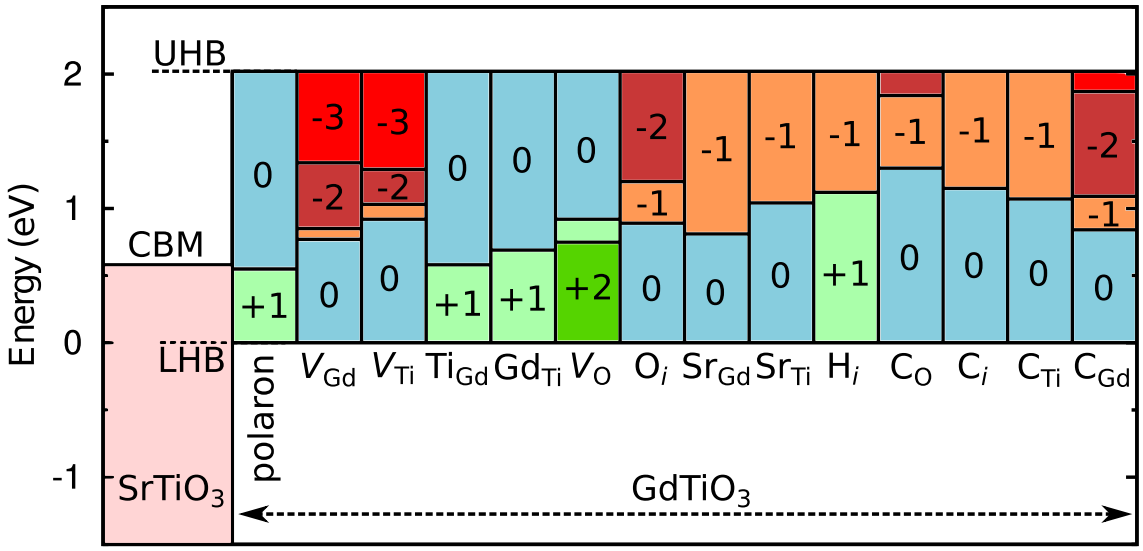

Figure 6.8: (Color online) Band alignment between STO and GTO, with positions of charge-state transition levels for native defects and impurities shown within the GTO gap. The zero of energy is set to the top of the GTO valence band (LHB), and the conduction-band minimum (CBM) of STO is indicated.

transition level [since the system will subsequently relax to the final state, lowering its energy by this amount of strain energy, similar to the emission event in Figure 6.7(b)]. Note that the strain energies for trapping and for detrapping are different.

As discussed in Sections 6.4 and 6.5, for all point defects except the hydrogen interstitial the transition levels are associated with small hole polarons. Therefore, we first illustrate these concepts for the case of a polaron in the bulk, and subsequently discuss how the binding of the polaron to a defect would affect the charge-state switching levels.

A hole polaron by itself gives a (+/0) transition level at 0.55 eV, and may recombine with a tunneling electron. This (+/0) transition corresponds to occupying the hole polaron state with an electron. This is similar to what happens when a small hole polaron transitions to a delocalized state via optical absorption [as illustrated in Figure 6.7(a)]: in that case, an electron at the top of the LHB is excited to occupy the polaron state, leaving behind a delocalized hole. The energy E_a required for the optical absorption process is the sum of the polaron self-trapping energy $E_{\mathrm{ST}} = 0.55$ eV and the strain energy $E_{\mathrm{S}} = 0.64$ eV. In the case of electron tunneling, the electron would thus need to be injected at an energy 0.55 eV + 0.64 eV = 1.19 eV above the LHB, as illustrated in Figure 6.9(a). The charge-state switching level for electron trapping is thus at 1.19 eV. After the electron has filled the polaron state, lattice relaxation occurs (through phonon emission), and the final state corresponds to the perfect GTO lattice—i.e., there is no detrapping level in this case.

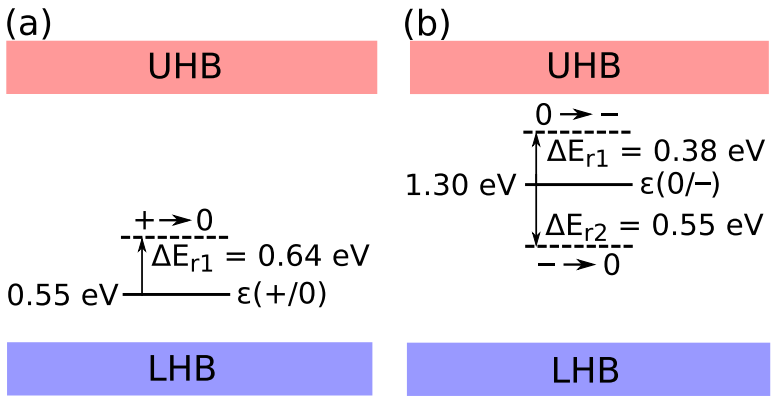

Figure 6.9: (Color online) Thermodynamic transition levels and charge-state switching levels for trapping/detrapping of an electron, for (a) the $(+1/0)$ transition for a polaron in bulk GTO and (b) the $(0/-1)$ transition for C_O. The arrows indicate a transition in which the atomic configuration is kept fixed to that of the initial state (unlike the thermodynamic transition levels, for which the atomic configuration of the final state is relaxed). $E_{S(1,2)}$ are the relaxation energies between the two charge states.

Now we examine the electron-trapping process in the presence of defects. To illustrate this we use the 1.30 eV $(0/-1)$ transition level for C_O, the lowest-energy C-related defect. Since the Fermi level is likely to lie below 1.30 eV, C_O is initially in the neutral charge state and two polarons are localized on the nearest-neighbor Ti atoms (C_O^0). The difference in energy between C_O^- in its equilibrium configuration and C_O^- in the configuration of C_O^0 (E_{S1}) is 0.38 eV. Adding this strain energy to the transition level gives a 1.68 eV charge-state switching level for the $0 \rightarrow -$ trapping process [Figure 6.9(b)].

After an electron is trapped, C_O is in the negative charge state, and the defect will relax to its ground-state atomic configuration. We now address whether the electron would remain trapped on the defect, or be able to tunnel out. To remove the electron, a

transition to the neutral charge state would need to occur. Again, the thermodynamic transition level is at 1.30 eV, but now we need to take into account the strain energy corresponding to the difference in energy between C_O^0 in its equilibrium configuration and C_O^0 in the configuration of C_O^- (E_{S2}). This energy, E_{S2}, is 0.55 eV. Subtracting this strain energy from the transition level gives a charge-state switching level of 0.75 eV for the $- \rightarrow 0$ detrapping process, as indicated in Figure 6.9(b). Empty states would need to be available at that energy on the "exit" side of the barrier in order for the electron to be able to escape from the C_O trap.

For the range of possible Fermi levels, which we estimated above to be between 0.6 to 1.6 eV, multiple defects occur in charge states that stabilize small hole polarons. These defects may act as trapping centers once a voltage is applied: an electron tunnels into the defect, fills a hole polaron, and the defect switches to another charge state. For this electron to become detrapped, there must be an empty state available on the other side of the junction. It is evident from Figure 6.9(b) that for this criterion to be satisfied, the voltage swing applied to the device must therefore be greater than the sum of the strain energies associated with the charge-state switching level; in the example of C_O $(0/-1)$, this would be 0.38 eV + 0.55 eV = 0.93 eV. Assuming that the strain energies are similar for all the defects (except H_i), since all the transition levels involve small polarons, we conclude that defects may only contribute to tunneling for applied voltage swings greater than about 0.9 V. For smaller applied voltage swings, there are no empty

states available on the other side of the junction, and the defect level may act as a trapping center, i.e., electrons would be trapped on the defect without the possibility of detrapping; this would lead to charging of the GTO layer, which could be detrimental to device operation.

6.7 Summary

We have investigated the electronic and optical properties of intrinsic and extrinsic point defects in GTO using hybrid density functional theory. Results for formation energies of native defects are summarized in Figure 6.2. It should be noted that this figure should be interpreted somewhat differently from the usual case of semiconductors or band insulators:[49] the kinks in the curves, which define the positions of the defect levels according to Eq. (6.2), do *not* correspond to adding or removing electrons from electronic states within the band gap here; rather, they represent the formation of polarons in the vicinity of the defect, while the center of the defect remains in the charge state in which the bonding states are fully occupied. The same is true for all of the impurities in Figure 6.5, except interstitial H. Among the native defects, the cation vacancies have the lowest formation energies under oxygen-rich conditions and the oxygen vacancy under oxygen-poor conditions. Among candidate impurities, Sr_{Gd} is an acceptor with low

formation energy, H_i has a level in the middle of the gap, and C_O has the lowest energy among C-related defects.

The transition levels for all defects (except H_i) are related to small hole polarons. In the bulk, the (+1/0) transition level for a polaron is at 0.55 eV. The transition levels for defects are higher in energy because of the binding of the polaron to the defect. The defects can act as electron traps or sources of leakage current in GTO barrier layers in devices. We find that defects would only act as tunneling centers (enabling trapping and detrapping of electrons) if applied voltage swings are greater than about 0.9 V. Several of the defects can lead to electron trapping and charging of the GTO layer.

Chapter 7

Summary and future directions

In this work, we studied interface, bulk, and defect properties of perovskite oxides ("complex oxides") exhibiting the formation of an interface two-dimensional electron gas (2DEG). This 2DEG arises because of an interface polar discontinuity, which leads to a sheet of donors right at the interface. Its density is incredibly high at 1/2 electrons per unit cell area, corresponding to about 3×10^{14} cm^{-2}, an order of magnitude higher than 2DEG densities achievable in conventional semiconductor systems. This has drawn a large amount of attention to these complex oxides, and the efforts in this thesis centered on understanding the formation of this 2DEG, and how to use it in electronic devices.

We began by outlining a set of criteria for the use of this 2DEG in devices. In that context we calculated the band alignment between a variety of perovskite oxides that may give rise to a 2DEG, predicting new interface candidates. Calculating the band

alignment of $SmTiO_3$, a new material used in complex oxide heterostrucures,[10] and comparing with experimental measurements, is currently in progress as a continuation of this work.

A "grand challenge" of complex-oxide electronics is identifying and fabricating an interface with good lattice matching, which can give rise to a high-mobility 2DEG that can be modulated via a gate voltage. With that in mind, $BaSnO_3$ was highlighted as a promising 2DEG host material, having high mobility and a low-lying conduction band, but with the drawback of low density of states. Subsequent work in which I participated, led by my colleague K. Krishnaswamy in the Van de Walle group, evaluated $BaSnO_3$ as a channel material and used Schrödinger-Poisson simulations to understand the behavior of the 2DEG at the interface.[185] Future work in this direction is calculating band-edge deformation potentials, quantifying by how much the valence- and conduction-band edges shift on an absolute scale under strain, for candidate oxide materials such as $BaSnO_3$.

We next performed a detailed study of GTO/STO/GTO heterostructures (as grown in the Stemmer group at UCSB), where each interface contributes a 2DEG in the STO. These heterostructures display a metal-to-insulator transition with layer thickness; the system becomes insulating for one or two STO layers. This transition has been attributed to on-site Mott-Hubbard-type correlation physics: once the 3D density is high enough, the on-site electron-electron repulsion causes localization.[27] Distortions of the

atomic positions are also found to accompany the transition.[10,73] We found that the insulating behavior can occur even in *bulk* STO as a consequence of extremely high doping, making the material into a Mott insulator with one electron localized on every second Ti atom. Once the layer thickness is small enough, this localized phase becomes lower in energy than the competing delocalized (metallic) phase, leading to localized electrons in the interface TiO_2 layers. This fundamental understanding of the transition is key to potentially designing a "Mott field effect transistor" based on a GTO/STO/GTO heterostructure, where small changes in the 2DEG electron concentration in the STO (by applying a voltage) could bring the system across the transition.

In the process of studying the STO/GTO interface, we noticed that our calculated gap (2 eV) for GTO was significantly larger than what was reported in the literature based on optical absorption measurements (0.7 eV). Experimental collaborators in the Jena group at the University of Notre Dame (now at Cornell University) measured a photoluminesence (PL) peak at 1.8 eV, setting a lower limit on the band gap in agreement with our calculated value of 2 eV. The discrepancy with the 0.7 eV value from optical absorption prompted further investigation of the electronic properties of GTO. Given that GTO is reported to contain small hole polarons (leading to *p*-type hopping conductivity), we investigated the role hole polarons play in optical absorption. A joint study with experimentalists at UCSB (Allen group) found an excellent match between the calculated and measured excitation energy of small hole polarons, confirming that

they are indeed the source of the 0.7 eV optical absorption signal. As *all* the rare-earth titanates have reported band gaps in the range 0.2-0.7 eV based on optical absorption, and display *p*-type hopping conductivity, it is likely that the gap of all these materials must be revised. PL measurements and optical absorption measurements of small hole polaron excitations of other rare-earth titanates, in particular $LaTiO_3$, which has the smallest reported onset of optical absorption, would confirm or disprove this hypothesis. Another approach to investigate the connection between small hole polarons and optical absorption is to study their behavior under pressure, comparing the calculated optical excitations with optical absorption measurements.[186]

Lastly, we studied native defects and impurities in GTO in order to understand how the small polarons arise and affect physical properties. Surprisingly, *all* defects are either neutral or acceptors (except hydrogen interstitials), and have *only* small hole polaron-related thermodynamic transition levels. We considered how the defects may influence possible devices using GTO as a tunnel barrier. We find that the defects can act as electron traps or sources of leakage current, but that they only act as tunneling centers (enabling trapping and detrapping of electrons) if applied voltage swings are greater than about 0.9 V. However, several of the defects can lead to electron trapping and charging of the GTO layer.

To conclude, our initial work on the formation of complex oxide 2DEGs and how to harness this for device applications lead us down a path to understand Mott metal-

insulator transitions, the impact of small hole polarons in these Mott materials, and how such polarons form. This fundamental research is therefore motivated by a well-defined application, and serves as a nice illustration of the power of first-principles calculations in building understanding of new and unexplored materials.

Bibliography

[1] M. Ieong, B. Doris, J. Kedzierski, K. Rim, and M. Yang. Silicon device scaling to the sub-10-nm regime. *Science*, 306(5704):2057, 2004.

[2] M.-K. Wu, J. R. Ashburn, C. J. Torng, P. H. Hor, R. L. Meng, L. Gao, Z. J. Huang, Y. Q. Wang, and C. W. Chu. Superconductivity at 93 K in a new mixed-phase Y-Ba-Cu-O compound system at ambient pressure. *Physical Review Letters*, 58(9):908, 1987.

[3] M. Imada, A. Fujimori, and Y. Tokura. Metal-insulator transitions. *Reviews of Modern Physics*, 70(4):1039, 1998.

[4] G. H. Haertling. Ferroelectric ceramics: history and technology. *J. Am. Ceram. Soc.*, 82(4):797–818, 1999.

[5] S. Jin, T. H. Tiefel, M. McCormack, R. A. Fastnacht, R. Ramesh, and L. H. Chen. Thousandfold change in resistivity in magnetoresistive La-Ca-Mn-O films. *Science*, 264(5157):413–415, 1994.

[6] A. Ohtomo and H. Y. Hwang. A high-mobility electron gas at the $LaAlO_3/SrTiO_3$ heterointerface. *Nature*, 427(6973):423–426, 2004.

[7] A. Brinkman, M. Huijben, M. Van Zalk, J. Huijben, U. Zeitler, J. C. Maan, W. G. Van der Wiel, G. Rijnders, D. H. A. Blank, and H. Hilgenkamp. Magnetic effects at the interface between non-magnetic oxides. *Nature Materials*, 6(7):493–496, 2007.

[8] M. Huijben, A. Brinkman, G. Koster, G. Rijnders, H. Hilgenkamp, and D. H. A. Blank. Structure–property relation of $SrTiO_3/LaAlO_3$ interfaces. *Advanced Materials*, 21(17):1665–1677, 2009.

[9] P. Moetakef, T. A. Cain, D. G. Ouellette, J. Y. Zhang, D. O Klenov, A. Janotti, C. G. Van de Walle, S. Rajan, S. J. Allen, and S. Stemmer. Electrostatic car-

rier doping of $GdTiO_3/SrTiO_3$ interfaces. *Applied Physics Letters*, 99(23):232116, 2011.

[10] J. Y. Zhang, C. A. Jackson, R. Chen, S. Raghavan, P. Moetakef, L. Balents, and S. Stemmer. Correlation between metal-insulator transitions and structural distortions in high-electron-density $SrTiO_3$ quantum wells. *Physical Review B*, 89(7):075140, 2014.

[11] N. Reyren, S. Thiel, A. D. Caviglia, L. F. Kourkoutis, G. Hammerl, C. Richter, C. W. Schneider, T. Kopp, A.-S. Rüetschi, D. Jaccard, et al. Superconducting interfaces between insulating oxides. *Science*, 317(5842):1196–1199, 2007.

[12] J. Son, S. Rajan, S. Stemmer, and S. J. Allen. A heterojunction modulation-doped Mott transistor. *Journal of Applied Physics*, 110(8):084503, 2011.

[13] K. Yoshimatsu, K. Horiba, H. Kumigashira, T. Yoshida, A. Fujimori, and M. Oshima. Metallic quantum well states in artificial structures of strongly correlated oxide. *Science*, 333(6040):319–322, 2011.

[14] D. H. Lowndes, D. B. Geohegan, A. A. Puretzky, D. P. Norton, and C. M. Rouleau. Synthesis of novel thin-film materials by pulsed laser deposition. *Science*, 273(5277):898–903, 1996.

[15] D. G. Schlom, J. H. Haeni, J. Lettieri, C. D. Theis, W. Tian, J. C. Jiang, and X. Q. Pan. Oxide nano-engineering using MBE. *Materials Science and Engineering: B*, 87(3):282–291, 2001.

[16] V. M. Goldschmidt. Die Gesetze der Krystallochemie. *Naturwissenschaften*, 14(21):477–485, 1926.

[17] C. J. Howard and H. T. Stokes. Group-theoretical analysis of octahedral tilting in perovskites. *Acta Crystallographica Section B: Structural Science*, 54(6):782–789, 1998.

[18] R. H. Mitchell. *Perovskites: modern and ancient*. Almaz Press Thunder Bay, 2002.

[19] N. F. Mott. The basis of the electron theory of metals, with special reference to the transition metals. *Proceedings of the Physical Society. Section A*, 62(7):416, 1949.

[20] B. Himmetoglu, A. Janotti, L. Bjaalie, and C. G. Van de Walle. Interband and polaronic excitations in $YTiO_3$ from first principles. *Physical Review B*, 90(16):161102, 2014.

[21] A. Georges, G. Kotliar, W. Krauth, and M. J. Rozenberg. Dynamical mean-field theory of strongly correlated fermion systems and the limit of infinite dimensions. *Reviews of Modern Physics*, 68(1):13, 1996.

[22] U. Mishra and J. Singh. *Semiconductor device physics and design*. Springer Science & Business Media, 2007.

[23] A. P. Kajdos, D. G. Ouellette, T. A. Cain, and S. Stemmer. Two-dimensional electron gas in a modulation-doped $SrTiO_3/Sr(Ti,Zr)O_3$ heterostructure. *Applied Physics Letters*, 103(8):082120, 2013.

[24] W. A. Harrison. *Elementary electronic structure*. World Scientific, 1999.

[25] W. A. Harrison, E. A. Kraut, J. R. Waldrop, and R. W. Grant. Polar heterojunction interfaces. *Physical Review B*, 18(8):4402, 1978.

[26] A. Janotti, L. Bjaalie, L. Gordon, and C. G. Van de Walle. Controlling the density of the two-dimensional electron gas at the $SrTiO_3/LaAlO_3$ interface. *Physical Review B*, 86(24):241108, 2012.

[27] P. Moetakef, C. A. Jackson, J. Hwang, L. Balents, S. J. Allen, and S. Stemmer. Toward an artificial Mott insulator: Correlations in confined high-density electron liquids in $SrTiO_3$. *Physical Review B*, 86(20):201102, 2012.

[28] L. Bjaalie, B. Himmetoglu, L. Weston, A. Janotti, and C. G. Van de Walle. Oxide interfaces for novel electronic applications. *New Journal of Physics*, 16(2):025005, 2014.

[29] R. M. Martin. *Electronic structure: basic theory and practical methods*. Cambridge university press, 2004.

[30] P. Hohenberg and W. Kohn. Inhomogeneous electron gas. *Physical Review*, 136(3B):B864, 1964.

[31] W. Kohn and L. J. Sham. Self-consistent equations including exchange and correlation effects. *Physical Review*, 140(4A):A1133, 1965.

[32] D. M. Ceperley and B. J. Alder. Ground state of the electron gas by a stochastic method. *Physical Review Letters*, 45(7):566, 1980.

[33] J. P. Perdew and A. Zunger. Self-interaction correction to density-functional approximations for many-electron systems. *Physical Review B*, 23(10):5048, 1981.

[34] J. P. Perdew, K. Burke, and M. Ernzerhof. Generalized gradient approximation made simple. *Physical Review Letters*, 77(18):3865, 1996.

[35] B. Himmetoglu, A. Floris, S. Gironcoli, and M. Cococcioni. Hubbard-corrected DFT energy functionals: The LDA + U description of correlated systems. *International Journal of Quantum Chemistry*, 114(1):14–49, 2014.

[36] J. Hubbard. Electron correlations in narrow energy bands. In *Proceedings of the Royal Society of London A: Mathematical, Physical and Engineering Sciences*, volume 276, pages 238–257. The Royal Society, 1963.

[37] V. I. Anisimov, F. Aryasetiawan, and A. I. Lichtenstein. First-principles calculations of the electronic structure and spectra of strongly correlated systems: the LDA + U method. *Journal of Physics: Condensed Matter*, 9(4):767, 1997.

[38] A. I. Liechtenstein, V. I. Anisimov, and J. Zaanen. Density-functional theory and strong interactions: Orbital ordering in Mott-Hubbard insulators. *Physical Review B*, 52(8):R5467, 1995.

[39] A. D. Becke. A new mixing of Hartree-Fock and local density functional theories. *J. Chem. Phys.*, 98(2):1372, 1993.

[40] J. Heyd, G. E. Scuseria, and M. Ernzerhof. Erratum: Hybrid functionals based on a screened Coulomb potential [J. Chem. Phys. 118, 8207 (2003)]. *J. Chem. Phys.*, 124(21):219906, 2006.

[41] L. Cláudio de Carvalho, A. Schleife, and F. Bechstedt. Influence of exchange and correlation on structural and electronic properties of AlN, GaN, and InN polytypes. *Physical Review B*, 84(19):195105, 2011.

[42] J. He and C. Franchini. Screened hybrid functional applied to $3d^0 \rightarrow 3d^8$ transition-metal perovskites $LaMO_3$ (M= Sc–Cu): Influence of the exchange mixing parameter on the structural, electronic, and magnetic properties. *Physical Review B*, 86(23):235117, 2012.

[43] J. Paier, M. Marsman, K. Hummer, G. Kresse, I. C. Gerber, and J. G. Angyán. Screened hybrid density functionals applied to solids. *J. Chem. Phys.*, 124(15):154709, 2006.

[44] P. Rivero, I. de P. R. Moreira, G. E. Scuseria, and F. Illas. Description of magnetic interactions in strongly correlated solids via range-separated hybrid functionals. *Physical Review B*, 79(24):245129, 2009.

[45] M. Levy, J. P. Perdew, and V. Sahni. Exact differential equation for the density and ionization energy of a many-particle system. *Physical Review A*, 30(5):2745, 1984.

[46] W. G. Aulbur, L. Jönsson, and J. W. Wilkins. Quasiparticle calculations in solids. Academic Press, 1999.

[47] P. Mori-Sánchez, A. J. Cohen, and W. Yang. Localization and delocalization errors in density functional theory and implications for band-gap prediction. *Physical Review Letters*, 100(14):146401, 2008.

[48] J. P. Perdew, R. G. Parr, M. Levy, and J. L. Balduz Jr. Density-functional theory for fractional particle number: derivative discontinuities of the energy. *Physical Review Letters*, 49(23):1691, 1982.

[49] C. Freysoldt, B. Grabowski, T. Hickel, J. Neugebauer, G. Kresse, A. Janotti, and C. G. Van de Walle. First-principles calculations for point defects in solids. *Reviews of Modern Physics*, 86(1):253, 2014.

[50] L. Hedin. New Method for Calculating the One-Particle Green's Function with Application to the Electron-Gas Problem. *Physical Review*, 139:A796–A823, Aug 1965.

[51] G. Kresse and J. Furthmüller. Efficient iterative schemes for *ab initio* total-energy calculations using a plane-wave basis set. *Physical Review B*, 54(16):11169, 1996.

[52] P. E. Blöchl. Projector augmented-wave method. *Physical Review B*, 50(24):17953, 1994.

[53] A. Baldereschi. Mean-Value Point in the Brillouin Zone. *Physical Review B*, 7(12):5212, 1973.

[54] D. J. Chadi and M. Cohen. Special Points in the Brillouin Zone. *Physical Review B*, 8(12):5747, 1973.

[55] H. J. Monkhorst and J. D. Pack. Special points for Brillouin-zone integrations. *Physical Review B*, 13(12):5188, 1976.

[56] P. Moetakef, J. Y. Zhang, S. Raghavan, A. P. Kajdos, and S. Stemmer. Growth window and effect of substrate symmetry in hybrid molecular beam epitaxy of a Mott insulating rare earth titanate. *Journal of Vacuum Science & Technology A*, 31(4):041503, 2013.

[57] B. Jalan, P. Moetakef, and S. Stemmer. Molecular beam epitaxy of $SrTiO_3$ with a growth window. *Applied Physics Letters*, 95(3):032906, 2009.

[58] B. Jalan, R. Engel-Herbert, N. J. Wright, and S. Stemmer. Growth of high-quality $SrTiO_3$ films using a hybrid molecular beam epitaxy approach. *Journal of Vacuum Science and Technology. A, International Journal Devoted to Vacuum, Surfaces, and Films*, 27(3), 2009.

[59] P. Moetakef, D. G. Ouellette, J. Y. Zhang, T. A. Cain, S. J. Allen, and S. Stemmer. Growth and properties of $GdTiO_3$ films prepared by hybrid molecular beam epitaxy. *Journal of Crystal Growth*, 355(1):166–170, 2012.

[60] D. G. Schlom, L.-Q. Chen, X. Pan, A. Schmehl, and M. A. Zurbuchen. A thin film approach to engineering functionality into oxides. *Journal of the American Ceramic Society*, 91(8):2429–2454, 2008.

[61] C.-J. Eklund, C. J. Fennie, and K. M. Rabe. Strain-induced ferroelectricity in orthorhombic $CaTiO_3$ from first principles. *Physical Review B*, 79(22):220101, 2009.

[62] W. Siemons, G. Koster, H. Yamamoto, W. A. Harrison, G. Lucovsky, T. H. Geballe, D. H. A. Blank, and M. R. Beasley. Origin of charge density at $LaAlO_3$ on $SrTiO_3$ heterointerfaces: Possibility of intrinsic doping. *Physical Review Letters*, 98(19):196802, 2007.

[63] N. C. Bristowe, P. B. Littlewood, and E. Artacho. Surface defects and conduction in polar oxide heterostructures. *Physical Review B*, 83(20):205405, 2011.

[64] Y. Li, S. N. Phattalung, S. Limpijumnong, J. Kim, and J. Yu. Formation of oxygen vacancies and charge carriers induced in the n-type interface of a $LaAlO_3$ overlayer on $SrTiO_3$ (001). *Physical Review B*, 84(24):245307, 2011.

[65] A. Kalabukhov, R. Gunnarsson, J. Börjesson, E. Olsson, T. Claeson, and D. Winkler. Effect of oxygen vacancies in the $SrTiO_3$ substrate on the electrical properties of the $LaAlO_3/SrTiO_3$ interface. *Physical Review B*, 75(12):121404, 2007.

[66] G. Herranz, M. Basletić, M. Bibes, C. Carrétéro, E. Tafra, E. Jacquet, K. Bouzehouane, C. Deranlot, A. Hamzić, J.-M. Broto, A. Barthélémy, and A. Fert. High mobility in $LaAlO_3/SrTiO_3$ heterostructures: Origin, dimensionality, and perspectives. *Physical Review Letters*, 98(21):216803, 2007.

[67] J. B. Varley, A. Janotti, and C. G. Van de Walle. Hydrogenated vacancies and hidden hydrogen in $SrTiO_3$. *Physical Review B*, 89(7):075202, 2014.

[68] M. Choi, A. Janotti, and C. G. Van de Walle. Native point defects and dangling bonds in α-Al2O_3. *Journal of Applied Physics*, 113(4):044501, 2013.

[69] A. Janotti, J. B. Varley, P. Rinke, N. Umezawa, G. Kresse, and C. G. Van de Walle. Hybrid functional studies of the oxygen vacancy in TiO_2. *Physical Review B*, 81(8):085212, 2010.

[70] N. Nakagawa, H. Y. Hwang, and D. A. Muller. Why some interfaces cannot be sharp. *Nature Materials*, 5(3):204–209, 2006.

[71] L. Qiao, T. C. Droubay, T. Varga, M. E. Bowden, V. Shutthanandan, Z. Zhu, T. C. Kaspar, and S. A. Chambers. Epitaxial growth, structure, and intermixing at the $LaAlO_3/SrTiO_3$ interface as the film stoichiometry is varied. *Physical Review B*, 83(8):085408, 2011.

[72] E. Breckenfeld, N. Bronn, J. Karthik, A. R. Damodaran, S. Lee, N. Mason, and L. W. Martin. Effect of growth induced (non) stoichiometry on interfacial conductance in $LaAlO_3/SrTiO_3$. *Physical Review Letters*, 110(19):196804, 2013.

[73] J. Y. Zhang, J. Hwang, S. Raghavan, and S. Stemmer. Symmetry lowering in extreme-electron-density perovskite quantum wells. *Physical Review Letters*, 110(25):256401, 2013.

[74] S. Thiel, G. Hammerl, A. Schmehl, C. W. Schneider, and J. Mannhart. Tunable quasi-two-dimensional electron gases in oxide heterostructures. *Science*, 313(5795):1942–1945, 2006.

[75] J. Lee and A. Demkov. Charge origin and localization at the n-type $SrTiO_3/LaAlO_3$ interface. *Physical Review B*, 78(19):193104, 2008.

[76] R. Pentcheva and W. E. Pickett. Electronic phenomena at complex oxide interfaces: insights from first principles. *Journal of Physics: Condensed Matter*, 22(4):043001, 2010.

[77] K. Krishnaswamy, C. E. Dreyer, A. Janotti, and C. G. Van de Walle. First-principles study of surface charging in $LaAlO_3/SrTiO_3$ heterostructures. *Physical Review B*, 92(8):085420, 2015.

[78] M. Basletic, J.-L. Maurice, C. Carrétéro, G. Herranz, O. Copie, M. Bibes, É. Jacquet, K. Bouzehouane, S. Fusil, and A. Barthélémy. Mapping the spatial distribution of charge carriers in $LaAlO_3/SrTiO_3$ heterostructures. *Nature Materials*, 7(8):621–625, 2008.

[79] C. G. Van de Walle and D. Segev. Microscopic origins of surface states on nitride surfaces. *Journal of Applied Physics*, 101(8):081704, 2007.

[80] K. Krishnaswamy, C. E. Dreyer, A. Janotti, and C. G. Van de Walle. Structure and energetics of $LaAlO_3$ (001) surfaces. *Physical Review B*, 90(23):235436, 2014.

[81] M. Huijben, G. Rijnders, D. H. A. Blank, S. Bals, S. Van Aert, J. Verbeeck, G. Van Tendeloo, A. Brinkman, and H. Hilgenkamp. Electronically coupled complementary interfaces between perovskite band insulators. *Nature Materials*, 5(7):556–560, 2006.

[82] A. Janotti, D. Steiauf, and C. G. Van de Walle. Strain effects on the electronic structure of $SrTiO_3$: Toward high electron mobilities. *Physical Review B*, 84(20):201304, 2011.

[83] G. Khalsa and A. H. MacDonald. Theory of the $SrTiO_3$ surface state two-dimensional electron gas. *Physical Review B*, 86(12):125121, 2012.

[84] H. Peelaers, K. Krishnaswamy, L. Gordon, D. Steiauf, A. Sarwe, A. Janotti, and C. G. Van de Walle. Impact of electric-field dependent dielectric constants on two-dimensional electron gases in complex oxides. *Applied Physics Letters*, 107(18):183505, 2015.

[85] R. A. Van der Berg, P. W. M. Blom, J. F. M. Cillessen, and R. M. Wolf. Field dependent permittivity in metal-semiconducting $SrTiO_3$ Schottky diodes. *Applied Physics Letters*, 66(6):697–699, 1995.

[86] M. B. Steer and W. D. Palmer. *Multifunctional adaptive microwave circuits and systems*. Scitech Pub Incorporated, 2009.

[87] M. Heinrich, H.-A. Krug von Nidda, V. Fritsch, and A. Loidl. Heavy-fermion formation at the metal-to-insulator transition in $Gd_{1-x}Sr_xTiO_3$. *Physical Review B*, 63(19):193103, 2001.

[88] P. G. Moses, M. Miao, Q. Yan, and C. G. Van de Walle. Hybrid functional investigations of band gaps and band alignments for AlN, GaN, InN, and InGaN. *The Journal of chemical physics*, 134(8):084703, 2011.

[89] K. Van Benthem, C. Elsässer, and R. H. French. Bulk electronic structure of $SrTiO_3$: Experiment and theory. *Journal of Applied Physics*, 90(12):6156–6164, 2001.

[90] S.-G. Lim, S. Kriventsov, T. N. Jackson, J. H. Haeni, D. G. Schlom, A. M. Balbashov, R. Uecker, P. Reiche, J. L. Freeouf, and G. Lucovsky. Dielectric functions and optical bandgaps of high-K dielectrics for metal-oxide-semiconductor field-effect transistors by far ultraviolet spectroscopic ellipsometry. *Journal of applied physics*, 91(7):4500–4505, 2002.

[91] J. O. McCaldin, T. C. McGill, and C. A. Mead. Correlation for III-V and II-VI semiconductors of the Au Schottky barrier energy with anion electronegativity. *Physical Review Letters*, 36(1):56, 1976.

[92] A. Franciosi and C. G. Van de Walle. Heterojunction band offset engineering. *Surface Science Reports*, 25(1):1–140, 1996.

[93] C. G. Van de Walle and R. M. Martin. Theoretical calculations of heterojunction discontinuities in the Si/Ge system. *Physical Review B*, 34(8):5621, 1986.

[94] C. G. Van de Walle and J. Neugebauer. Universal alignment of hydrogen levels in semiconductors, insulators and solutions. *Nature*, 423(6940):626–628, 2003.

[95] J. Son, P. Moetakef, B. Jalan, O. Bierwagen, N. J. Wright, R. Engel-Herbert, and S. Stemmer. Epitaxial $SrTiO_3$ films with electron mobilities exceeding 30,000 cm^2 V^{-1} s^{-1}. *Nature Materials*, 9(6):482–484, 2010.

[96] H. P. R. Frederikse, W. R. Thurber, and W. R. Hosler. Electronic transport in strontium titanate. *Physical Review*, 134(2A):A442, 1964.

[97] S. Mehrotra, M. Povolotskyi, D. C. Elias, T. Kubis, J. J. M. Law, M. J. W. Rodwell, and G. Klimeck. Simulation study of thin-body ballistic n-MOSFETs involving transport in mixed-L valleys. *Electron Device Letters, IEEE*, 34(9):1196–1198, 2013.

[98] M. Reiche, O. Moutanabbir, J. Hoentschel, U. M. Gösele, S. Flachowsky, and M. Horstmann. Strained silicon devices. In *Solid State Phenomena*, volume 156, pages 61–68. Trans Tech Publ, 2010.

[99] B. Himmetoglu, A. Janotti, H. Peelaers, A. Alkauskas, and C. G. Van de Walle. First-principles study of the mobility of $SrTiO_3$. *Physical Review B*, 90(24):241204, 2014.

[100] R. Pentcheva and W. E. Pickett. Charge localization or itineracy at $LaAlO_3/SrTiO_3$ interfaces: Hole polarons, oxygen vacancies, and mobile electrons. *Physical Review B*, 74(3):035112, 2006.

[101] J.-M. Albina, M. Mrovec, B. Meyer, and C. Elsässer. Structure, stability, and electronic properties of $SrTiO_3/LaAlO_3$ and $SrTiO_3/SrRuO_3$ interfaces. *Physical Review B*, 76(16):165103, 2007.

[102] Z. S. Popović, S. Satpathy, and R. M. Martin. Origin of the two-dimensional electron gas carrier density at the $LaAlO_3$ on $SrTiO_3$ interface. *Physical Review Letters*, 101(25):256801, 2008.

[103] R. Schafranek, J. D. Baniecki, M. Ishii, Y. Kotaka, K. Yamanka, and K. Kurihara. Band offsets at the epitaxial $SrTiO_3/SrZrO_3$ (001) heterojunction. *Journal of Physics D: Applied Physics*, 45(5):055303, 2012.

[104] C. G. Van de Walle. Band lineups and deformation potentials in the model-solid theory. *Physical Review B*, 39(3):1871, 1989.

[105] P. G. Moses and C. G. Van de Walle. Band bowing and band alignment in InGaN alloys. *Applied Physics Letters*, 96(2):021908, 2010.

[106] J. Brous, I. Fankuchen, and E. Banks. Rare earth titanates with a perovskite structure. *Acta Crystallographica*, 6(1):67–70, 1953.

[107] R. H. Buttner and E. N. Maslen. Structural parameters and electron difference density in $BaTiO_3$. *Acta Crystallographica Section B: Structural Science*, 48(6):764–769, 1992.

[108] S. H. Wemple. Polarization Fluctuations and the Optical-Absorption Edge in $BaTiO_3$. *Physical Review B*, 2(7):2679, 1970.

[109] E. A. Zhurova, V. E. Zavodnik, S. A. Ivanov, P. P. Syrnikov, and V. G. Tsirelson. Electron density and anharmonicity of the thermal vibrations of the atoms in the perovskites $K_{1-x}Li_xTaO_3$. *Russian journal of inorganic chemistry*, 37(11):1240–1244, 1992.

[110] G. E. Jellison Jr, I. Paulauskas, L. A. Boatner, and D. J. Singh. Optical functions of $KTaO_3$ as determined by spectroscopic ellipsometry and comparison with band structure calculations. *Physical Review B*, 74(15):155130, 2006.

[111] A. Nakatsuka, O. Ohtaka, H. Arima, N. Nakayama, and T. Mizota. Cubic phase of single-crystal $LaAlO_3$ perovskite synthesized at 4.5 GPa and 1273 K. *Acta Crystallographica Section E: Structure Reports Online*, 61(8):148–150, 2005.

[112] H. Mizoguchi, P. M. Woodward, C.-H. Park, and D. A. Keszler. Strong near-infrared luminescence in $BaSnO_3$. *Journal of the American Chemical Society*, 126(31):9796–9800, 2004.

[113] S. Sasaki, C. T. Prewitt, J. D. Bass, and W. A. Schulze. Orthorhombic perovskite $CaTiO_3$ and $CdTiO_3$: structure and space group. *Acta Crystallographica Section C: Crystal Structure Communications*, 43(9):1668–1674, 1987.

[114] K. Ueda, H. Yanagi, R. Noshiro, H. Hosono, and H. Kawazoe. Vacuum ultraviolet reflectance and electron energy loss spectra of $CaTiO_3$. *Journal of Physics: Condensed Matter*, 10(16):3669, 1998.

[115] L. S. Cavalcante, A. Z. Simoes, J. C. Sczancoski, V. M. Longo, R. Erlo, M. T. Escote, E. Longo, and J. A. Varela. $SrZrO_3$ powders obtained by chemical method: synthesis, characterization and optical absorption behaviour. *Solid State Sciences*, 9(11):1020–1027, 2007.

[116] Y. S. Lee, J. S. Lee, T. W. Noh, D. Y. Byun, K. S. Yoo, K. Yamaura, and E. Takayama-Muromachi. Systematic trends in the electronic structure parameters of the 4*d* transition-metal oxides $SrMO_3$ (M= Zr, Mo, Ru, and Rh). *Physical Review B*, 67(11):113101, 2003.

[117] A. Vegas, M. Vallet-Regi, J. M. González-Calbet, and M. A. Alario-Franco. The $ASnO_3$ (A = Ca, Sr) perovskites. *Acta Crystallographica Section B: Structural Science*, 42(2):167–172, 1986.

[118] H. Mizoguchi and P. M. Woodward. Electronic structure studies of main group oxides possessing edge-sharing octahedra: implications for the design of transparent conducting oxides. *Chemistry of materials*, 16(25):5233–5248, 2004.

[119] P. S. Beurmann, V. Thangadurai, and W. Weppner. Phase transitions in the $SrSnO_3$–$SrFeO_3$ solid solutions: X-ray diffraction and Mössbauer studies. *Journal of Solid State Chemistry*, 174(2):392–402, 2003.

[120] B. Bellal, B. Hadjarab, A. Bouguelia, and M. Trari. Visible light photocatalytic reduction of water using $SrSnO_3$ sensitized by $CuFeO_2$. *Theoretical and Experimental Chemistry*, 45(3):172–179, 2009.

[121] D. A. MacLean, H.-N. Ng, and J. E. Greedan. Crystal structures and crystal chemistry of the $RETiO_3$ perovskites: RE= La, Nd, Sm, Gd, Y. *Journal of Solid State Chemistry*, 30(1):35–44, 1979.

[122] S. A. Chambers, M. H. Engelhard, V. Shutthanandan, Z. Zhu, T. C. Droubay, L. Qiao, P. V. Sushko, T. Feng, H. D. Lee, T. Gustafsson, et al. Instability, intermixing and electronic structure at the epitaxial heterojunction. *Surface Science Reports*, 65(10):317–352, 2010.

[123] L. Qiao, T. C. Droubay, T. C. Kaspar, P. V. Sushko, and S. A. Chambers. Cation mixing, band offsets and electric fields at $LaAlO_3/SrTiO_3$ (001) heterojunctions with variable La:Al atom ratio. *Surface Science*, 605(15):1381–1387, 2011.

[124] Y. Segal, J. H. Ngai, J. W. Reiner, F. J. Walker, and C. H. Ahn. X-ray photoemission studies of the metal-insulator transition in $LaAlO_3/SrTiO_3$ structures grown by molecular beam epitaxy. *Physical Review B*, 80(24):241107, 2009.

[125] G. Berner, A. Müller, F. Pfaff, J. Walde, C. Richter, J. Mannhart, S. Thiess, A. Gloskovskii, W. Drube, M. Sing, et al. Band alignment in $LaAlO_3/SrTiO_3$ oxide heterostructures inferred from hard x-ray photoelectron spectroscopy. *Physical Review B*, 88(11):115111, 2013.

[126] G. Conti, A. M. Kaiser, A. X. Gray, S. Nemšák, G. K. Pálsson, J. Son, P. Moetakef, A. Janotti, L. Bjaalie, C. S. Conlon, et al. Band offsets in complex-oxide thin films and heterostructures of $SrTiO_3/LaNiO_3$ and $SrTiO_3/GdTiO_3$ by soft and hard X-ray photoelectron spectroscopy. *Journal of Applied Physics*, 113(14):143704, 2013.

[127] H. J. Kim, U. Kim, H. M. Kim, T. H. Kim, H. S. Mun, B.-G. Jeon, K. T. Hong, W.-J. Lee, C. Ju, K. H. Kim, et al. High mobility in a stable transparent perovskite oxide. *Applied Physics Express*, 5(6):061102, 2012.

[128] D. G. Ouellette, P. Moetakef, T. A. Cain, J. Y. Zhang, S. Stemmer, D. Emin, and S. J. Allen. High-density two-dimensional small polaron gas in a delta-doped Mott insulator. *Scientific Reports*, 3, 2013.

[129] R. Chen, S. B. Lee, and L. Balents. Dimer Mott insulator in an oxide heterostructure. *Physical Review B*, 87(16):161119, 2013.

[130] C. W. Turner and J. E. Greedan. Ferrimagnetism in the rare earth titanium (III) oxides, $RTiO_3$; R= Gd, Tb, Dy, Ho, Er, Tm. *Journal of Solid State Chemistry*, 34(2):207–213, 1980.

[131] A. C. Komarek, H. Roth, M. Cwik, W.-D. Stein, J. Baier, M. Kriener, F. Bourée, T. Lorenz, and M. Braden. Magnetoelastic coupling in $RTiO_3$ (R= La, Nd, Sm, Gd, Y) investigated with diffraction techniques and thermal expansion measurements. *Physical Review B*, 75(22):224402, 2007.

[132] D. A. Crandles, T. Timusk, J. D. Garrett, and J. E. Greedan. The midinfrared absorption in $RTiO_3$ perovskites (R= La, Ce, Pr, Nd, Sm, Gd): The Hubbard gap? *Physica C: Superconductivity*, 201(3):407–412, 1992.

[133] M. N. Grisolia, F. Y. Bruno, D. Sando, H. J. Zhao, E. Jacquet, X. M. Chen, L. Bellaiche, A. Barthélémy, and M. Bibes. Structural, magnetic, and electronic properties of $GdTiO_3$ Mott insulator thin films grown by pulsed laser deposition. *Applied Physics Letters*, 105(17):172402, 2014.

[134] A. Baldereschi, S. Baroni, and R. Resta. Band offsets in lattice-matched heterojunctions: a model and first-principles calculations for GaAs/AlAs. *Physical Review Letters*, 61(6):734, 1988.

[135] S. Nemšák, G. Conti, A. X. Gray, G. K. Pálsson, C. Conlon, D. Eiteneer, A. Keqi, A. Rattanachata, A. Y. Saw, A. Bostwick, et al. Energetic, spatial and momentum character of a buried interface: the two-dimensional electron gas between two metal oxides. *arXiv preprint arXiv:1508.01832*, 2015.

[136] C. A. Jackson and S. Stemmer. Interface-induced magnetism in perovskite quantum wells. *Physical Review B*, 88(18):180403, 2013.

[137] D. Doennig and R. Pentcheva. Control of orbital reconstruction in $(LaAlO_3)_M/(SrTiO_3)_N$ (001) quantum wells by strain and confinement. *Scientific Reports*, 5, 2015.

[138] S. Ohta, T. Nomura, H. Ohta, M. Hirano, H. Hosono, and K. Koumoto. Large thermoelectric performance of heavily Nb-doped $SrTiO_3$ epitaxial film at high temperature. *Applied Physics Letters*, 87(9):092108, 2005.

[139] A. Janotti, B. Jalan, S. Stemmer, and C. G. Van de Walle. Effects of doping on the lattice parameter of $SrTiO_3$. *Applied Physics Letters*, 100(26):262104, 2012.

[140] L. Bjaalie, A. Janotti, B. Himmetoglu, and C. G. Van de Walle. Turning $SrTiO_3$ into a Mott insulator. *Physical Review B*, 90(19):195117, 2014.

[141] T. Katsufuji, Y. Taguchi, and Y. Tokura. Transport and magnetic properties of a Mott-Hubbard system whose bandwidth and band filling are both controllable: $R_{1-x}Ca_xTiO_{3+y/2}$. *Physical Review B*, 56(16):10145, 1997.

[142] L. Bjaalie, A. Verma, B. Himmetoglu, A. Janotti, S. Raghavan, V. Protasenko, E. H. Steenbergen, D. Jena, S. Stemmer, and C. G. Van de Walle. Determination of the Mott-Hubbard gap in $GdTiO_3$. *Physical Review B*, 92:085111, Aug 2015.

[143] P. Y. Yu and M. Cardona. Electronic band structures. *Fundamentals of Semiconductors*, pages 17–106, 2010.

[144] M. Cococcioni and S. De Gironcoli. Linear response approach to the calculation of the effective interaction parameters in the LDA + U method. *Physical Review B*, 71(3):035105, 2005.

[145] D. Vanderbilt. Soft self-consistent pseudopotentials in a generalized eigenvalue formalism. *Physical Review B*, 41(11):7892, 1990.

[146] P. Giannozzi, S. Baroni, N. Bonini, M. Calandra, R. Car, C. Cavazzoni, D. Ceresoli, G. L. Chiarotti, M. Cococcioni, I. Dabo, et al. QUANTUM ESPRESSO: a modular and open-source software project for quantum simulations of materials. *Journal of Physics: Condensed Matter*, 21(39):395502, 2009.

[147] E. Pavarini, A. Yamasaki, J. Nuss, and O. K. Andersen. How chemistry controls electron localization in $3d^1$ perovskites: a Wannier-function study. *New Journal of Physics*, 7(1):188, 2005.

[148] F. El-Mellouhi, E. N. Brothers, M. J. Lucero, I. W. Bulik, and G. E. Scuseria. Structural phase transitions of the metal oxide perovskites $SrTiO_3$, $LaAlO_3$, and $LaTiO_3$ studied with a screened hybrid functional. *Physical Review B*, 87(3):035107, 2013.

[149] L.-J. Yang, Y.-K. Weng, H.-M. Zhang, and S. Dong. Strain driven sequential magnetic transitions in strained $GdTiO_3$ on compressive substrates: a first-principles study. *Journal of Physics: Condensed Matter*, 26(47):476001, 2014.

[150] M. Gajdoš, K. Hummer, G. Kresse, J. Furthmüller, and F. Bechstedt. Linear optical properties in the projector-augmented wave methodology. *Physical Review B*, 73(4):045112, 2006.

[151] H. D. Zhou and J. B. Goodenough. Localized or itinerant TiO_3 electrons in $RTiO_3$ perovskites. *Journal of Physics: Condensed Matter*, 17(46):7395, 2005.

[152] Y. Tokura, Y. Taguchi, Y. Okada, Y. Fujishima, T. Arima, K. Kumagai, and Y. Iye. Filling dependence of electronic properties on the verge of metal–Mott-insulator transition in $Sr_{1-x}La_xTiO_3$. *Physical Review Letters*, 70(14):2126, 1993.

[153] M. Klinger. Quantum theory of non-steady-state conductivity in low mobility solids. *Physics Letters*, 7(2):102–104, 1963.

[154] H. G. Reik and D. Heese. Frequency dependence of the electrical conductivity of small polarons for high and low temperatures. *Journal of Physics and Chemistry of Solids*, 28(4):581–596, 1967.

[155] D. Emin. Optical properties of large and small polarons and bipolarons. *Physical Review B*, 48(18):13691, 1993.

[156] A. Janotti, C. Franchini, J. B. Varley, G. Kresse, and C. G. Van de Walle. Dual behavior of excess electrons in rutile TiO_2. *Physica Status Solidi (RRL)-Rapid Research Letters*, 7(3):199–203, 2013.

[157] L. Bjaalie, D. G. Ouellette, P. Moetakef, T. A. Cain, A. Janotti, B. Himmetoglu, S. J. Allen, S. Stemmer, and C. G. Van de Walle. Small hole polarons in rare-earth titanates. *Applied Physics Letters*, 106(23):232103, 2015.

[158] T. Holstein. Studies of polaron motion: Part II. The small polaron. *Annals of Physics*, 281(1):725–773, 2000.

[159] D. Emin. Phonon-assisted transition rates I. Optical-phonon-assisted hopping in solids. *Advances in Physics*, 24(3):305–348, 1975.

[160] A. S. Alexandrov and J. T. Devreese. *Advances in polaron physics*. Springer, 2010.

[161] D. A. Crandles, T. Timusk, J. D. Garrett, and J. E. Greedan. Infrared-active phonons in $RTiO_3$ perovskites (R= La, Ce, Pr, Nd, Sm, Gd). *Physical Review B*, 49(6):4299, 1994.

[162] K. Huang and A. Rhys. Theory of light absorption and non-radiative transitions in f-centres. In *Proceedings of the Royal Society of London A: Mathematical, Physical and Engineering Sciences*, volume 204, pages 406–423. The Royal Society, 1950.

[163] A. Alkauskas, Q. Yan, and C. G. Van de Walle. First-principles theory of nonradiative carrier capture via multiphonon emission. *Physical Review B*, 90(7):075202, 2014.

[164] A. Alkauskas, P. Broqvist, and A. Pasquarello. Defect levels through hybrid density functionals: Insights and applications. *Physica Status Solidi (b)*, 248(4):775–789, 2011.

[165] F. Oba, A. Togo, I. Tanaka, J. Paier, and G. Kresse. Defect energetics in ZnO: A hybrid Hartree-Fock density functional study. *Physical Review B*, 77(24):245202, 2008.

[166] P. Deák, B. Aradi, T. Frauenheim, E. Janzén, and A. Gali. Accurate defect levels obtained from the HSE06 range-separated hybrid functional. *Physical Review B*, 81(15):153203, 2010.

[167] J. L. Lyons, A. Janotti, and C. G. Van de Walle. Shallow versus deep nature of Mg acceptors in nitride semiconductors. *Physical Review Letters*, 108(15):156403, 2012.

[168] A. Alkauskas, J. L. Lyons, D. Steiauf, and C. G. Van de Walle. First-principles calculations of luminescence spectrum line shapes for defects in semiconductors: the example of GaN and ZnO. *Physical Review Letters*, 109(26):267401, 2012.

[169] C. Freysoldt, J. Neugebauer, and C. G. Van de Walle. Fully *abinitio* finite-size corrections for charged-defect supercell calculations. *Physical Review Letters*, 102(1):016402, 2009.

[170] C. Freysoldt, J. Neugebauer, and C. G. Van de Walle. Electrostatic interactions between charged defects in supercells. *Physica Status Solidi (b)*, 248(5):1067–1076, 2011.

[171] M. Chase. NIST-JANAF thermochemical tables. 1998.

[172] D. R. Lide. *CRC handbook of chemistry and physics*. CRC press, 2004.

[173] K. B. Helean, S. V. Ushakov, C. E. Brown, A. Navrotsky, J. Lian, R. C. Ewing, J. M. Farmer, and L. A. Boatner. Formation enthalpies of rare earth titanate pyrochlores. *Journal of Solid State Chemistry*, 177(6):1858–1866, 2004.

[174] K. T. Jacob and G. Rajitha. Thermodynamic properties of strontium titanates: Sr_2TiO_4, $Sr_3Ti_2O_7$, $Sr_4Ti_3O_{10}$, and $SrTiO_3$. *The Journal of Chemical Thermodynamics*, 43(1):51–57, 2011.

[175] A. Janotti, J. B. Varley, M. Choi, and C. G. Van de Walle. Vacancies and small polarons in $SrTiO_3$. *Physical Review B*, 90(8):085202, 2014.

[176] L. Weston, A. Janotti, X. Y. Cui, C. Stampfl, and C. G. Van de Walle. Hybrid functional calculations of point defects and hydrogen in $SrZrO_3$. *Physical Review B*, 89(18):184109, 2014.

[177] M. Choi, A. Janotti, and C. G. Van de Walle. Native point defects in $LaAlO_3$: A hybrid functional study. *Physical Review B*, 88(21):214117, 2013.

[178] T. A. Cain, P. Moetakef, C. A. Jackson, and S. Stemmer. Modulation doping to control the high-density electron gas at a polar/non-polar oxide interface. *Applied Physics Letters*, 101(11):111604, 2012.

[179] P. Moetakef and T. A. Cain. Metal–insulator transitions in epitaxial $Gd_{1-x}Sr_xTiO_3$ thin films grown using hybrid molecular beam epitaxy. *Thin Solid Films*, 583:129–134, 2015.

[180] A. Alkauskas, Q. Yan, and C. G. Van de Walle. First-principles theory of nonradiative carrier capture via multiphonon emission. *Physical Review B*, 90(7):075202, 2014.

[181] M. Boucherit, O. Shoron, C. A. Jackson, T. A. Cain, M. L. C. Buffon, C. Polchinski, S. Stemmer, and S. Rajan. Modulation of over 10^{14} cm^{-2} electrons in $SrTiO_3/GdTiO_3$ heterostructures. *Applied Physics Letters*, 104(18):182904, 2014.

[182] S. Raghavan, S. J. Allen, and S. Stemmer. Subband structure of two-dimensional electron gases in $SrTiO_3$. *Applied Physics Letters*, 103(21):212103, 2013.

[183] W. B. Fowler, J. K. Rudra, M. E. Zvanut, and F. J. Feigl. Hysteresis and Franck-Condon relaxation in insulator-semiconductor tunneling. *Physical Review B*, 41(12):8313, 1990.

[184] P. E. Blöchl and J. H. Stathis. Hydrogen electrochemistry and stress-induced leakage current in silica. *Physical Review Letters*, 83(2):372, 1999.

[185] K. Krishnaswamy, L. Bjaalie, B. Himmetoglu, A. Janotti, L. Gordon, and Van de Walle C. G. $BaSnO_3$ as a channel material in perovskite oxide heterostructures. *Applied Physics Letters*, 108(083501):083501, 2016.

[186] I. Loa, X. Wang, K. Syassen, H. Roth, T. Lorenz, M. Hanfland, and Y.-L. Mathis. Crystal structure and the Mott-Hubbard gap in $YTiO_3$ at high pressure. *Journal of Physics: Condensed Matter*, 19(40):406223, 2007.